NTNU – Trondheim
Norwegian University of
Science and Technology

Analysis of Drifting for a Remotely Controlled Car

Stian Ellefsen

Master of Science in Engineering Cybernetics
Submission date: June 2012
Supervisor: Thor Inge Fossen, ITK

Norwegian University of Science and Technology
Department of Engineering Cybernetics

Analysis of Drifting for a Remotely Controlled Car

Norwegian University of Science and Technology, NTNU
Department of Engineering Cybernetics

Ellefsen, Stian
June 1, 2012

Abstract

By restricting a vehicle to the linear region of operation, with a small sideslip angle, a vehicle cannot achieve its full potential. By entering the nonlinear region of operation tighter corners can be achieved and some accidents could be prevented. Research is currently being conducted to introduce drifting into vehicle safety systems, which currently restrict the vehicle to the linear region of operation. Vehicle drifting has been shown to have unstable equilibria, while still maintaining controllability.

In this thesis, equilibria with sideslip angles ranging from -30 degrees to 30 are found for a nonlinear two-track model simulator. Analysis showed that simple mappings could be made between the states and the inputs, and between the states themselves. All the linearised systems in these equilibria were found to be unstable, which coincides with current research.

In addition, this thesis presents an adaptive backstepping controller, which is used for converge to an arbitrary sideslip angle, and when the drift is being initialised the controller mimics the behaviour of Power Over drifting technique. The adaptive part of the backstepping controller is used as integral action that, by the use of adaptation, finds the stationary deviation between the yaw rate and the desired yaw rate, which is added to the control law. A mapping between the desired sideslip angle and the desired yaw rate is used in a feed forward term such that the desired sideslip angle is achieved when the yaw rate converges. The controller has been tested with a modified Line Of Sight guidance system which provided the controller with a desired sideslip angle. Robust response with respect to changes in vehicle mass and inertia was observed.

Sammendrag

Ved å begrense et kjøretøy til det lineære operasjonsområdet, med en liten sideslippvinkel, kan ikke et kjøretøy oppnå sitt fulle potensiale. Ved å entre det ulineære oprasjonsområdet kan skarpere svinger tas og noen ulykker kunne vært unngått. Idag forskes det på å introdusere drifting i bilsikkerhetssystemer, som idag begrenser bilen til det lineære oprasjonsområdet. Drifting av bil har blitt vist å ha ustabile likevektspunter, samtidig som styrbarheten bevares.

I denne avhandlingene ble likevektspunkter med sideslippvinkler mellom -30 grader og 30 funnet for en simulator av en ulineær to-sporsmodell. Analysen viste at det fantes enkle funksjoner som beskrev forholdet mellom tilstander og innganger, og mellom tilstandene selv. Alle de lineæriserte systemene i disse likevektspunktene var ustabile, noe som samsvarer med aktuell forskning.

I tillegg presenterer denne oppgaven en adaptiv backsteppingkontroller, som brukes til å konvergere til en vilkårlig sideslippvinkel, og når drifting blir initialisert så etterligner kontrolleren oppførselen til driftingteknikken Power Over. Den adaptive delen av backsteppingkontrolleren blir brukt som integralvirkning som, ved å bruke adapsjon, finner stasjonær- avviket mellom giringsraten og den ønskede giringsrate, som blir lagt til i kontrolloven. En funksjon som beskriver forholdet mellom den ønskede sideslippvinkelen og den ønskede giringsraten blir brukt i en foroverkobling slik at den ønskede sideslippvinkelen blir oppnådd når giringsraten konvergerer. Kontrolleren var robust mot endringer i bilens masse og treghet. Kontrolleren ble testet sammen med en modifisert Line Of Sight baneplanlegger som forsynte kontrolleren med sideslippvinkelreferanse. Robust respons med hensyns på endringer i bilens masse og treghet ble observert.

Preface

This master's thesis is the finishing touches on my 5 years of higher education at Norwegian University of Science and Technology. Hopefully, this will only be a stepping stone to my Ph.D. The world of cybernetics has been great fun these past five years, and I am looking forward to delving deeper.

I had several supervisors during this thesis, however, they have all helped me when I was in need. Therefore, I would like to thank Professor Thor Inge Fossen and Professor Jan Tommy Gravdahl from the Department of Engineering Cybnertics for steering me in the right direction and digging me out of the holes I dug for myself. From Kongsberg Defence Systems I would like to thank Jon Bernhard Høstmark and Åge Skullestad for insightful tips and keeping up my motivation when progress was slow.

Finally, I would like to thank my family for always supporting me.

Table of Contents

List of Figures

List of Tables

1 Abbreviations and Nomenclature

1.1 Abbreviations

AWD	All wheel driven
DOF	Degree of freedom
fw	From wheels
FL	Front left wheel
FR	Front right wheel
FWD	Rear wheel driven
IMU	Inertial measurement unit
LFC	Lyapunov function candidate
LOS	Line of sight
PID	Proportional-integral-derivative
RL	Rear left wheel
RR	Rear right wheel
RWD	Rear wheel driven
UGAS	Uniform global asymptotic stability
ULES	Uniform local exponential stability

1.2 Nomenclature

$\mathbf{A}$	State matrix
b	Distance between two wheels on the same axle
$\mathbf{B}$	Input matrix
C_D	Drag coefficient
$\mathbf{C}$	Output matrix
$\mathbf{C}_{RB}$	Rigid body Coriolis matrix
D	Drag
g	Acceleration due to gravity
h_{CG}	Distance between ground and vehicle center of gravity
I_{xx}	Moment of inertia in roll
I_{xy}	Product of inertia about x^b and y^b axes
I_{xz}	Product of inertia about x^b and z^b axes
I_{yy}	Moment of inertia in pitch
I_{yz}	Product of inertia about y^b and z^b axes
I_{zz}	Moment of inertia in yaw
$\mathbf{I}$	Identity matrix
$\mathbf{I_{CG}}$	Inertia matrix about center of gravity
$\mathbf{K}$	Force coefficient matrix, Feedback gain matrix
l_f	Distance from vehicle center of gravity to front axle

l_r	Distance from vehicle center of gravity to rear axle
L	Rolling moment
m	Vehicle mass
$\mathbf{M}_{RB}$	Rigid body inertia matrix
p	Roll rate
q	Pitch rate
r	Yaw rate
$\mathbf{R}$	Rotation matrix
$\mathbf{S}$	Skew-symmetric matrix
t	Time
T	Time step
$\mathbf{T}$	Thrust and steering configuration matrix
$\mathbf{u}$	Input vector
u	Total axial velocity
u_0	Axial component of steady equilibrium velocity
v	Total lateral velocity
v_0	Lateral component of steady equilibrium velocity
V_T	Total speed
V_{T0}	Total steady equilibrium speed
w	Total normal velocity
x	Longitudinal coordinate in axis system
$\mathbf{x}$	State vector
X	Axial force component
y	Lateral coordinate in axis system
$\mathbf{y}$	Output vector
Y	Lateral force component
z	Normal coordinate in axis system
Z	Normal force component

Greek letter

α	Wheel slip angle
β	Sideslip angle
δ	Wheel turn angle
ϵ	Perturbation
$\boldsymbol{\eta}$	Position and attitude vector
θ	Euler pitch angle
$\boldsymbol{\Theta}$	Vector of euler angles
ϑ	Angle between vehicle center of gravity and wheel center point
$\boldsymbol{\nu}$	Vector of speeds and rates
ρ	Density
$\boldsymbol{\tau}$	Vector of forces and moments
$\boldsymbol{\tau}_{RB}$	Vector of rigid body forces and moments
ϕ	Euler roll angle
ψ	Euler yaw angle

ω	Wheel angular velocity, Rotational velocity of the motor shaft

Subscripts

0	Equilibrium value
3×3	Matrix dimension
b	BODY axis
$brake$	Braking
c	Control
CG	Center of gravity
d	Desired
d, ff	Desired feed forward
$drag$	Drag
$drive$	Driving
D	Drag
e	Error
eff	Effective arm
f	Front
$fric$	Friction
fw	From wheels
FL	Front left wheel
FR	Front right wheel
g	Gravitational
nb	Between BODY and NWU
$prev$	Previous sample
r	Rolling
R, FL	Rotational equivalent velocity for front left wheel
R, FR	Rotational equivalent velocity for front right wheel
R, RL	Rotational equivalent velocity for rear left wheel
R, RR	Rotational equivalent velocity for rear right wheel
RB	Rigid body
RL	Rear left wheel
RR	Rear right wheel
s	Side
T	Thrust
x	Axial
y	Lateral
w	Wheels
w, FL	Wheel axis for front left wheel
w, FR	Wheel axis for front right wheel
w, RL	Wheel axis for rear left wheel
w, RR	Wheel axis for rear right wheel
W, FL	Wheel ground contact point velocity for front left wheel
W, FR	Wheel ground contact point velocity for front right wheel
W, RL	Wheel ground contact point velocity for rear left wheel

W, RR	Wheel ground contact point velocity for rear right wheel

Superscripts

b	Expressed in BODY reference frame
FL	Expressed in front left wheel reference frame
FR	Expressed in front right wheel reference frame
lat	Lateral in wheel velocity frame
$long$	Longitudinal in wheel velocity frame
n	Expressed in NWU reference frame
RL	Expressed in rear left wheel reference frame
RR	Expressed in rear right wheel reference frame
T	Transpose

2 Introduction

Skilled drivers can manoeuvre through the most narrow and curvy roads, however they cannot do so if they only use the throttle for speed control and the steering angle as the only means for turning. By using the throttle in conjunction with the steering can cause the back wheels to lose traction while navigating a turn. This results in the rear part of the vehicle moving out of the turn, forcing the vehicle to rotate while the direction of the speed is unchanged. This phenomena is called oversteering, and is the first step toward drifting. Drifting is achieved when the throttle and steering causes the vehicle to stop rotating relative to the vehicle speed. The angle between the front of the vehicle and the direction of the speed is called the sideslip angle. A mathematical definition for the sideslip angle is the arctanget of the lateral velocity v divided by the the axial velocity u of the vehicle

$$\beta = \arctan\left(\frac{v}{u}\right) \tag{2.1}$$

The sideslip angle β and the velocities together with the speed can be seen in figure 2.1. The speed is defined as

$$V_T = \sqrt{u^2 + v^2 + w^2} \tag{2.2}$$

where w is the normal velocity. According to [1], when drifting is not being performed, the sideslip angle is normally between ±2 deg.

To be able to experience the full potential of a vehicle, certain limits need to be crossed, which are not crossed during normal conditions. A vehicle driving close to the limit of what it is capable of, can do sharper turns and achieve faster lap times with the use of drifting techniques [2]. Drifting is often performed in rally driving, when the roads are narrow and curvy with changing road conditions.

2.1 Motivation

In recent years, research has been conducted on utilizing drifting techniques from race car driving in accident avoidance. The automotive systems used today, forces the vehicle to operate within the linear region [3]. With this restriction, the driver vehicle system is stable and the average driver can predict how the vehicle will react to steering, throttle and breaking input. According to [4], the vehicle system becomes unstable when the nonlinear region with large sideslip angles is entered, while controllability is retained.

Under normal circumstances, there are only two vehicle states the driver wants to control, and that is the yaw rate and the speed. However, in the nonlinear region the sideslip angle

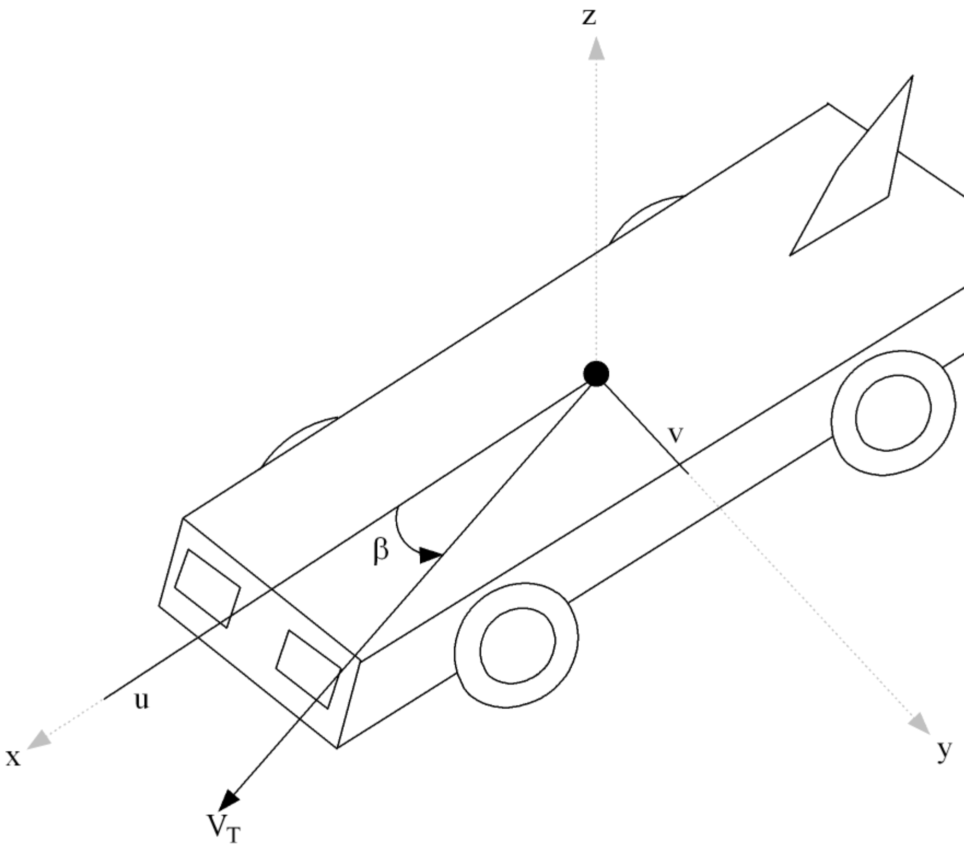

Figure 2.1: The sideslip angle, velocities and speed.

also is in need of control. Which entails that the system wants to control three states with only two control inputs. Here a choice must be made, to cope for this lack of actuation. In this thesis, based on a simulator made in [5], a controller will be made to converge to arbitrary sideslip angles, and tested for sideslip angles within the range ±30 deg. The sideslip angle was chosen for control to show the clear connection between the yaw rate and the sideslip angle. By converging to a sideslip angle, the vehicle will gain a yaw rate and a turn is established.

Because the vehicle has constraints in throttle setting and steering angle, not all combinations of speed and sideslip angle can be achieved. A drifting equilibrium analysis is needed to find the feasible drifting equilibria. In addition, to achieve maximum cornering efficiency, the sideslip angles corresponding to the largest yaw rate needed to be found before control is performed.

Rear wheel drive with locked differential will be used in this thesis. The road surface is assumed flat, which gives no pitch and rolling motion of the vehicle. This flat surface assumption leads to uniform surface friction in the testing environment, which entails friction differences between the left and right track is assumed negligible.

This thesis is part of the LocalHawk project, which will be described in the following section.

2.2 LocalHawk

The LocalHawk project is a collaboration between many engineering disciplines to create an Autonomous Unmanned Aerial Vehicle from scratch. The starting point was a master's thesis written by Jon Bernhard Høstmark at Norwegian University of Science and Technology in 2007. Kongsberg Defence Systems supplies the funding for this project and students contribute papers, master's theses and some are invited to do summer internships at Kongsberg. Project challenges include instrumentation and electronics, control system design, waypoint navigation, in-flight communication with ground station and object recognition by means of camera technology.

A new testing platform was needed, because the LocalHawk hardware and software became more complex and travelling to an airfield to do simple tests was too time consuming. In addition, badly written and untested code could cause the LocalHawk to fall from the sky, which could damage equipment.

2.3 The LocalBug

The need for a new test platform resulted in the LocalBug, which is a remotely controlled car. It can be loaded with the same payload as the LocalHawk and ground testing reduces the risk of damaging the hardware.

The LocalBug has a hardware platform called Phoenix II which interfaces all the devices connected to the LocalBug. The sensor package consists of an Inertial measurement unit(IMU), with three-axis accelerometer and gyroscope. In addition, the IMU has an integrated GPS receiver, magnetometer, barometer and a Kalman filter. Phoenix II also receives signals from a radio controller used for manual control of the vehicle. A 3G link is used to send and receive data from the ground station. If needed, a camera can also be connected for use in object recognition.

2.4 Previous Work

In the last few years vehicle behaviour during large sideslips, or drifting has been studied by many. The first use of this technique was within the race car society which found that corners could be taken faster by drifting. Now the behaviour is studied to better understand the limitations of vehicle performance which can contribute to new safety system features for vehicles [6].

The steady state condition of drifting has been investigated by many [6], [7], [8], [9], [10], [3], [11] and many more. A two-wheel model called a bicycle model was used in [3] and [9] for linearisation and control with a sliding mode controller. It was shown that the sliding mode controller in [3] and [9] converged to a steady state drifting condition, which was to be expected since the system was linearised.

In [8], an analysis of pole movements of a linearised vehicle model with four wheels was performed, about a steady state drifting condition. It was observed that the steady state drifting condition is unstable and thus in need of stabilization by a controller or a experienced driver. In [7], a two-wheel model was linearised, similar to the model in [9]. The model was controlled and used for analysis of steady state behaviour by means of phase diagrams.

Data from a rally car were used to understand the steady state drifting condition and a more complex four wheel model which included suspension dynamics was used in [10]. The model in [10] was linearised and controlled by means of sliding mode controller. Simulation supported the findings in [8], that the vehicle needed steering and throttle control to obtain steady state drifting. A linear controller for steering was made for a rear wheel driven(RWD) vehicle for a steady state drifting in [11]. The steering controller was applied to a bicycle model, and a separate speed controller was also implemented for control to steady state drifting in [11].

The bicycle model was used in [6], however, contrary to the other papers stated above, the control was performed on a front wheel driven(FWD) vehicle. To drift with a FWD vehicle, the handbrake was used. A Linear-quadratic regulator provided convergence to steady state drifting.

The difference between minimum cornering time and maximum exit velocity was observed in [12]. It was shown that with a slower cornering time, the maximum exit velocity could be larger, while both used drifting techniques.

An empirical description of two drifting techniques called Trail-braking and Pendulum-turn is found in [2]. Trail-braking is essentially breaking during the cornering to cause the drift, and Pendulum-turn is done by steering in the opposite direction of the turn and counter steering to cause a drift. Different optimization methods were used on a bicycle model to perform the drifting manoeuvres.

In [13], by optimization it is shown that Trail-braking corresponds to the minimum-time cornering solution when a vehicle needs to return to a straight line right after the corner.

Feedback linearisation of a four wheel model was used for trajectory tracking in [5]. Here the sideslip angle was controlled to achieve desired yaw rate when cornering.

Based on known steady state drifting conditions, a controller using elements of feedback linearisation and saturation avoidance was tested in practice in [4]. Even though the controller was derived using a bicycle model, the controller converged to the desired drifting condition.

Open loop commands was tested on a remotely controlled car in [24]. Where a model of the drift is run in parallel with a physical experiment with a remotely controlled car. The model estimated inputs that were used for the vehicle.

2.5 Contribution of Thesis

This thesis inspects the drifting equilibrium points of the LocalBug simulator from [5]. Because of input constraints, not all equilibrium points are feasible, and the infeasible equilibrium points are excluded from the analysis. The simulator is linearised and the pole movements of the equilibrium points are analysed. Equilibrium points with the fastest yaw rate are extracted, and used for control.

An adaptive backstepping controller for the wheel turning angle, that converges to any of the equilibrium points found for the LocalBug simulator was developed. To cope with the underactuation of the vehicle, the adaptive backstepping controller for the sideslip angle controls both the sideslip angle and the yaw rate in cascade. For speed control, a simple Proportional-Integral-Derivative(PID) controller was used. The adaptive backstepping controller was tested successfully on the LocalBug simulator, with faster lap times than conventional steering.

In parallel with this thesis, guidance has been provided to a group of students in the subject $Eksperter\ i\ Team$. The group did an analysis of different sideslip angle sensors and interfaced the IMU in the LocalBug with Explicit Target.

2.6 Thesis Outline

Chapter 3 contains some mathematical tools used in this thesis. In chapter 4, the kinematics of the vehicle is derived, which includes the coordinate systems and rotations between the coordinate system. In addition, the rigid body kinetics are described in this chapter. The nonlinear two-track model developed in [5], will be described in detail in chapter 5. Linearisation of the model described in chapter 5 is performed in chapter 6, which includes finding the linearisation points, also called the drifting equilibria. Inspection of the drifting equilibria is performed in chapter 7. Derivation and stability analysis of the adaptive backstepping controller and the guidance system can be found in chapter 8. The simulation results and discussion of these are done in chapter 9. In chapter 10, the report conclusion and proposals of further work are presented.

3 Mathematical Preliminaries

Rotation Matrices

According to [14], a rotation between two frames a and b can be expressed as a rotation matrix $\mathbf{R}_b^a$ which is an element in the special orthogonal group of order 3($SO(3)$). The $SO(3)$ can be expressed as

$$SO(3) = \{\ \mathbf{R}|\mathbf{R} \in \mathbb{R}^{3\times 3},\ \mathbf{R} \text{ is orthogonal and } \det \mathbf{R} = 1\ \} \tag{3.1}$$

The group $SO(3)$ is a subset of all orthogonal matrices of order 3($O(3)$), where $O(3)$ is defined as

$$O(3) = \{\ \mathbf{R}|\mathbf{R} \in \mathbb{R}^{3\times 3},\ \mathbf{R}\mathbf{R}^T = \mathbf{R}^T\mathbf{R} = \mathbf{I}\ \} \tag{3.2}$$

The properties of $O(3)$ imply

$$\mathbf{R}^{-1} = \mathbf{R}^T \tag{3.3}$$

A rotation from frame b to frame a will be written as the rotation matrix $\mathbf{R}_b^a$.

When transforming a vector from one coordinate frame to another, the notation is as follows

$$\mathbf{v}^a = \mathbf{R}_b^a \mathbf{v}^b \tag{3.4}$$

Trigonometric Properties

From [15], cosine to the sum of two angles can be expressed as

$$\cos(A \pm B) = \cos(A)\cos(B) \mp \sin(A)\sin(B) \tag{3.5}$$

According to [15], the cosine and sine can be expressed as functions of the tangent

$$\cos(A) = \frac{1}{\sqrt{1 + (\tan(A))^2}}\,, \qquad \sin(A) = \frac{\tan(A)}{\sqrt{1 + (\tan(A))^2}} \tag{3.6}$$

Using equation 3.6, the cosine and sine of the inverse tangent can be found

$$\cos(\arctan(B)) = \frac{1}{\sqrt{1 + (\tan(\arctan(B)))^2}} = \frac{1}{\sqrt{1 + B^2}} \tag{3.7}$$

$$\sin(\arctan(B)) = \frac{\tan(\arctan(B))}{\sqrt{1 + (\tan(\arctan(B)))^2}} = \frac{B}{\sqrt{1 + B^2}} \tag{3.8}$$

4 Kinematics and Kinetics

According to [14], dynamics consists of two parts: the kinematics which only treats the geometrical motion, and the kinetics, which is the forces and moments creating the motion. Coordinate systems need to be defined to be able to describe the kinematic of the system. Rotations between the different coordinate systems and movement of the coordinate systems are used for attitude and position calculations respectively. Newtons laws in a rotating coordinate frame can be used to describe the kinetics.

In this chapter, the coordinate systems are defined in section 4.1. Section 4.2 explains the state vectors used in this thesis. The transformations between the different frames are described in section 4.3. Lastly, the rigid body kinetics are developed in section 4.4.

4.1 Reference Systems

When deriving the equations of motion of the vehicle, well defined reference systems are required. This section explains the different reference systems used in the remainder of the thesis.

4.1.1 NWU

The North-West-Up (NWU) reference system is located at the surface of the earth. Where the NWU x-axis points toward the north pole, the z-axis points upward and y-axis points westward. The vehicle considered in this thesis only travels within a radius of a couple of hundred meters. Thus the surface of the earth can be assumed flat, and therefore the NWU reference frame is assumed inertial such that Newton's laws apply.

4.1.2 BODY

The BODY reference system is fixed to the vehicle. Vehicle position is expressed relative to the NWU frame, while the attitude of the vehicle is expressed as the orientation of the vehicle BODY axis system relative to the NWU frame.

For the BODY coordinate system, vehicle center of gravity and coordinate origin coincide. The BODY x-axis is pointing forward in the vehicle, z-axis is pointing upward and the y-axis completes the right hand coordinate system by pointing out of the left side of the vehicle, orthogonal to the BODY x- and z-axis. See figure 4.1 for a graphical representation of the BODY axes.

4.1.3 WHEEL

It is useful to include the WHEEL coordinate system for easy transformation of forces acting on the wheels to the BODY axis. Origin of the WHEEL coordinate system is the center of the wheel. The WHEEL x-axis is pointing out the front of the wheel, the z- and y-axis uses the same convention as the BODY axes.

There is a WHEEL axes system in each wheel. Vectors expressed in WHEEL for the front right wheel has superscript FR, and thus for the front left, rear right and rear left superscripts are FL, RR and RL respectively.

The rear WHEEL axes have the same orientation as the BODY axes since the vehicle only turns the front wheels. The WHEEL axes are shown in figure 4.1.

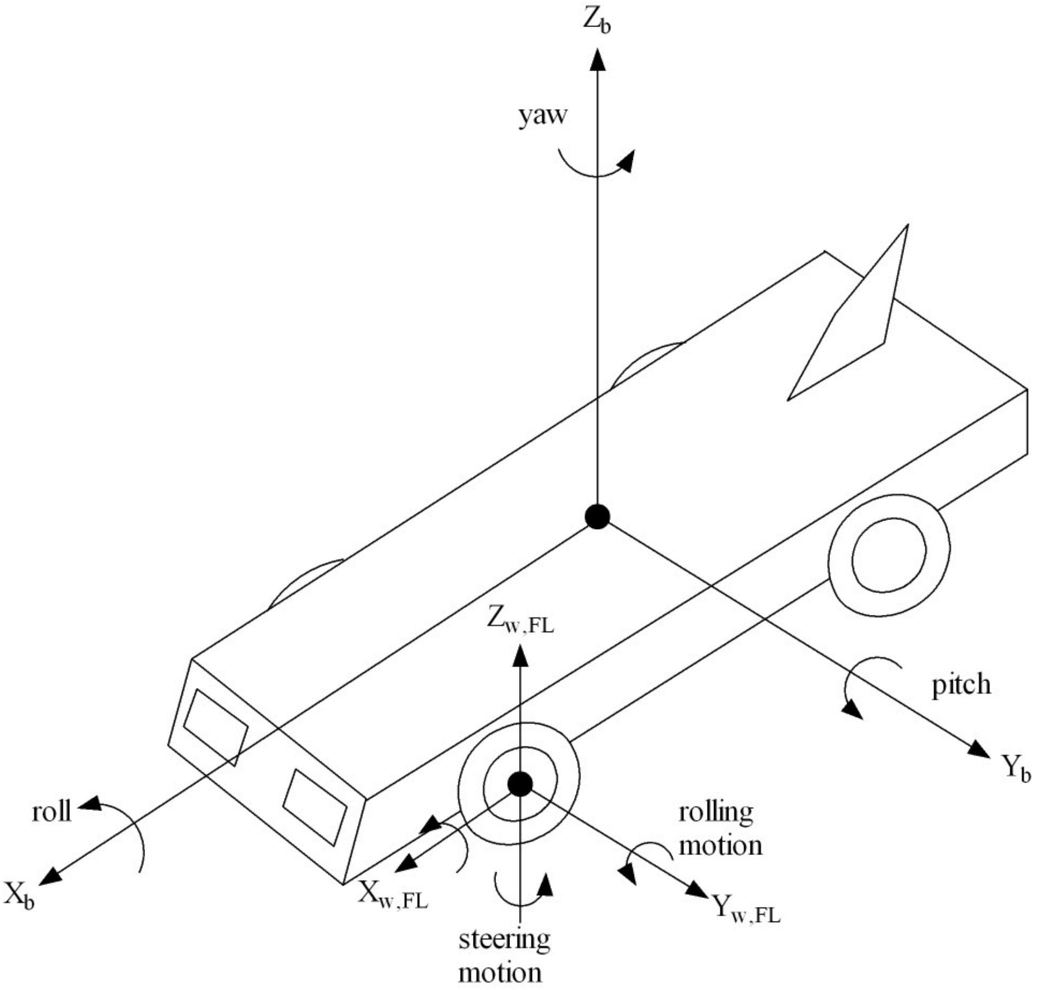

Figure 4.1: The BODY and WHEEL axes systems.

4.2 State Vector

Before stating the equations of motions it is useful to define the state vectors.

The position and orientation vector $\boldsymbol{\eta}$ for a body {b} relative to the NWU frame is defined as

$$\boldsymbol{\eta} := \begin{bmatrix} x^n \\ y^n \\ z^n \\ \phi_{nb} \\ \theta_{nb} \\ \psi_{nb} \end{bmatrix} = \begin{bmatrix} \text{north} \\ \text{west} \\ \text{up} \\ \text{roll angle} \\ \text{pitch angle} \\ \text{yaw angle} \end{bmatrix} \tag{4.1}$$

The velocity vector $\boldsymbol{\nu}$ in a general body reference frame is defined as

$$\boldsymbol{\nu} := \begin{bmatrix} u \\ v \\ w \\ p \\ q \\ r \end{bmatrix} = \begin{bmatrix} \text{axial velocity} \\ \text{lateral velocity} \\ \text{normal velocity} \\ \text{roll rate} \\ \text{pitch rate} \\ \text{yaw rate} \end{bmatrix} \tag{4.2}$$

The components of the velocity vector are shown in figure 4.2.

The force and moment vector $\boldsymbol{\tau}$ in a general body reference frame is defined as

$$\boldsymbol{\tau} := \begin{bmatrix} X \\ Y \\ Z \\ L \\ M \\ N \end{bmatrix} = \begin{bmatrix} \text{axial force} \\ \text{lateral force} \\ \text{normal force} \\ \text{rolling moment} \\ \text{pitching moment} \\ \text{yawing moment} \end{bmatrix} \tag{4.3}$$

The forces and moments can be seen in figure 4.2.

4.3 Transformations

Now the different reference frames can be related to each other, which are used for calculating attitude.

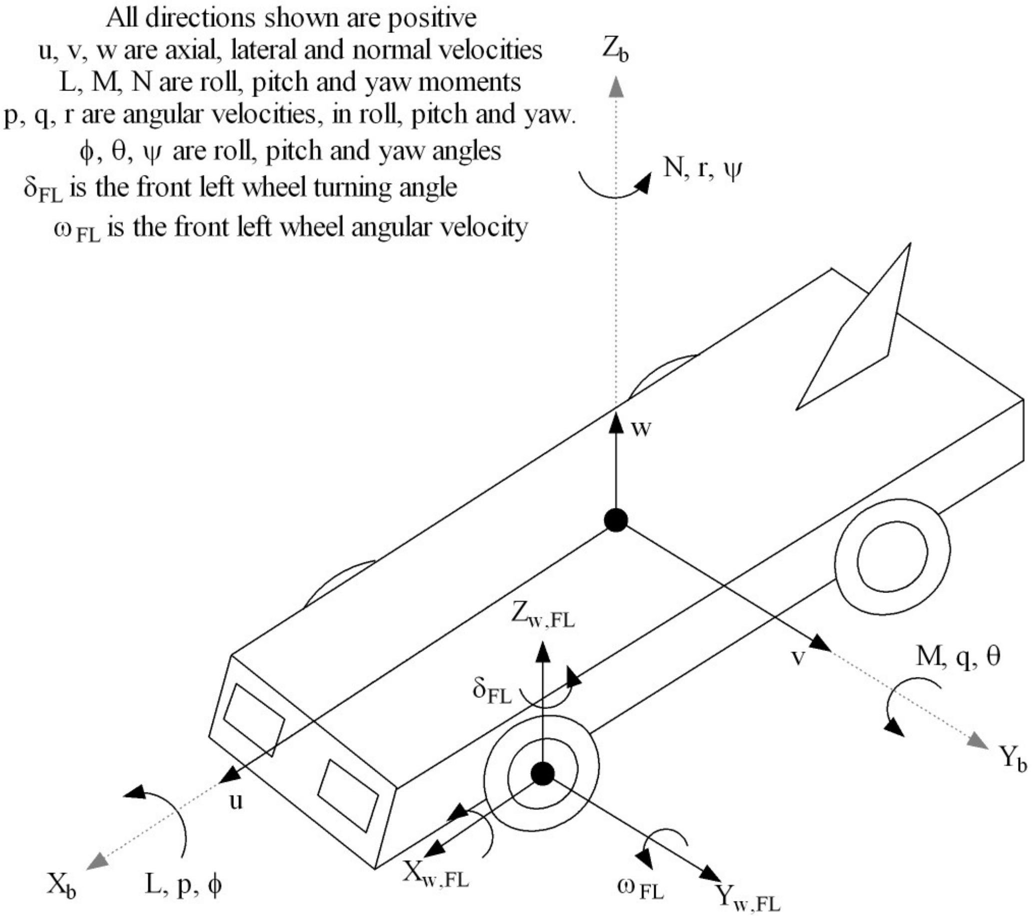

Figure 4.2: The BODY and WHEEL axes with associated variables.

4.3.1 Transformation between BODY and NWU

The rotation matrix is described in chapter 3. Relating a vector $\mathbf{p}^n$ in NWU and a vector $\mathbf{p}^b$ in BODY

$$\mathbf{p}^n = \mathbf{R}_b^n \mathbf{p}^b$$

where $\mathbf{R}_b^n$ is the Euler angle rotation matrix from BODY to NWU, and given by

$$\mathbf{R}_b^n = \begin{bmatrix} \mathrm{c}\psi_{nb}\mathrm{c}\theta_{nb} & -\mathrm{s}\psi_{nb}\mathrm{c}\phi_{nb} - \mathrm{c}\psi_{nb}\mathrm{s}\theta_{nb}\mathrm{s}\phi_{nb} & \mathrm{s}\psi_{nb}\mathrm{s}\phi_{nb} + \mathrm{c}\psi_{nb}\mathrm{c}\phi_{nb}\mathrm{s}\theta_{nb} \\ \mathrm{s}\psi_{nb}\mathrm{c}\theta_{nb} & \mathrm{c}\psi_{nb}\mathrm{c}\phi_{nb} + \mathrm{s}\psi_{nb}\mathrm{s}\theta_{nb}\mathrm{s}\phi_{nb} & -\mathrm{c}\psi_{nb}\mathrm{s}\phi_{nb} - \mathrm{s}\psi_{nb}\mathrm{c}\phi_{nb}\mathrm{s}\theta_{nb} \\ -\mathrm{s}\theta_{nb} & \mathrm{c}\theta_{nb}\mathrm{s}\phi_{nb} & \mathrm{c}\theta_{nb}\mathrm{c}\phi_{nb} \end{bmatrix}$$

where $\mathrm{s}\cdot = \sin(\cdot)$ and $\mathrm{c}\cdot = \cos(\cdot)$.

This gives the relationship between the translation motion in BODY and NWU

$$\begin{bmatrix}\dot{x}^n\\ \dot{y}^n\\ \dot{z}^n\end{bmatrix} = \mathbf{R}_b^n \begin{bmatrix}u^b\\ v^b\\ w^b\end{bmatrix}$$

For rotation motion, the relationship between BODY and NWU is given by

$$\begin{bmatrix}\dot{\phi}_{nb}\\ \dot{\theta}_{nb}\\ \dot{\psi}_{nb}\end{bmatrix} = \begin{bmatrix}1 & \mathrm{s}\phi_{nb}\mathrm{t}\theta_{nb} & \mathrm{c}\phi_{nb}\mathrm{t}\theta_{nb}\\ 0 & \mathrm{c}\phi_{nb} & -\mathrm{s}\phi_{nb}\\ 0 & \mathrm{s}\phi_{nb}/\mathrm{c}\theta_{nb} & \mathrm{c}\phi_{nb}/\mathrm{c}\theta_{nb}\end{bmatrix} \begin{bmatrix}p^b\\ q^b\\ r^b\end{bmatrix}$$

where $\mathrm{t}\cdot = \tan(\cdot)$.

4.3.2 Transformation between BODY and WHEEL

A vector $\mathbf{p}^b$ in BODY can be transformed into a vector $\mathbf{p}^{FL}$ in the front left WHEEL coordinate system by means of a rotation matrix

$$\mathbf{p}^{FL} = \mathbf{R}_b^{FL}\mathbf{p}^b \tag{4.4}$$

where $\mathbf{R}_b^{FL}$ is the rotation matrix which includes the steering angle δ. It can be written as follows

$$\mathbf{R}_b^{FL} = \begin{bmatrix}\cos(\delta) & \sin(\delta) & 0\\ -\sin(\delta) & \cos(\delta) & 0\\ 0 & 0 & 1\end{bmatrix} \tag{4.5}$$

If the steering angle for both the front wheels are assumed equal, the front left WHEEL frame is identical to the front right WHEEL frame such that $\mathbf{R}_b^{FR}$ = $\mathbf{R}_b^{FL}$. In addition, because only the front wheels are used for turning; $\mathbf{R}_b^{RL}$ = $\mathbf{R}_b^{RR}$ = $\mathbf{I}_{3\times3}$. In other words, the orientation of the WHEEL frame for the rear wheels coincide with the BODY frame.

4.4 Rigid Body Kinetics

The derivation of the equations of motions for a general body starts with Euler's first and second axioms

$$\frac{{}^n\mathrm{d}}{\mathrm{d}t}\vec{p}_b = \vec{f}_b \qquad \vec{p}_b = m\vec{v}_{nb} \tag{4.6}$$

$$\frac{{}^n\mathrm{d}}{\mathrm{d}t}\vec{h}_b = \vec{m}_b \qquad \vec{h}_b = I_{CG}\vec{\omega}_{nb} \tag{4.7}$$

where $\vec{f}_b$ and $\vec{m}_b$ are the forces and moments acting on the body's center of gravity, $\vec{\omega}_{nb}$ is the angular velocity of the body with respect to NWU. ${}^n\mathrm{d}/\mathrm{d}t$ means the time differentiation

in the NWU frame.
Following the derivation in [14], the vehicle rigid body kinetics can be expressed as

$$m(\dot{\boldsymbol{\nu}}_{\mathbf{1}} + \mathbf{S}(\boldsymbol{\nu}_{\mathbf{2}})\boldsymbol{\nu}_{\mathbf{1}}) = \boldsymbol{\tau}_1 \tag{4.8}$$

$$\mathbf{I_{CG}}\dot{\boldsymbol{\nu}}_{\mathbf{2}} - \mathbf{S}(\mathbf{I_{CG}}\boldsymbol{\nu}_{\mathbf{2}})\boldsymbol{\nu}_{\mathbf{2}} = \boldsymbol{\tau}_{\mathbf{2}} \tag{4.9}$$

where $\boldsymbol{\nu}_{\mathbf{1}}$ = $[u, v, w]^T$, $\boldsymbol{\nu}_{\mathbf{2}}$ = $[p, q, r]^T$, $\boldsymbol{\tau}_{\mathbf{1}}$ = $[X, Y, Z]^T$, $\boldsymbol{\tau}_{\mathbf{2}}$ = $[L, M, N]^T$, $\mathbf{I_{CG}}$ is the inertia matrix and S is a skew symmetric matrix. The resulting 6 degree of freedom(DOF) model is written

$$\mathbf{M}_{RB}\dot{\boldsymbol{\nu}} + \mathbf{C}_{RB}\boldsymbol{\nu} = \boldsymbol{\tau}_{RB} \tag{4.10}$$

where

$$\mathbf{M}_{RB} = \begin{bmatrix} m\mathbf{I}_{3\times3} & \mathbf{0}_{3\times3} \\ \mathbf{0}_{3\times3} & \mathbf{I_{CG}} \end{bmatrix} \tag{4.11}$$

is the rigid body inertia matrix. Where $\mathbf{0}_{3\times3}$ is a square zero matrix of dimension three. The Coriolis matrix is as follows

$$\mathbf{C}_{RB} = \begin{bmatrix} m\mathbf{S}(\boldsymbol{\nu}_{\mathbf{2}}) & \mathbf{0}_{3\times3} \\ \mathbf{0}_{3\times3} & -\mathbf{S}(\mathbf{I_{CG}}\boldsymbol{\nu}_{\mathbf{2}}) \end{bmatrix} \tag{4.12}$$

In these equations it is assumed that the body reference system is located at the center of gravity.

Assuming xz-plane symmetry (I_{xy} = I_{yz} = 0) the inertia matrix is defined

$$\mathbf{I_{CG}} := \begin{bmatrix} I_{xx} & 0 & -I_{xz} \\ 0 & I_{yy} & 0 \\ I_{xz} & 0 & I_{zz} \end{bmatrix} \tag{4.13}$$

where I_{xx}, I_{yy} and I_{zz} are the moments of inertia about the body x, y and z axes, and I_{xz} is the product of inertia defined as

$$\begin{aligned} I_{xx} &:= \int_V (y^2 + z^2)\rho_m \mathrm{d}V \\ I_{yy} &:= \int_V (x^2 + z^2)\rho_m \mathrm{d}V \\ I_{zz} &:= \int_V (x^2 + y^2)\rho_m \mathrm{d}V \\ I_{xz} &:= \int_V (xz)\rho_m \mathrm{d}V \end{aligned}$$

The forces and moments acting on the body can be expressed as

$$\boldsymbol{\tau}_{RB} = -\mathrm{g}(\boldsymbol{\eta}) + \boldsymbol{\tau} \tag{4.14}$$

where $\boldsymbol{\tau}$ includes the drag, rolling resistance and wheel force and moments defined as

$$\boldsymbol{\tau} := \boldsymbol{\tau}_D + \boldsymbol{\tau}_r + \boldsymbol{\tau}_w \tag{4.15}$$

and g($\boldsymbol{\eta}$) is the force of gravity. The gravity force is given in the body reference frame by

$$\mathbf{g}(\boldsymbol{\eta}) = -(\mathbf{R}_b^n)^T \begin{bmatrix} 0 \\ 0 \\ -mg \\ 0 \\ 0 \\ 0 \end{bmatrix} = \begin{bmatrix} -mg\sin(\theta) \\ mg\cos(\theta)\sin(\phi) \\ mg\cos(\theta)\cos(\phi) \\ 0 \\ 0 \\ 0 \end{bmatrix} \tag{4.16}$$

The 6 DOF model can now be written in matrix form

$$\mathbf{M}_{RB}\dot{\boldsymbol{\nu}} + \mathbf{C}_{RB}\boldsymbol{\nu} + \mathbf{g}(\boldsymbol{\eta}) = \boldsymbol{\tau} \tag{4.17}$$

or in component form:

$$\begin{aligned} m(\dot{u} + qw - rv - g\sin(\theta)) &= X \\ m(\dot{v} + ur - wp + g\cos(\theta)\sin(\phi)) &= Y \\ m(\dot{w} + vp - qu + g\cos(\theta)\cos(\phi)) &= Z \\ I_{xx}\dot{p} - I_{xz}(\dot{r} + pq) + (I_{zz} - I_{yy})qr &= L \\ I_{yy}\dot{q} - I_{xz}(p^2 - r^2) + (I_{xx} - I_{zz})pr &= M \\ I_{zz}\dot{r} - I_{xz}\dot{p} + (I_{yy} - I_{xx})pq + I_{xz}qr &= N \end{aligned} \tag{4.18}$$

The models in this thesis will be expressed in the BODY axes. Since the equations in (4.18) are derived in a general body, they still hold for the BODY axes. In the remainder of the thesis all the forces, moments and velocities will be in the BODY axes and the position and attitude relative to the NWU system. Thus the following definitions is made

$$\boldsymbol{\eta} = \begin{bmatrix} x \\ y \\ z \\ \phi \\ \theta \\ \psi \end{bmatrix} := \begin{bmatrix} x^n \\ y^n \\ z^n \\ \phi_{nb} \\ \theta_{nb} \\ \psi_{nb} \end{bmatrix} \tag{4.19}$$

$$\boldsymbol{\nu} = \begin{bmatrix} u \\ v \\ w \\ p \\ q \\ r \end{bmatrix} := \begin{bmatrix} u^b \\ v^b \\ w^b \\ p^b \\ q^b \\ r^b \end{bmatrix} \tag{4.20}$$

$$\boldsymbol{\nu} = \begin{bmatrix} X \\ Y \\ Z \\ L \\ M \\ N \end{bmatrix} := \begin{bmatrix} X^b \\ Y^b \\ Z^b \\ L^b \\ M^b \\ N^b \end{bmatrix} \tag{4.21}$$

5 Modelling

There are many ways to model vehicle dynamics, but often it is useful to make simple models while still preserving the main behaviour of the system. Because the model in this thesis will be used for vehicle control with large sideslip angles, the model accuracy for large vehicle sideslip angles is paramount.

A nonlinear model will be used, because linear models of vehicle dynamics assume small sideslip angles. The nonlinear two-track model described below was implemented in [5]. And it will be used in this thesis due to good results in comparisons between model simulations and physical vehicle tests done on the LocalBug in [5].

The nonlinear two-track model is described in the following section. Motor and driveline model is presented in section 5.2. Wheel torque model for the vehicle is described in section 5.3. In section 5.4, the servo model used for the vehicle is described. Lastly, in section 5.5, the control allocation is presented.

5.1 Nonlinear Two-Track Model

The nonlinear two-track simulator is a 6 DOF model, which is affected by wind forces and rolling resistance. The model states are velocity in vehicle BODY axes and rates about the vehicle BODY axes.

The vehicle body kinetics derived in section 4.4, are used as a foundation for the two-track simulator model. The forces and moments acting on the vehicle need to be found to complete the model.

By assuming low normal velocities, the drag forces only act along the longitudinal and lateral axis of the vehicle. Thus the drag forces can be expressed as

$$\boldsymbol{\tau}_D = \begin{bmatrix} X_D \\ Y_D \\ Z_D \\ L_D \\ M_D \\ N_D \end{bmatrix} = \begin{bmatrix} -\frac{1}{2}\rho u^2 \text{sgn}(u) A_f C_D \\ -\frac{1}{2}\rho v^2 \text{sgn}(v) A_s C_D \\ 0 \\ 0 \\ 0 \\ 0 \end{bmatrix} \tag{5.1}$$

where ρ is air pressure, A_f and A_s are front and side projected areas and C_D is the drag coefficient. The function sgn(·) is the sign function, and is defined as

$$\operatorname{sgn}(a) = \begin{cases} 1 & \text{for} \quad a > 0 \\ -1 & \text{for} \quad a < 0 \end{cases} \tag{5.2}$$

The rolling resistance is due to several effects, but according to [16], the most dominating are

1. Energy loss from deflection of the tire sidewall near wheel and ground contact area
2. Energy loss from deflection of the contact point between wheel and ground contact area
3. Scrubbing in contact area between wheel and ground
4. Tire longitudinal and lateral slip
5. Deflection of the road surface
6. Air drag on the inside and outside of the tire
7. Energy loss on bumps

The rolling resistance can be expressed as

$$\boldsymbol{\tau}_r = \begin{bmatrix} X_r \\ Y_r \\ Z_r \\ L_r \\ M_r \\ N_r \end{bmatrix} = \begin{bmatrix} -mguC_r \\ 0 \\ 0 \\ 0 \\ 0 \\ 0 \end{bmatrix} \tag{5.3}$$

where C_r is the rolling coefficient.

Lastly the wheel forces and moments need to be expressed. These can be written as

$$\boldsymbol{\tau}_w = \begin{bmatrix} X_w \\ Y_w \\ Z_w \\ L_w \\ M_w \\ N_w \end{bmatrix} = \begin{bmatrix} X_{FL} + X_{FR} + X_{RL} + X_{RR} \\ Y_{FL} + Y_{FR} + Y_{RL} + Y_{RR} \\ Z_{FL} + Z_{FR} + Z_{RL} + Z_{RR} \\ L_{FL} + L_{FR} + L_{RL} + L_{RR} \\ M_{FL} + M_{FR} + M_{RL} + M_{RR} \\ N_{FL} + N_{FR} + N_{RL} + N_{RR} \end{bmatrix} \tag{5.4}$$

The forces acting from the wheels need to be rotated from WHEEL to BODY coordinate system. Steering angle δ for the front wheels are assumed equal. Using the rotation matrix in equation (4.5), the wheel forces acting on the body from the tires are

$$\begin{bmatrix} X_{FL} \\ Y_{FL} \\ Z_{FL} \end{bmatrix} = (\mathbf{R}_b^{FL})^T \begin{bmatrix} X_{FL}^{FL} \\ Y_{FL}^{FL} \\ Z_{FL}^{FL} \end{bmatrix} \tag{5.5}$$

$$\begin{bmatrix} X_{FR} \\ Y_{FR} \\ Z_{FR} \end{bmatrix} = (\mathbf{R}_b^{FR})^T \begin{bmatrix} X_{FR}^{FR} \\ Y_{FR}^{FR} \\ Z_{FR}^{FR} \end{bmatrix} \tag{5.6}$$

$$\begin{bmatrix} X_{RL} \\ Y_{RL} \\ Z_{RL} \end{bmatrix} = \begin{bmatrix} X_{RL}^{RL} \\ Y_{RL}^{RL} \\ Z_{RL}^{RL} \end{bmatrix} \tag{5.7}$$

$$\begin{bmatrix} X_{RR} \\ Y_{RR} \\ Z_{RR} \end{bmatrix} = \begin{bmatrix} X_{RR}^{RR} \\ Y_{RR}^{RR} \\ Z_{RR}^{RR} \end{bmatrix} \tag{5.8}$$

And the moments acting on the body can be written as

$$\begin{bmatrix} L_w \\ M_w \\ N_w \end{bmatrix} = \begin{bmatrix} l_f \\ \frac{b}{2} \\ -h_{CG} \end{bmatrix} \times \begin{bmatrix} X_{FL} \\ Y_{FL} \\ Z_{FL} \end{bmatrix} + \begin{bmatrix} l_f \\ -\frac{b}{2} \\ -h_{CG} \end{bmatrix} \times \begin{bmatrix} X_{FR} \\ Y_{FR} \\ Z_{FR} \end{bmatrix} + \begin{bmatrix} -l_r \\ \frac{b}{2} \\ -h_{CG} \end{bmatrix} \times \begin{bmatrix} X_{RL} \\ Y_{RL} \\ Z_{RL} \end{bmatrix} + \begin{bmatrix} -l_r \\ -\frac{b}{2} \\ -h_{CG} \end{bmatrix} \times \begin{bmatrix} X_{RR} \\ Y_{RR} \\ Z_{RR} \end{bmatrix} \tag{5.9}$$

where l_f, l_r are distance between vehicle center of gravity and front axle and rear axle respectively. The constant h_{CG} is distance between ground and center of gravity and b is the distance between two wheels on the same axle. By inserting equation (5.5) to (5.8), equation (5.9) becomes

$$\begin{aligned} \begin{bmatrix} L_w \\ M_w \\ N_w \end{bmatrix} = {} & \begin{bmatrix} l_f \\ \frac{b}{2} \\ -h_{CG} \end{bmatrix} \times \left((\mathbf{R}_b^{FL})^T \begin{bmatrix} X_{FL}^{FL} \\ Y_{FL}^{FL} \\ Z_{FL}^{FL} \end{bmatrix} \right) + \begin{bmatrix} l_f \\ -\frac{b}{2} \\ -h_{CG} \end{bmatrix} \times \left((\mathbf{R}_b^{FR})^T \begin{bmatrix} X_{FR}^{FR} \\ Y_{FR}^{FR} \\ Z_{FR}^{FR} \end{bmatrix} \right) \\ & + \begin{bmatrix} -l_r \\ \frac{b}{2} \\ -h_{CG} \end{bmatrix} \times \begin{bmatrix} X_{RL}^{RL} \\ Y_{RL}^{RL} \\ Z_{RL}^{RL} \end{bmatrix} + \begin{bmatrix} -l_r \\ -\frac{b}{2} \\ -h_{CG} \end{bmatrix} \times \begin{bmatrix} X_{RR}^{RR} \\ Y_{RR}^{RR} \\ Z_{RR}^{RR} \end{bmatrix} \end{aligned} \tag{5.10}$$

Gathering the equations (5.5) to (5.8) and (5.10), gives the component form of the wheel forces and moments

$$
\begin{aligned}
X_w &= (X_{FL}^{FL} + X_{FR}^{FR})\cos(\delta) - (Y_{FL}^{FL} + Y_{FR}^{FR})\sin(\delta) + X_{RL}^{RL} + X_{RR}^{RR} && (5.11)\\
Y_w &= (Y_{FL}^{FL} + Y_{FR}^{FR})\cos(\delta) + (X_{FL}^{FL} + X_{FR}^{FR})\sin(\delta) + Y_{RL}^{RL} + Y_{RR}^{RR} && (5.12)\\
Z_w &= Z_{FL}^{FL} + Z_{FR}^{FR} + Z_{RL}^{RL} + Z_{RR}^{RR} && (5.13)\\
L_w &= h_{CG}((Y_{FL}^{FL} + Y_{FR}^{FR})\cos(\delta) + (X_{FL}^{FL} + X_{FR}^{FR})\sin(\delta) + Y_{RL}^{RL} + Y_{RR}^{RR})\\
&\quad + \frac{b}{2}(Z_{FL}^{FL} - Z_{FR}^{FR} + Z_{RL}^{RL} - Z_{RR}^{RR}) && (5.14)\\
M_w &= -h_{CG}((X_{FL}^{FL} + X_{FR}^{FR})\cos(\delta) - (Y_{FL}^{FL} + Y_{FR}^{FR})\sin(\delta) + X_{RL}^{RL} + X_{RR}^{RR}) - l_f(Z_{FL}^{FL} + Z_{FR}^{FR})\\
&\quad + l_r(Z_{RL}^{RL} + Z_{RR}^{RR}) && (5.15)\\
N_w &= l_f((Y_{FL}^{FL} + Y_{FR}^{FR})\cos(\delta) + (X_{FL}^{FL} + X_{FR}^{FR})\sin(\delta)) - l_r(Y_{RL}^{RL} + Y_{RR}^{RR})\\
&\quad + \frac{b}{2}((X_{FR}^{FR} - X_{FL}^{FL})\cos(\delta) - (Y_{FR}^{FR} - Y_{FL}^{FL})\sin(\delta) + X_{RR}^{RR} - X_{RL}^{RL}) && (5.16)
\end{aligned}
$$

where X_{FL}^{FL}, X_{FR}^{FR}, X_{RL}^{RL} and X_{RR}^{RR} are inputs for all wheel driven (AWD), X_{FL}^{FL} and X_{FR}^{FR} are inputs for FWD and X_{RL}^{RL} and X_{RR}^{RR} are inputs for RWD.

The sum of the forces are

$$
\begin{aligned}
m\dot{u} &= (X_{FL}^{FL} + X_{FR}^{FR})\cos(\delta) - (Y_{FL}^{FL} + Y_{FR}^{FR})\sin(\delta) + X_{RL}^{RL} + X_{RR}^{RR}\\
&\quad - \frac{1}{2}\rho u^2 \text{sgn}(u) A_f C_D + m(rv - qw - C_r g u + g\sin(\theta)) && (5.17)\\
m\dot{v} &= (X_{FL}^{FL} + X_{FR}^{FR})\sin(\delta) + (Y_{FL}^{FL} + Y_{FR}^{FR})\cos(\delta) + Y_{RL}^{RL} + Y_{RR}^{RR}\\
&\quad - \frac{1}{2}\rho v^2 \text{sgn}(v) A_s C_D + m(wp - ur - g\cos(\theta)\sin(\phi)) && (5.18)\\
m\dot{w} &= Z_{FL}^{FL} + Z_{FR}^{FR} + Z_{RL}^{RL} + Z_{RR}^{RR} + m(qu - vp - g\cos(\theta)\cos(\phi)) && (5.19)\\
I_{xx}\dot{p} &= h_{CG}((Y_{FL}^{FL} + Y_{FR}^{FR})\cos(\delta) + (X_{FL}^{FL} + X_{FR}^{FR})\sin(\delta) + Y_{RL}^{RL} + Y_{RR}^{RR})\\
&\quad + \frac{b}{2}(Z_{FL}^{FL} - Z_{FR}^{FR} + Z_{RL}^{RL} - Z_{RR}^{RR}) + (I_{yy} - I_{zz})qr && (5.20)\\
I_{yy}\dot{q} &= -h_{CG}((X_{FL}^{FL} + X_{FR}^{FR})\cos(\delta) - (Y_{FL}^{FL} + Y_{FR}^{FR})\sin(\delta) + X_{RL}^{RL} + X_{RR}^{RR}) - l_f(Z_{FL}^{FL} + Z_{FR}^{FR})\\
&\quad + l_r(Z_{RL}^{RL} + Z_{RR}^{RR}) + (I_{zz} - I_{xx})pr && (5.21)\\
I_{zz}\dot{r} &= l_f(Y_{FL}^{FL} + Y_{FR}^{FR})\cos(\delta) + l_f(X_{FL}^{FL} + X_{FR}^{FR})\sin(\delta) + \frac{b}{2}(X_{FR}^{FR} - X_{FL}^{FL})\cos(\delta)\\
&\quad - \frac{b}{2}(Y_{FR}^{FR} - Y_{FL}^{FL})\sin(\delta) + \frac{b}{2}(X_{RR}^{RR} - X_{RL}^{RL}) - l_r(Y_{RL}^{RL} + Y_{RR}^{RR}) + (I_{xx} - I_{yy})pq && (5.22)
\end{aligned}
$$

Note here that I_{xz} has been omitted from the equations in (4.18). A flat road surface is assumed, with roll and pitch angles put to zero leading to

$$
\begin{aligned}
\sin(\theta) &\approx 0 & \cos(\theta) &\approx 1 && (5.23)\\
\sin(\phi) &\approx 0 & \cos(\phi) &\approx 1 && (5.24)\\
r &\approx \dot{\psi} & \dot{r} &\approx \ddot{\psi} && (5.25)
\end{aligned}
$$

This assumption leads to errors in the gravitation vector during physical tests when the surface has an inclination. By using equation (5.23), (5.24) and (5.25), the resulting model is

$$\begin{aligned}
m\dot{u} &= (X_{FL}^{FL} + X_{FR}^{FR})\cos(\delta) - (Y_{FL}^{FL} + Y_{FR}^{FR})\sin(\delta) + X_{RL}^{RL} + X_{RR}^{RR} \\
&\quad - \frac{1}{2}\rho u^2 \mathrm{sgn}(u) A_f C_D + m(\dot{\psi} v - qw - C_r g u) && (5.26)\\
m\dot{v} &= (X_{FL}^{FL} + X_{FR}^{FR})\sin(\delta) + (Y_{FL}^{FL} + Y_{FR}^{FR})\cos(\delta) + Y_{RL}^{RL} + Y_{RR}^{RR} \\
&\quad - \frac{1}{2}\rho v^2 \mathrm{sgn}(v) A_s C_D + m(wp - u\dot{\psi}) && (5.27)\\
m\dot{w} &= Z_{FL}^{FL} + Z_{FR}^{FR} + Z_{RL}^{RL} + Z_{RR}^{RR} + m(qu - vp - g) && (5.28)\\
I_{xx}\dot{p} &= h_{CG}((Y_{FL}^{FL} + Y_{FR}^{FR})\cos(\delta) + (X_{FL}^{FL} + X_{FR}^{FR})\sin(\delta) + Y_{RL}^{RL} + Y_{RR}^{RR}) \\
&\quad + \frac{b}{2}(Z_{FL}^{FL} - Z_{FR}^{FR} + Z_{RL}^{RL} - Z_{RR}^{RR}) + (I_{yy} - I_{zz})q\dot{\psi} && (5.29)\\
I_{yy}\dot{q} &= -h_{CG}((X_{FL}^{FL} + X_{FR}^{FR})\cos(\delta) - (Y_{FL}^{FL} + Y_{FR}^{FR})\sin(\delta) + X_{RL}^{RL} + X_{RR}^{RR}) - l_f(Z_{FL}^{FL} + Z_{FR}^{FR}) \\
&\quad + l_r(Z_{RL}^{RL} + Z_{RR}^{RR}) + (I_{zz} - I_{xx})p\dot{\psi} && (5.30)\\
I_{zz}\ddot{\psi} &= l_f(Y_{FL}^{FL} + Y_{FR}^{FR})\cos(\delta) + l_f(X_{FL}^{FL} + X_{FR}^{FR})\sin(\delta) + \frac{b}{2}(X_{FR}^{FR} - X_{FL}^{FL})\cos(\delta) \\
&\quad - \frac{b}{2}(Y_{FR}^{FR} - Y_{FL}^{FL})\sin(\delta) + \frac{b}{2}(X_{RR}^{RR} - X_{RL}^{RL}) - l_r(Y_{RL}^{RL} + Y_{RR}^{RR}) + (I_{xx} - I_{yy})pq && (5.31)
\end{aligned}$$

The wheel axis forces are connected to the wheel velocity vector frame by

$$\begin{bmatrix} X_{(\cdot)}^{(\cdot)} \\ Y_{(\cdot)}^{(\cdot)} \end{bmatrix} = \begin{bmatrix} \cos(\alpha_{(\cdot)}) & \sin(\alpha_{(\cdot)}) \\ -\sin(\alpha_{(\cdot)}) & \cos(\alpha_{(\cdot)}) \end{bmatrix} \begin{bmatrix} \mu_{(\cdot)}^{long} Z_{(\cdot)}^{b} \\ \mu_{(\cdot)}^{lat} Z_{(\cdot)}^{b} \end{bmatrix} \tag{5.32}$$

where $(\cdot)$ can be FL, FR, RL or RR. The parameters $\mu_{(\cdot)}^{long}$ and $\mu_{(\cdot)}^{lat}$ are the friction coefficients in longitudinal wheel speed direction and lateral wheel speed direction respectively. And $\alpha_{(\cdot)}$ are the wheel slip angles shown in figure 5.1, and are calculated as

$$\alpha_{FL} = \delta - \arctan\left(\frac{v + \dot{\psi} r_{FL}\cos(\vartheta_{FL})}{u - \dot{\psi} r_{FL}\sin(\vartheta_{FL})}\right) \tag{5.33}$$

$$\alpha_{FR} = \delta - \arctan\left(\frac{v + \dot{\psi} r_{FR}\sin(\vartheta_{FR})}{u + \dot{\psi} r_{FR}\cos(\vartheta_{FR})}\right) \tag{5.34}$$

$$\alpha_{RL} = -\arctan\left(\frac{v - \dot{\psi} r_{RL}\sin(\vartheta_{RL})}{u - \dot{\psi} r_{RL}\cos(\vartheta_{RL})}\right) \tag{5.35}$$

$$\alpha_{RR} = -\arctan\left(\frac{v - \dot{\psi} r_{RR}\cos(\vartheta_{RR})}{u + \dot{\psi} r_{RR}\sin(\vartheta_{RR})}\right) \tag{5.36}$$

where

$$\vartheta_{FL} = \arctan(\frac{b/2}{l_f}), \qquad r_{FL} = \sqrt{l_f^2 + \frac{b^2}{4}} \tag{5.37}$$

$$\vartheta_{FR} = \arctan(\frac{l_f}{b/2}), \qquad r_{FR} = r_{FL} \tag{5.38}$$

$$\vartheta_{RL} = \arctan(\frac{l_r}{b/2}), \qquad r_{RL} = \sqrt{l_r^2 + \frac{b^2}{4}} \tag{5.39}$$

$$\vartheta_{RR} = \arctan(\frac{b/2}{l_r}), \qquad r_{RR} = r_{RL} \tag{5.40}$$

The constants r_{FL}, r_{FR}, r_{RL} and r_{RR} are the distance between center of gravity and front left wheel, front right wheel, rear left wheel and rear right wheel respectively, shown in figure 5.2. And the angle between center of gravity and front left wheel, front right wheel, rear left wheel and rear right wheel are ϑ_{FL}, ϑ_{FR}, ϑ_{RL} and ϑ_{RR} respectively, seen in figure 5.2.

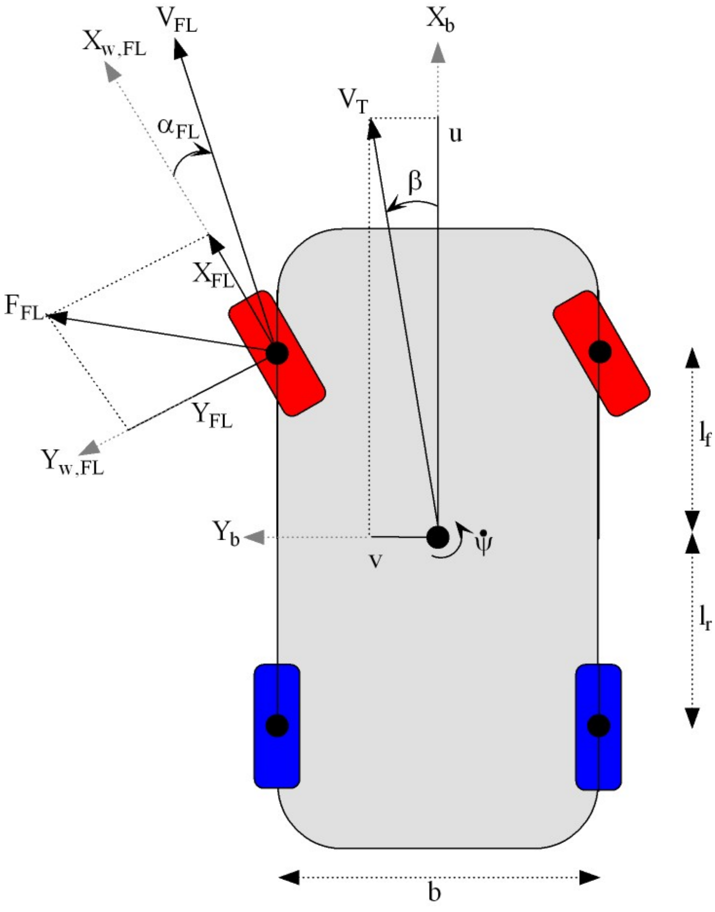

Figure 5.1: Vehicle slip angle and sideslip angle.

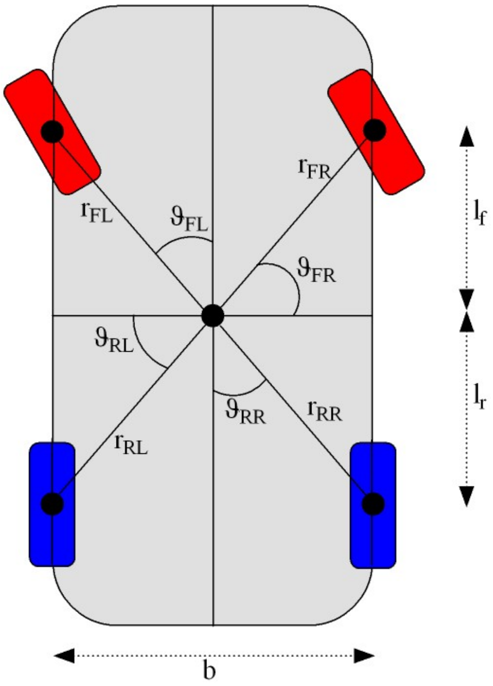

Figure 5.2: Vehicle angles and distances from center of gravity to wheels.

The friction coefficients $\mu_{(\cdot)}^{long}$ and $\mu_{(\cdot)}^{lat}$ are found using the Burckhardt method described in [17]. The Burckhardt method uses a model on the form

$$\mu_{(\cdot)}^{long} = \mu_{(\cdot)} \frac{s_{(\cdot)}^{long}}{s_{(\cdot)}^{Res}} \tag{5.41}$$

$$\mu_{(\cdot)}^{lat} = \mu_{(\cdot)} \frac{s_{(\cdot)}^{lat}}{s_{(\cdot)}^{Res}} \tag{5.42}$$

$$\mu_{(\cdot)} = (c_1(1 - e^{-c_2 s_{(\cdot)}^{Res}}) - c_3 s_{(\cdot)}^{Res})e^{-c_4 s_{(\cdot)}^{Res} V_T} \tag{5.43}$$

where constants c_1, c_2, c_3 and c_4 vary with road surface, $(\cdot)$ can be FL, FR, RL or RR, and $s_{(\cdot)}^{long}$, $s_{(\cdot)}^{lat}$ and $s_{(\cdot)}^{Res}$ are the longitudinal, lateral and resultant wheel slip. A mathematical description of the resultant slip is $s_{(\cdot)}^{Res} = \sqrt{(s_{(\cdot)}^{long})^2 + (s_{(\cdot)}^{lat})^2}$.

The wheel slips are differently expressed for breaking and driving wheels. Slipping of the breaking and free rolling wheels can be written as

$$s_{(\cdot)}^{long} = \frac{V_{R,(\cdot)} \cos(\alpha_{(\cdot)}) - V_{W,(\cdot)}}{V_{W,(\cdot)}} \tag{5.44}$$

$$s_{(\cdot)}^{lat} = \frac{V_{R,(\cdot)} \sin(\alpha_{(\cdot)})}{V_{W,(\cdot)}} \tag{5.45}$$

and for driving wheels

$$s^{long}_{(\,\cdot\,)} = \frac{V_{R,(\,\cdot\,)}\cos(\alpha_{(\,\cdot\,)}) - V_{W,(\,\cdot\,)}}{V_{R,(\,\cdot\,)}\cos(\alpha_{(\,\cdot\,)})} \tag{5.46}$$

$$s^{lat}_{(\,\cdot\,)} = \tan(\alpha_{(\,\cdot\,)}) \tag{5.47}$$

as above $(\,\cdot\,)$ can be FL, FR, RL or RR. The rotational equivalent velocity $V_{R,(\,\cdot\,)}$ is

$$V_{R,(\,\cdot\,)} = \omega_{(\,\cdot\,)} r_w \tag{5.48}$$

where r_w is the radius from the wheel center point to wheel contact point and $\omega_{(\,\cdot\,)}$ is the angular velocity of the wheel. And the ground wheel contact point velocities are

$$V_{W,FL} = \sqrt{u^2 + v^2 + 2\dot{\psi} r_{FL}(v\cos(\vartheta_{FL}) - u\sin(\vartheta_{FL})) + \dot{\psi}^2 r_{FL}^2} \tag{5.49}$$

$$V_{W,FR} = \sqrt{u^2 + v^2 + 2\dot{\psi} r_{FR}(u\cos(\vartheta_{FR}) + v\sin(\vartheta_{FR})) + \dot{\psi}^2 r_{FR}^2} \tag{5.50}$$

$$V_{W,RL} = \sqrt{u^2 + v^2 - 2\dot{\psi} r_{RL}(u\cos(\vartheta_{RL}) + v\sin(\vartheta_{RL})) + \dot{\psi}^2 r_{RL}^2} \tag{5.51}$$

$$V_{W,RR} = \sqrt{u^2 + v^2 + 2\dot{\psi} r_{RR}(u\sin(\vartheta_{RR}) - v\cos(\vartheta_{RR})) + \dot{\psi}^2 r_{RR}^2} \tag{5.52}$$

When deriving the wheel normal forces it is assumed that there is no suspension dynamics and the coupling between roll and pitch is neglected. By following the derivation in [17], the normal forces can be written as

$$Z_{fl} = -m(\frac{l_r g - h_{CG}\dot{u}}{l}) \cdot (0.5 - \frac{h_{CG}\dot{v}}{bg}) \tag{5.53}$$

$$Z_{fr} = -m(\frac{l_r g - h_{CG}\dot{u}}{l}) \cdot (0.5 + \frac{h_{CG}\dot{v}}{bg}) \tag{5.54}$$

$$Z_{rl} = -m(\frac{l_f g + h_{CG}\dot{u}}{l}) \cdot (0.5 - \frac{h_{CG}\dot{v}}{bg}) \tag{5.55}$$

$$Z_{rr} = -m(\frac{l_f g + h_{CG}\dot{u}}{l}) \cdot (0.5 + \frac{h_{CG}\dot{v}}{bg}) \tag{5.56}$$

where l is the distance between the rear axle and the front axle of the vehicle, and can be written as $l = l_f + l_r$.

The normal force equations are derived assuming no coupling between roll and pitch, and no suspension dynamics. However, from driving experience with the LocalBug, the vehicle tends to roll more than regular cars, it also tips over if the driver is too aggressive when cornering. Thus, this assumption should be looked into when improving the simulator.

5.2 Motor and Driveline Modelling

In [5] the motor is modelled with a DC motor model as in [18]

$$L_a \frac{di_a}{dt} = -R_a i_a - k_E \omega_m + u_a \tag{5.57}$$

$$I_m \dot{\omega}_m = k_t i_a - T_L \tag{5.58}$$

The notations are explained below in table 5.1

Table 5.1: Notations for the DC motor model equation

Symbol	Description
i_a	Armature current [A]
u_a	Armature voltage [V]
L_a	Armature inductance [H]
R_a	Armature resistance [Ω]
k_E	Back EMF constant [kgm^2/s]
ω_m	Rotational velocity of the motor shaft [rad/s]
I_m	Inertia of the motor armature [kgm^2]
k_t	Torque constant [Nm/A]
T_L	Load torque [Nm]

The constants in table 5.1 were found in [5] to be

Table 5.2: Values used in the DC motor model

Coefficient	Value
L_a	0.001
R_a	0.8
k_E	0.17
k_t	0.17

The values in table 5.2 are only approximate values, since no extensive testing was done on the DC motor model in [5].

5.3 Wheel Torque Modelling

In the simulator made in [5] it is possible to have open or locked differential, FWD, RWD or AWD. With the differential open, two wheels on the same axle can rotate with different speeds and the motor torque is evenly distributed to all driving wheels. Open differential is useful in corners, when the outer wheels in the curve have longer distance to travel than the inner wheels. A locked differential forces the wheels on the same axle to rotate at the same speed. Below is the derivation from [5] for the wheel torque model.

With the assumption of a rigid driveline with no friction, the torque balance for each wheel from [17] is

$$I_w \dot{\omega}_w = T_{drive} - T_{brake} - r_{eff} X_{fric} \tag{5.59}$$

where T_{drive} is torque from the motor, $r_{eff} X_{fric}$ is the torque from friction between the road surface and the tires, T_{brake} is the breaking torque. The Localbug has no dedicated breaks, such that T_{brake} = 0.

When the driveline is rigid and there is no friction, the drive torque, T_{drive} is equal to the load torque, T_L. Equation 5.58 can be rewritten by substituting 5.59, this yields

$$I_m \dot{\omega}_m + I_w \dot{\omega}_w = T_{drive} - r_{eff} X_{fric} \tag{5.60}$$

With a rigid driveline ω_m = ω_w, which gives

$$(I_m + I_w) \dot{\omega}_w = T_{drive} - r_{eff} X_{fric} \tag{5.61}$$

In [5], an open differential, with the wheels rotating at different speeds, the motor speed is the average of the angular velocity of the driving wheels.

For an open differential the torque balance for each driving wheels becomes

$$(I_w + \frac{I_m}{n}) \dot{\omega}_w = \frac{T_{drive}}{n} - r_{eff} X_{fric} \tag{5.62}$$

where n is the number of driving wheels. The free rolling tires do not have any driving torque, and are not affected by the motor, only friction, hence

$$I_w \dot{\omega}_w = -r_{eff} X_{fric} \tag{5.63}$$

The model in [5] does not take into account the affects that occur when one wheel is spinning while the others retain traction. However, because the simulator is not able to simulate different road conditions for each wheel, the simplification can be considered acceptable.

For a locked differential the torque balance for each driving wheel becomes

$$(2I_w + \frac{I_m}{m})\dot{\omega}_w = \frac{T_{drive}}{m} - r_{eff}(X_{fric,left} + X_{fric,right}) \tag{5.64}$$

where m is the number of axles connected to the motor. The model in (5.63) is used for the free rolling tires.

In this thesis the LocalBug will be RWD with a locked differential, which means that equation (5.64) is used with m = 1, resulting in

$$\dot{\omega}_w = \frac{1}{2I_w + I_m}\Big(T_{drive} - r_{eff}(X_{fric,left} + X_{fric,right})\Big) \tag{5.65}$$

5.4 Servo Model

The servo model only consists of a low-pass filter to limit the steering angle rate. A low-pass filter is on the form

$$h_{lowpass} = \frac{K}{Ts + 1} \tag{5.66}$$

where the gain K = 1 and time constant T = 0.001 was used for the simulator. This filter has a weak low-pass filtering effect due to the low time constant, only asymptotically reducing the magnitude above $\frac{1}{T}$ = 1000 $\frac{rad}{s}$.

5.5 Control Allocation

The control allocation for the model consists of a mapping between the forces produced by the actuators and the inputs to the vehicle, which are the steering angle and the throttle. A control allocation method developed for the LocalBug simulator in [5], will be used for this thesis.

Mapping between the forces produced by the actuators and the inputs to the system can be written as [14]

$$\mathbf{f} = \mathbf{K}\mathbf{u} \tag{5.67}$$

where f is the forces produced by the actuators, $\mathbf{K}$ is the force coefficient matrix and u is the control inputs. For a steering angle δ the forces from the front wheels will be rotated compared to the vehicle BODY axis. Now by defining the virtual control input τ, the relationship between virtual control inputs and actuator commands can be written as

$$\boldsymbol{\tau} = \mathbf{T}(\delta)\mathbf{f} = \mathbf{T}(\delta)\mathbf{K}\mathbf{u} \tag{5.68}$$

where the thrust and steering configuration matrix $\mathbf{T}(\delta)$ is

$$\mathbf{T}(\delta) = \begin{bmatrix} 1 & -\sin(\delta) \\ 0 & \cos(\delta) \\ 0 & l_f \cos(\delta) \end{bmatrix} \tag{5.69}$$

This leads to the an expression for the control inputs

$$\mathbf{u} = \mathbf{K}^{-1}\mathbf{T}(\delta)^{\dagger}\boldsymbol{\tau} \tag{5.70}$$

where $T(\delta)^{\dagger}$ is the pseudo inverse

$$\mathbf{T}(\delta)^{\dagger} = \left(\mathbf{T}^T\mathbf{T}\right)^{-1}\mathbf{T}^T \tag{5.71}$$

Steering Servo
In [5] a linear relationship between the wheel slip angle and the lateral force on the front wheels is assumed. A linear relationship will only be valid for small slip angles. However, the front wheels will be used for countersteering during the drift and the friction forces will not saturate. Which means that this assumption will be adequate for the control objective.

The linear relationship can be written as

$$Y = C_\alpha \alpha = C_\alpha \left(\delta - \beta - \frac{l_f \dot{\psi}}{V_T}\right) \tag{5.72}$$

where Y is the lateral wheel force produced by the front wheels in the front WHEEL axis and C_α is the cornering coefficient. In [5], the cornering coefficient was found as the gradient of friction slip curve evaluated at zero slip. Throughout this thesis, the vehicle will be running on wet cobblestones with $C_\alpha \approx 12$.

When the desired slip angle α has been found, the steering angle δ can be extracted from the relationship

$$\delta = \alpha + \beta + \frac{l_f \dot{\psi}}{V_T} \tag{5.73}$$

Throttle Servo
From [5], by using the normal load and the friction coefficient, a linear relationship between the produced force and the throttle input can be expressed as

$$X = \frac{\mu Z}{u_{a,max}} u_a \tag{5.74}$$

where X is the longitudinal wheel force produced by the rear wheels, μ is the friction coefficient, Z is the normal force acting on the driving wheels and u_a is the armature voltage as in (5.57).

The friction coefficient can be taken as the peak friction coefficient found in [5]. In this thesis, wet cobblestone will be used as the surface with $\mu = 0.4$. And normal force will be calculated as $Z = mg$. The armature voltage vary with the number of battery cells connected to the LocalBug. A maximum of six cells can be connected at a time, with each cell having a nominal voltage of 4.2, giving a maximum voltage output of 25 volts.

Finally the force coefficient matrix can be written as

$$\mathbf{K} = \begin{bmatrix} \dfrac{\mu Z}{u_{a,max}} & 0 \\ 0 & C_\alpha \end{bmatrix} \tag{5.75}$$

where the front wheels only produce lateral forces and while assuming the rear wheels only produce longitudinal forces.

The vehicle inputs can be written on component form as

$$u_a = \frac{u_{a,max}}{\mu Z} \left(X_w + \frac{\sin(\delta)}{(1 + l_f^2)\cos(\delta)} (Y_w + l_f N_w) \right) \tag{5.76}$$

$$\delta = \frac{1}{C_\alpha (1 + l_f^2)\cos(\delta)} (Y_w + l_f N_w) + \beta + \frac{l_f \dot{\psi}}{V_T} \tag{5.77}$$

Notice that for the armature voltage, the side force Y_w and the yaw moment N_w would dominate the axial force X_w if

$$\frac{\sin(\delta)}{(1 + l_f^2)\cos(\delta)} (Y_w + l_f N_w) > X_w \tag{5.78}$$

Simulator Remark

The nonlinear two-track model described in this chapter was compared against logged data from the LocalBug vehicle [5]. Heavy breaking and acceleration measurements in the simulator were found to be very different from the logged data. With this knowledge, the acceleration measurements will not be used for control in this thesis, and heavy breaking will not be performed.

6 Linearisation

The two-track model described in section 5.1, is highly nonlinear, including control input limitations, thus it can be hard to analyse thoroughly with regards to drifting. Thus it is useful to linearise the system to do the analysis on many linear models, to find feasible steady state values, that do not saturate the control inputs. In addition, the largest yaw rate during a drifting manoeuvre can be found. A stability analysis can also be done for these steady state drifting conditions.

In the following section a linearisation of the simulator described in section 5.1, is performed and the vehicle states at the drifting equilibriums are found in section 6.2.

6.1 Linearisation of Simulator Model

The simulator used in this thesis is made using 6 DOF, however the heave velocity, and the pitch and roll rates are omitted in the linear analysis. The accelerations in vehicle z-axis are used for finding the weight distribution when the vehicle is affected by acceleration. However, in the linear analysis the vehicle is not affected by accelerations and the weight distribution is the same for all wheels.

By using equation (5.32), the wheel forces in the equations (5.11), (5.12) and (5.16) can be expressed as

$$\begin{aligned}
X_w(\alpha,\mu) &= (Z^b_{FL}(\cos(\alpha_{FL})\mu^{long}_{FL} + \sin(\alpha_{FL})\mu^{lat}_{FL}) + Z^b_{FR}(\cos(\alpha_{FR})\mu^{long}_{FR} + \sin(\alpha_{FR})\mu^{lat}_{FR}))\cos(\delta) \\
&\quad - (Z^b_{FL}(-\sin(\alpha_{FL})\mu^{long}_{FL} + \cos(\alpha_{FL})\mu^{lat}_{FL}) + Z^b_{FR}(-\sin(\alpha_{FR})\mu^{long}_{FR} + \cos(\alpha_{FR})\mu^{lat}_{FR}))\sin(\delta) \\
&\quad + X^{RL}_{RL} + X^{RR}_{RR} \qquad (6.1) \\
Y_w(\alpha,\mu) &= (Z^b_{FL}(\cos(\alpha_{FL})\mu^{long}_{FL} + \sin(\alpha_{FL})\mu^{lat}_{FL}) + Z^b_{FR}(\cos(\alpha_{FR})\mu^{long}_{FR} + \sin(\alpha_{FR})\mu^{lat}_{FR}))\sin(\delta) \\
&\quad + (Z^b_{FL}(-\sin(\alpha_{FL})\mu^{long}_{FL} + \cos(\alpha_{FL})\mu^{lat}_{FL}) + Z^b_{FR}(-\sin(\alpha_{FR})\mu^{long}_{FR} + \cos(\alpha_{FR})\mu^{lat}_{FR}))\cos(\delta) \\
&\quad + Z^b_{RL}(-\sin(\alpha_{RL})\mu^{long}_{RL} + \cos(\alpha_{RL})\mu^{lat}_{RL}) + Z^b_{RR}(-\sin(\alpha_{RR})\mu^{long}_{RR} + \cos(\alpha_{RR})\mu^{lat}_{RR}) \\
&\qquad (6.2)
\end{aligned}$$

$$\begin{aligned}
N_w(\alpha,\mu) = {} & l_f(Z^b_{FL}(-\sin(\alpha_{FL})\mu^{long}_{FL} + \cos(\alpha_{FL})\mu^{lat}_{FL}) + Z^b_{FR}(-\sin(\alpha_{FR})\mu^{long}_{FR} + \cos(\alpha_{FR})\mu^{lat}_{FR}))\cos(\delta) \\
& + l_f(Z^b_{FL}(\cos(\alpha_{FL})\mu^{long}_{FL} + \sin(\alpha_{FL})\mu^{lat}_{FL}) + Z^b_{FR}(\cos(\alpha_{FR})\mu^{long}_{FR} + \sin(\alpha_{FR})\mu^{lat}_{FR}))\sin(\delta) \\
& + \frac{b}{2}(Z^b_{FR}(\cos(\alpha_{FR})\mu^{long}_{FR} + \sin(\alpha_{FR})\mu^{lat}_{FR}) - Z^b_{FL}(\cos(\alpha_{FL})\mu^{long}_{FL} + \sin(\alpha_{FL})\mu^{lat}_{FL}))\cos(\delta) \\
& - \frac{b}{2}(Z^b_{FR}(-\sin(\alpha_{FR})\mu^{long}_{FR} + \cos(\alpha_{FR})\mu^{lat}_{FR}) - Z^b_{FL}(-\sin(\alpha_{FL})\mu^{long}_{FL} + \cos(\alpha_{FL})\mu^{lat}_{FL}))\sin(\delta) \\
& + \frac{b}{2}(X^{RR}_{RR} - X^{RL}_{RL}) \\
& - l_r(Z^b_{RL}(-\sin(\alpha_{RL})\mu^{long}_{RL} + \cos(\alpha_{RL})\mu^{lat}_{RL}) + Z^b_{RR}(-\sin(\alpha_{RR})\mu^{long}_{RR} + \cos(\alpha_{RR})\mu^{lat}_{RR}))
\end{aligned} \tag{6.3}$$

Firstly the derivative of the wheel slip angles with respect to u, v, $\dot{\psi}$, δ and $X_R = X^{RR}_{RR} + X^{RL}_{RL}$ were calculate, which were used in the linearisation.

The thrust force from the rear wheels X_R is one of the two inputs to the system, but in a steady state drifting condition $X^{RR}_{RR} \neq X^{RL}_{RL}$. A simplification is done in the following by assuming a change in X_R affects both the rear wheels equally. Thrust will affect the two rear wheels differently, however for small variations in thrust about the equilibrium this assumption will only cause small errors. This simplification can be written as

$$\frac{\partial X^{RR}_{RR}}{\partial X_R} = \frac{\partial X^{RL}_{RL}}{\partial X_R} = \frac{1}{2} \tag{6.4}$$

The wheel slip angles are expressions in equations (5.33) to (5.36). The derivatives are as follows

$$\begin{aligned}
\frac{\partial \alpha_{FL}}{\partial u} &= \frac{\partial}{\partial u}\left(\delta - \arctan\left(\frac{v + \dot{\psi} r_{FL}\cos(\vartheta_{FL})}{u - \dot{\psi} r_{FL}\sin(\vartheta_{FL})}\right)\right) \\
&= \frac{\dfrac{\partial(u - \dot{\psi} r_{FL}\sin(\vartheta_{FL}))}{\partial u}(v + \dot{\psi} r_{FL}\cos(\vartheta_{FL})) - \dfrac{\partial(v + \dot{\psi} r_{FL}\cos(\vartheta_{FL}))}{\partial u}(u - \dot{\psi} r_{FL}\sin(\vartheta_{FL}))}{u^2 + v^2 + 2\dot{\psi} r_{FL}(v\cos(\vartheta_{FL}) - u\sin(\vartheta_{FL})) + \dot{\psi}^2 r^2_{FL}} \\
&= \frac{v + \dot{\psi} r_{FL}\cos(\vartheta_{FL})}{u^2 + v^2 + 2\dot{\psi} r_{FL}(v\cos(\vartheta_{FL}) - u\sin(\vartheta_{FL})) + \dot{\psi}^2 r^2_{FL}}
\end{aligned} \tag{6.5}$$

$$\frac{\partial \alpha_{FL}}{\partial v} = \frac{-u + \dot{\psi} r_{FL}\sin(\vartheta_{FL})}{u^2 + v^2 + 2\dot{\psi} r_{FL}(v\cos(\vartheta_{FL}) - u\sin(\vartheta_{FL})) + \dot{\psi}^2 r^2_{FL}} \tag{6.6}$$

$$\frac{\partial \alpha_{FL}}{\partial \dot{\psi}} = \frac{-r_{FL}(u\cos(\vartheta_{FL}) + v\sin(\vartheta_{FL}))}{u^2 + v^2 + 2\dot{\psi} r_{FL}(v\cos(\vartheta_{FL}) - u\sin(\vartheta_{FL})) + \dot{\psi}^2 r^2_{FL}} \tag{6.7}$$

$$\frac{\partial \alpha_{FL}}{\partial \delta} = 1 \qquad \frac{\partial \alpha_{FL}}{\partial X_R} = 0 \tag{6.8}$$

$$\begin{aligned}
\frac{\partial \alpha_{FR}}{\partial u} &= \frac{\partial}{\partial u}\left(\delta - \arctan\left(\frac{v + \dot{\psi} r_{FR}\sin(\vartheta_{FR})}{u + \dot{\psi} r_{FR}\cos(\vartheta_{FR})}\right)\right) \\
&= \frac{\dfrac{\partial(u + \dot{\psi} r_{FR}\cos(\vartheta_{FR}))}{\partial u}(v + \dot{\psi} r_{FR}\sin(\vartheta_{FR})) - \dfrac{\partial(v + \dot{\psi} r_{FR}\sin(\vartheta_{FR}))}{\partial u}(u + \dot{\psi} r_{FR}\cos(\vartheta_{FR}))}{u^2 + v^2 + 2\dot{\psi} r_{FR}(u\cos(\vartheta_{FR}) + v\sin(\vartheta_{FR})) + \dot{\psi}^2 r_{FR}^2} \\
&= \frac{v + \dot{\psi} r_{FR}\sin(\vartheta_{FR})}{u^2 + v^2 + 2\dot{\psi} r_{FR}(u\cos(\vartheta_{FR}) + v\sin(\vartheta_{FR})) + \dot{\psi}^2 r_{FR}^2}
\end{aligned} \tag{6.9}$$

$$\frac{\partial \alpha_{FR}}{\partial v} = \frac{-u - \dot{\psi} r_{FR}\cos(\vartheta_{FR})}{u^2 + v^2 + 2\dot{\psi} r_{FR}(u\cos(\vartheta_{FR}) + v\sin(\vartheta_{FR})) + \dot{\psi}^2 r_{FR}^2} \tag{6.10}$$

$$\frac{\partial \alpha_{FR}}{\partial \dot{\psi}} = \frac{r_{FR}(v\cos(\vartheta_{FR}) - u\sin(\vartheta_{FR}))}{u^2 + v^2 + 2\dot{\psi} r_{FR}(u\cos(\vartheta_{FR}) + v\sin(\vartheta_{FR})) + \dot{\psi}^2 r_{FR}^2} \tag{6.11}$$

$$\frac{\partial \alpha_{FR}}{\partial \delta} = 1 \qquad\qquad \frac{\partial \alpha_{FR}}{\partial X_R} = 0 \tag{6.12}$$

$$\begin{aligned}
\frac{\partial \alpha_{RL}}{\partial u} &= \frac{\partial}{\partial u}\left(- \arctan\left(\frac{v - \dot{\psi} r_{RL}\sin(\vartheta_{RL})}{u - \dot{\psi} r_{RL}\cos(\vartheta_{RL})}\right)\right) \\
&= \frac{\dfrac{\partial(u - \dot{\psi} r_{RL}\cos(\vartheta_{RL}))}{\partial u}(v - \dot{\psi} r_{RL}\sin(\vartheta_{RL})) - \dfrac{\partial(v - \dot{\psi} r_{RL}\sin(\vartheta_{RL}))}{\partial u}(u - \dot{\psi} r_{RL}\cos(\vartheta_{RL}))}{u^2 + v^2 - 2\dot{\psi} r_{RL}(u\cos(\vartheta_{RL}) + v\sin(\vartheta_{RL})) + \dot{\psi}^2 r_{RL}^2} \\
&= \frac{v - \dot{\psi} r_{RL}\sin(\vartheta_{RL})}{u^2 + v^2 - 2\dot{\psi} r_{RL}(u\cos(\vartheta_{RL}) + v\sin(\vartheta_{RL})) + \dot{\psi}^2 r_{RL}^2}
\end{aligned} \tag{6.13}$$

$$\frac{\partial \alpha_{RL}}{\partial v} = \frac{-u + \dot{\psi} r_{RL}\cos(\vartheta_{RL})}{u^2 + v^2 - 2\dot{\psi} r_{RL}(u\cos(\vartheta_{RL}) + v\sin(\vartheta_{RL})) + \dot{\psi}^2 r_{RL}^2} \tag{6.14}$$

$$\frac{\partial \alpha_{RL}}{\partial \dot{\psi}} = \frac{r_{RL}(u\sin(\vartheta_{RL}) - v\cos(\vartheta_{RL}))}{u^2 + v^2 - 2\dot{\psi} r_{RL}(u\cos(\vartheta_{RL}) + v\sin(\vartheta_{RL})) + \dot{\psi}^2 r_{RL}^2} \tag{6.15}$$

$$\frac{\partial \alpha_{RL}}{\partial \delta} = 0 \qquad\qquad \frac{\partial \alpha_{RL}}{\partial X_R} = 0 \tag{6.16}$$

$$
\begin{aligned}
\frac{\partial \alpha_{RR}}{\partial u} &= \frac{\partial}{\partial u}\left(-\arctan\left(\frac{v-\dot{\psi}r_{RR}\cos(\vartheta_{RR})}{u+\dot{\psi}r_{RR}\sin(\vartheta_{RR})}\right)\right)\\
&= \frac{\dfrac{\partial(u+\dot{\psi}r_{RR}\sin(\vartheta_{RR}))}{\partial u}(v-\dot{\psi}r_{RR}\cos(\vartheta_{RR}))-\dfrac{\partial(v-\dot{\psi}r_{RR}\cos(\vartheta_{RR}))}{\partial u}(u+\dot{\psi}r_{RR}\sin(\vartheta_{RR}))}{u^2+v^2+2\dot{\psi}r_{RR}(u\sin(\vartheta_{RR})-v\cos(\vartheta_{RR}))+\dot{\psi}^2r_{RR}^2}\\
&= \frac{v-\dot{\psi}r_{RR}\cos(\vartheta_{RR})}{u^2+v^2+2\dot{\psi}r_{RR}(u\sin(\vartheta_{RR})-v\cos(\vartheta_{RR}))+\dot{\psi}^2r_{RR}^2}
\end{aligned} \tag{6.17}
$$

$$
\frac{\partial \alpha_{RR}}{\partial v} = \frac{-u-\dot{\psi}r_{RR}\sin(\vartheta_{RR})}{u^2+v^2+2\dot{\psi}r_{RR}(u\sin(\vartheta_{RR})-v\cos(\vartheta_{RR}))+\dot{\psi}^2r_{RR}^2} \tag{6.18}
$$

$$
\frac{\partial \alpha_{RR}}{\partial \dot{\psi}} = \frac{r_{RR}(u\cos(\vartheta_{RR})+v\sin(\vartheta_{RR}))}{u^2+v^2+2\dot{\psi}r_{RR}(u\sin(\vartheta_{RR})-v\cos(\vartheta_{RR}))+\dot{\psi}^2r_{RR}^2} \tag{6.19}
$$

$$
\frac{\partial \alpha_{RR}}{\partial \delta} = 0 \qquad\qquad \frac{\partial \alpha_{RR}}{\partial X_R} = 0 \tag{6.20}
$$

Let $(\cdot)$ be FL or FR, $(\cdots)$ can be u, v or $\dot{\psi}$ and $(-)$ can be FL, FR, RL or RR, the derivatives of the wheel forces can be written as

$$
\frac{\partial X_{(\cdot)}^{(\cdot)}}{\partial(\cdots)} = Z_{(\cdot)}^{b}\left(\frac{\partial \mu_{(\cdot)}^{long}}{\partial(\cdots)}\cos(\alpha_{(\cdot)})+\frac{\partial \mu_{(\cdot)}^{lat}}{\partial(\cdots)}\sin(\alpha_{(\cdot)})+(\mu_{(\cdot)}^{lat}\cos(\alpha_{(\cdot)})-\mu_{(\cdot)}^{long}\sin(\alpha_{(\cdot)}))\frac{\partial \alpha_{(\cdot)}}{\partial(\cdots)}\right) \tag{6.21}
$$

$$
\frac{\partial X_{(\cdot)}^{(\cdot)}}{\partial \delta} = Z_{(\cdot)}^{b}\left(\frac{\partial \mu_{(\cdot)}^{long}}{\partial \delta}\cos(\alpha_{(\cdot)})+\frac{\partial \mu_{(\cdot)}^{lat}}{\partial \delta}\sin(\alpha_{(\cdot)})+(\mu_{(\cdot)}^{lat}\cos(\alpha_{(\cdot)})-\mu_{(\cdot)}^{long}\sin(\alpha_{(\cdot)}))\right) \tag{6.22}
$$

$$
\frac{\partial X_{(\cdot)}^{(\cdot)}}{\partial X_R} = Z_{(\cdot)}^{b}\left(\frac{\partial \mu_{(\cdot)}^{long}}{\partial X_R}\cos(\alpha_{(\cdot)})+\frac{\partial \mu_{(\cdot)}^{lat}}{\partial X_R}\sin(\alpha_{(\cdot)})\right) \tag{6.23}
$$

$$
\frac{\partial Y_{(-)}^{(-)}}{\partial(\cdots)} = Z_{(-)}^{b}\left(\frac{\partial \mu_{(-)}^{lat}}{\partial(\cdots)}\cos(\alpha_{(-)})-\frac{\partial \mu_{(-)}^{long}}{\partial(\cdots)}\sin(\alpha_{(-)})-(\mu_{(-)}^{long}\cos(\alpha_{(-)})+\mu_{(-)}^{lat}\sin(\alpha_{(-)}))\frac{\partial \alpha_{(-)}}{\partial(\cdots)}\right) \tag{6.24}
$$

$$
\frac{\partial Y_{(\cdot)}^{(\cdot)}}{\partial \delta} = Z_{(\cdot)}^{b}\left(\frac{\partial \mu_{(\cdot)}^{lat}}{\partial \delta}\cos(\alpha_{(\cdot)})-\frac{\partial \mu_{(\cdot)}^{long}}{\partial \delta}\sin(\alpha_{(\cdot)})-(\mu_{(\cdot)}^{long}\cos(\alpha_{(\cdot)})+\mu_{(\cdot)}^{lat}\sin(\alpha_{(\cdot)}))\right) \tag{6.25}
$$

$$
\frac{\partial Y_{RL}^{RL}}{\partial \delta} = Z_{RL}^{b}\left(\frac{\partial \mu_{RL}^{lat}}{\partial \delta}\cos(\alpha_{RL})-\frac{\partial \mu_{RL}^{long}}{\partial \delta}\sin(\alpha_{RL})\right) \tag{6.26}
$$

$$
\frac{\partial Y_{RR}^{RR}}{\partial \delta} = Z_{RR}^{b}\left(\frac{\partial \mu_{RR}^{lat}}{\partial \delta}\cos(\alpha_{RR})-\frac{\partial \mu_{RR}^{long}}{\partial \delta}\sin(\alpha_{RR})\right) \tag{6.27}
$$

$$
\frac{\partial Y_{(-)}^{(-)}}{\partial X_R} = Z_{(-)}^{b}\left(\frac{\partial \mu_{(-)}^{lat}}{\partial X_R}\cos(\alpha_{(-)})-\frac{\partial \mu_{(-)}^{long}}{\partial X_R}\sin(\alpha_{(-)})\right) \tag{6.28}
$$

The derivatives of the friction coefficients were found by the approximation

$$\frac{\partial \mu^{long}_{(\cdot)}}{\partial state} = \frac{\mu^{long}_{(\cdot)}(x_0+\epsilon) - \mu^{long}_{(\cdot)}(x_0)}{\epsilon} \tag{6.29}$$

$$\frac{\partial \mu^{lat}_{(\cdot)}}{\partial state} = \frac{\mu^{lat}_{(\cdot)}(x_0+\epsilon) - \mu^{lat}_{(\cdot)}(x_0)}{\epsilon} \tag{6.30}$$

where x_0 is the linearisation point, the parameter $state$ can be u, v, $\dot{\psi}$, δ or X^R_R, and ϵ is a small variation in $state$.

If $(\cdots)$ can be u, v or $\dot{\psi}$ as above, the derivative of the wheel forces in state equations (5.26), (5.27) and (5.31) becomes

$$\begin{aligned}
\frac{\partial \dot{u}}{\partial(\cdots)}_{fw} &= \frac{1}{m}\Big\{(Z^b_{FL}\left(\frac{\partial \mu^{long}_{FL}}{\partial(\cdots)}\cos(\alpha_{FL}) + \frac{\partial \mu^{lat}_{FL}}{\partial(\cdots)}\sin(\alpha_{FL}) + (\mu^{lat}_{FL}\cos(\alpha_{FL}) - \mu^{long}_{FL}\sin(\alpha_{FL}))\frac{\partial \alpha_{FL}}{\partial(\cdots)}\right)\\
&+ Z^b_{FR}\left(\frac{\partial \mu^{long}_{FR}}{\partial(\cdots)}\cos(\alpha_{FR}) + \frac{\partial \mu^{lat}_{FR}}{\partial(\cdots)}\sin(\alpha_{FR}) + (\mu^{lat}_{FR}\cos(\alpha_{FR}) - \mu^{long}_{FR}\sin(\alpha_{FR}))\frac{\partial \alpha_{FR}}{\partial(\cdots)}\right))\cos(\delta)\\
&- (Z^b_{FL}\left(\frac{\partial \mu^{lat}_{FL}}{\partial(\cdots)}\cos(\alpha_{FL}) - \frac{\partial \mu^{long}_{FL}}{\partial(\cdots)}\sin(\alpha_{FL}) - (\mu^{long}_{FL}\cos(\alpha_{FL}) + \mu^{lat}_{FL}\sin(\alpha_{FL}))\frac{\partial \alpha_{FL}}{\partial(\cdots)}\right)\\
&+ Z^b_{FR}\left(\frac{\partial \mu^{lat}_{FR}}{\partial(\cdots)}\cos(\alpha_{FR}) - \frac{\partial \mu^{long}_{FR}}{\partial(\cdots)}\sin(\alpha_{FR}) - (\mu^{long}_{FR}\cos(\alpha_{FR}) + \mu^{lat}_{FR}\sin(\alpha_{FR}))\frac{\partial \alpha_{FR}}{\partial(\cdots)}\right))\sin(\delta)\Big\}
\end{aligned} \tag{6.31}$$

$$\begin{aligned}
\frac{\partial \dot{v}}{\partial(\cdots)}_{fw} &= \frac{1}{m}\Big\{(Z^b_{FL}\left(\frac{\partial \mu^{long}_{FL}}{\partial(\cdots)}\cos(\alpha_{FL}) + \frac{\partial \mu^{lat}_{FL}}{\partial(\cdots)}\sin(\alpha_{FL}) + (\mu^{lat}_{FL}\cos(\alpha_{FL}) - \mu^{long}_{FL}\sin(\alpha_{FL}))\frac{\partial \alpha_{FL}}{\partial(\cdots)}\right)\\
&+ Z^b_{FR}\left(\frac{\partial \mu^{long}_{FR}}{\partial(\cdots)}\cos(\alpha_{FR}) + \frac{\partial \mu^{lat}_{FR}}{\partial(\cdots)}\sin(\alpha_{FR}) + (\mu^{lat}_{FR}\cos(\alpha_{FR}) - \mu^{long}_{FR}\sin(\alpha_{FR}))\frac{\partial \alpha_{FR}}{\partial(\cdots)}\right))\sin(\delta)\\
&+ (Z^b_{FL}\left(\frac{\partial \mu^{lat}_{FL}}{\partial(\cdots)}\cos(\alpha_{FL}) - \frac{\partial \mu^{long}_{FL}}{\partial(\cdots)}\sin(\alpha_{FL}) - (\mu^{long}_{FL}\cos(\alpha_{FL}) + \mu^{lat}_{FL}\sin(\alpha_{FL}))\frac{\partial \alpha_{FL}}{\partial(\cdots)}\right)\\
&+ Z^b_{FR}\left(\frac{\partial \mu^{lat}_{FR}}{\partial(\cdots)}\cos(\alpha_{FR}) - \frac{\partial \mu^{long}_{FR}}{\partial(\cdots)}\sin(\alpha_{FR}) - (\mu^{long}_{FR}\cos(\alpha_{FR}) + \mu^{lat}_{FR}\sin(\alpha_{FR}))\frac{\partial \alpha_{FR}}{\partial(\cdots)}\right))\cos(\delta)\\
&+ (Z^b_{RL}\left(\frac{\partial \mu^{lat}_{RL}}{\partial(\cdots)}\cos(\alpha_{RL}) - \frac{\partial \mu^{long}_{RL}}{\partial(\cdots)}\sin(\alpha_{RL}) - (\mu^{long}_{RL}\cos(\alpha_{RL}) + \mu^{lat}_{RL}\sin(\alpha_{RL}))\frac{\partial \alpha_{RL}}{\partial(\cdots)}\right)\\
&+ Z^b_{RR}\left(\frac{\partial \mu^{lat}_{RR}}{\partial(\cdots)}\cos(\alpha_{RR}) - \frac{\partial \mu^{long}_{RR}}{\partial(\cdots)}\sin(\alpha_{RR}) - (\mu^{long}_{RR}\cos(\alpha_{RR}) + \mu^{lat}_{RR}\sin(\alpha_{RR}))\frac{\partial \alpha_{RR}}{\partial(\cdots)}\right))\Big\}
\end{aligned} \tag{6.32}$$

$$
\begin{aligned}
\frac{\partial \ddot{\psi}}{\partial(\cdots)}_{fw} &= \frac{1}{I_{zz}}\Big\{ l_f (Z^b_{FL} \bigg(\frac{\partial \mu^{lat}_{FL}}{\partial(\cdots)} \cos(\alpha_{FL}) - \frac{\partial \mu^{long}_{FL}}{\partial(\cdots)} \sin(\alpha_{FL}) - (\mu^{long}_{FL} \cos(\alpha_{FL}) + \mu^{lat}_{FL} \sin(\alpha_{FL})) \frac{\partial \alpha_{FL}}{\partial(\cdots)} \bigg) \\
&+ Z^b_{FR} \bigg(\frac{\partial \mu^{lat}_{FR}}{\partial(\cdots)} \cos(\alpha_{FR}) - \frac{\partial \mu^{long}_{FR}}{\partial(\cdots)} \sin(\alpha_{FR}) - (\mu^{long}_{FR} \cos(\alpha_{FR}) + \mu^{lat}_{FR} \sin(\alpha_{FR})) \frac{\partial \alpha_{FR}}{\partial(\cdots)} \bigg)) \cos(\delta) \\
&+ l_f (Z^b_{FL} \bigg(\frac{\partial \mu^{long}_{FL}}{\partial(\cdots)} \cos(\alpha_{FL}) + \frac{\partial \mu^{lat}_{FL}}{\partial(\cdots)} \sin(\alpha_{FL}) + (\mu^{lat}_{FL} \cos(\alpha_{FL}) - \mu^{long}_{FL} \sin(\alpha_{FL})) \frac{\partial \alpha_{FL}}{\partial(\cdots)} \bigg) \\
&+ Z^b_{FR} \bigg(\frac{\partial \mu^{long}_{FR}}{\partial(\cdots)} \cos(\alpha_{FR}) + \frac{\partial \mu^{lat}_{FR}}{\partial(\cdots)} \sin(\alpha_{FR}) + (\mu^{lat}_{FR} \cos(\alpha_{FR}) - \mu^{long}_{FR} \sin(\alpha_{FR})) \frac{\partial \alpha_{FR}}{\partial(\cdots)} \bigg)) \sin(\delta) \\
&+ \frac{b}{2} (Z^b_{FR} \bigg(\frac{\partial \mu^{long}_{FR}}{\partial(\cdots)} \cos(\alpha_{FR}) + \frac{\partial \mu^{lat}_{FR}}{\partial(\cdots)} \sin(\alpha_{FR}) + (\mu^{lat}_{FR} \cos(\alpha_{FR}) - \mu^{long}_{FR} \sin(\alpha_{FR})) \frac{\partial \alpha_{FR}}{\partial(\cdots)} \bigg) \\
&- Z^b_{FL} \bigg(\frac{\partial \mu^{long}_{FL}}{\partial(\cdots)} \cos(\alpha_{FL}) + \frac{\partial \mu^{lat}_{FL}}{\partial(\cdots)} \sin(\alpha_{FL}) + (\mu^{lat}_{FL} \cos(\alpha_{FL}) - \mu^{long}_{FL} \sin(\alpha_{FL})) \frac{\partial \alpha_{FL}}{\partial(\cdots)} \bigg) \cos(\delta) \\
&- \frac{b}{2} (Z^b_{FR} \bigg(\frac{\partial \mu^{lat}_{FR}}{\partial(\cdots)} \cos(\alpha_{FR}) - \frac{\partial \mu^{long}_{FR}}{\partial(\cdots)} \sin(\alpha_{FR}) - (\mu^{long}_{FR} \cos(\alpha_{FR}) + \mu^{lat}_{FR} \sin(\alpha_{FR})) \frac{\partial \alpha_{FR}}{\partial(\cdots)} \bigg) \\
&- Z^b_{FL} \bigg(\frac{\partial \mu^{lat}_{FL}}{\partial(\cdots)} \cos(\alpha_{FL}) - \frac{\partial \mu^{long}_{FL}}{\partial(\cdots)} \sin(\alpha_{FL}) - (\mu^{long}_{FL} \cos(\alpha_{FL}) + \mu^{lat}_{FL} \sin(\alpha_{FL})) \frac{\partial \alpha_{FL}}{\partial(\cdots)} \bigg)) \sin(\delta) \\
&- l_r (Z^b_{RL} \bigg(\frac{\partial \mu^{lat}_{RL}}{\partial(\cdots)} \cos(\alpha_{RL}) - \frac{\partial \mu^{long}_{RL}}{\partial(\cdots)} \sin(\alpha_{RL}) - (\mu^{long}_{RL} \cos(\alpha_{RL}) + \mu^{lat}_{RL} \sin(\alpha_{RL})) \frac{\partial \alpha_{RL}}{\partial(\cdots)} \bigg) \\
&+ Z^b_{RR} \bigg(\frac{\partial \mu^{lat}_{RR}}{\partial(\cdots)} \cos(\alpha_{RR}) - \frac{\partial \mu^{long}_{RR}}{\partial(\cdots)} \sin(\alpha_{RR}) - (\mu^{long}_{RR} \cos(\alpha_{RR}) + \mu^{lat}_{RR} \sin(\alpha_{RR})) \frac{\partial \alpha_{RR}}{\partial(\cdots)} \bigg)) \Big\}
\end{aligned}
\tag{6.33}
$$

where the subscript fw is an abbreviation for "from wheels", because it is the derivative of the forces coming from the wheels.

The resulting derivatives are

$$\frac{\partial\dot{u}}{\partial u} = \frac{\partial\dot{u}}{\partial u}_{fw} - C_r g - \frac{\rho}{m}|u|A_f C_D \tag{6.34}$$

$$\frac{\partial\dot{u}}{\partial v} = \frac{\partial\dot{u}}{\partial v}_{fw} + \dot{\psi} \tag{6.35}$$

$$\frac{\partial\dot{u}}{\partial\dot{\psi}} = \frac{\partial\dot{u}}{\partial\dot{\psi}}_{fw} + v \tag{6.36}$$

$$\begin{aligned}
\frac{\partial\dot{u}}{\partial\delta} = \frac{1}{m}\Big\{ & (Z^b_{FL}\Bigg(\frac{\partial\mu^{long}_{FL}}{\partial\delta}\cos(\alpha_{FL}) + \frac{\partial\mu^{lat}_{FL}}{\partial\delta}\sin(\alpha_{FL}) + (\mu^{lat}_{FL}\cos(\alpha_{FL}) - \mu^{long}_{FL}\sin(\alpha_{FL}))\Bigg) \\
& + Z^b_{FR}\Bigg(\frac{\partial\mu^{long}_{FR}}{\partial\delta}\cos(\alpha_{FR}) + \frac{\partial\mu^{lat}_{FR}}{\partial\delta}\sin(\alpha_{FR}) + (\mu^{lat}_{FR}\cos(\alpha_{FR}) - \mu^{long}_{FR}\sin(\alpha_{FR}))\Bigg))\cos(\delta) \\
& - (Z^b_{FL}\Bigg(\frac{\partial\mu^{lat}_{FL}}{\partial\delta}\cos(\alpha_{FL}) - \frac{\partial\mu^{long}_{FL}}{\partial\delta}\sin(\alpha_{FL}) - (\mu^{long}_{FL}\cos(\alpha_{FL}) + \mu^{lat}_{FL}\sin(\alpha_{FL}))\Bigg) \\
& + Z^b_{FR}\Bigg(\frac{\partial\mu^{lat}_{FR}}{\partial\delta}\cos(\alpha_{FR}) - \frac{\partial\mu^{long}_{FR}}{\partial\delta}\sin(\alpha_{FR}) - (\mu^{long}_{FR}\cos(\alpha_{FR}) + \mu^{lat}_{FR}\sin(\alpha_{FR}))\Bigg))\sin(\delta)\Big\}
\end{aligned} \tag{6.37}$$

$$\begin{aligned}
\frac{\partial\dot{u}}{\partial X_R} = \frac{1}{m} + \frac{1}{m}\Big\{ & (Z^b_{FL}\Bigg(\frac{\partial\mu^{long}_{FL}}{\partial X_R}\cos(\alpha_{FL}) + \frac{\partial\mu^{lat}_{FL}}{\partial X_R}\sin(\alpha_{FL})\Bigg) \\
& + Z^b_{FR}\Bigg(\frac{\partial\mu^{long}_{FR}}{\partial X_R}\cos(\alpha_{FR}) + \frac{\partial\mu^{lat}_{FR}}{\partial X_R}\sin(\alpha_{FR})\Bigg))\cos(\delta) \\
& - (Z^b_{FL}\Bigg(\frac{\partial\mu^{lat}_{FL}}{\partial X_R}\cos(\alpha_{FL}) - \frac{\partial\mu^{long}_{FL}}{\partial X_R}\sin(\alpha_{FL})\Bigg) \\
& + Z^b_{FR}\Bigg(\frac{\partial\mu^{lat}_{FR}}{\partial X_R}\cos(\alpha_{FR}) - \frac{\partial\mu^{long}_{FR}}{\partial X_R}\sin(\alpha_{FR})\Bigg))\sin(\delta)\Big\}
\end{aligned} \tag{6.38}$$

$$\frac{\partial \dot{v}}{\partial u} = \frac{\partial \dot{v}}{\partial u}_{fw} - \dot{\psi} \tag{6.39}$$

$$\frac{\partial \dot{v}}{\partial v} = \frac{\partial \dot{v}}{\partial v}_{fw} - \frac{\rho}{m}|v|A_s C_D \tag{6.40}$$

$$\frac{\partial \dot{v}}{\partial \dot{\psi}} = \frac{\partial \dot{v}}{\partial \dot{\psi}}_{fw} - u \tag{6.41}$$

$$\begin{aligned}
\frac{\partial \dot{v}}{\partial \delta} = \frac{1}{m}\Big\{ & (Z^b_{FL}\left(\frac{\partial \mu^{long}_{FL}}{\partial \delta}\cos(\alpha_{FL}) + \frac{\partial \mu^{lat}_{FL}}{\partial \delta}\sin(\alpha_{FL}) + (\mu^{lat}_{FL}\cos(\alpha_{FL}) - \mu^{long}_{FL}\sin(\alpha_{FL}))\right) \\
& + Z^b_{FR}\left(\frac{\partial \mu^{long}_{FR}}{\partial \delta}\cos(\alpha_{FR}) + \frac{\partial \mu^{lat}_{FR}}{\partial \delta}\sin(\alpha_{FR}) + (\mu^{lat}_{FR}\cos(\alpha_{FR}) - \mu^{long}_{FR}\sin(\alpha_{FR}))\right))\sin(\delta) \\
& + (Z^b_{FL}\left(\frac{\partial \mu^{lat}_{FL}}{\partial \delta}\cos(\alpha_{FL}) - \frac{\partial \mu^{long}_{FL}}{\partial \delta}\sin(\alpha_{FL}) - (\mu^{long}_{FL}\cos(\alpha_{FL}) + \mu^{lat}_{FL}\sin(\alpha_{FL}))\right) \\
& + Z^b_{FR}\left(\frac{\partial \mu^{lat}_{FR}}{\partial \delta}\cos(\alpha_{FR}) - \frac{\partial \mu^{long}_{FR}}{\partial \delta}\sin(\alpha_{FR}) - (\mu^{long}_{FR}\cos(\alpha_{FR}) + \mu^{lat}_{FR}\sin(\alpha_{FR}))\right))\cos(\delta) \\
& + Z^b_{RL}\left(\frac{\partial \mu^{lat}_{RL}}{\partial \delta}\cos(\alpha_{RL}) - \frac{\partial \mu^{long}_{RL}}{\partial \delta}\sin(\alpha_{RL})\right) \\
& + Z^b_{RR}\left(\frac{\partial \mu^{lat}_{RR}}{\partial \delta}\cos(\alpha_{RR}) - \frac{\partial \mu^{long}_{RR}}{\partial \delta}\sin(\alpha_{RR})\right)\Big\}
\end{aligned} \tag{6.42}$$

$$\begin{aligned}
\frac{\partial \dot{v}}{\partial X_R} = \frac{1}{m}\Big\{ & (Z^b_{FL}\left(\frac{\partial \mu^{long}_{FL}}{\partial X_R}\cos(\alpha_{FL}) + \frac{\partial \mu^{lat}_{FL}}{\partial X_R}\sin(\alpha_{FL})\right) \\
& + Z^b_{FR}\left(\frac{\partial \mu^{long}_{FR}}{\partial X_R}\cos(\alpha_{FR}) + \frac{\partial \mu^{lat}_{FR}}{\partial X_R}\sin(\alpha_{FR})\right))\sin(\delta) \\
& + (Z^b_{FL}\left(\frac{\partial \mu^{lat}_{FL}}{\partial X_R}\cos(\alpha_{FL}) - \frac{\partial \mu^{long}_{FL}}{\partial X_R}\sin(\alpha_{FL})\right) \\
& + Z^b_{FR}\left(\frac{\partial \mu^{lat}_{FR}}{\partial X_R}\cos(\alpha_{FR}) - \frac{\partial \mu^{long}_{FR}}{\partial X_R}\sin(\alpha_{FR})\right))\cos(\delta) \\
& + Z^b_{RL}\left(\frac{\partial \mu^{lat}_{RL}}{\partial X_R}\cos(\alpha_{RL}) - \frac{\partial \mu^{long}_{RL}}{\partial X_R}\sin(\alpha_{RL})\right) \\
& + Z^b_{RR}\left(\frac{\partial \mu^{lat}_{RR}}{\partial X_R}\cos(\alpha_{RR}) - \frac{\partial \mu^{long}_{RR}}{\partial X_R}\sin(\alpha_{RR})\right)\Big\}
\end{aligned} \tag{6.43}$$

$$\frac{\partial\ddot{\psi}}{\partial u} = \frac{\partial\ddot{\psi}}{\partial u}_{fw} \tag{6.44}$$

$$\frac{\partial\ddot{\psi}}{\partial v} = \frac{\partial\ddot{\psi}}{\partial v}_{fw} \tag{6.45}$$

$$\frac{\partial\ddot{\psi}}{\partial\dot{\psi}} = \frac{\partial\ddot{\psi}}{\partial\dot{\psi}}_{fw} \tag{6.46}$$

$$\begin{aligned}
\frac{\partial\ddot{\psi}}{\partial\delta} = \frac{1}{I_{zz}}\Big\{& l_f(Z^b_{FL}\Bigg(\frac{\partial\mu^{lat}_{FL}}{\partial\delta}\cos(\alpha_{FL}) - \frac{\partial\mu^{long}_{FL}}{\partial\delta}\sin(\alpha_{FL}) - (\mu^{long}_{FL}\cos(\alpha_{FL}) + \mu^{lat}_{FL}\sin(\alpha_{FL}))\Bigg)\\
&+ Z^b_{FR}\Bigg(\frac{\partial\mu^{lat}_{FR}}{\partial\delta}\cos(\alpha_{FR}) - \frac{\partial\mu^{long}_{FR}}{\partial\delta}\sin(\alpha_{FR}) - (\mu^{long}_{FR}\cos(\alpha_{FR}) + \mu^{lat}_{FR}\sin(\alpha_{FR}))\Bigg)\cos(\delta)\\
&+ l_f(Z^b_{FL}\Bigg(\frac{\partial\mu^{long}_{FL}}{\partial\delta}\cos(\alpha_{FL}) + \frac{\partial\mu^{lat}_{FL}}{\partial\delta}\sin(\alpha_{FL})) + (\mu^{lat}_{FL}\cos(\alpha_{FL}) - \mu^{long}_{FL}\sin(\alpha_{FL}))\Bigg)\\
&+ Z^b_{FR}\Bigg(\frac{\partial\mu^{long}_{FR}}{\partial\delta}\cos(\alpha_{FR}) + \frac{\partial\mu^{lat}_{FR}}{\partial\delta}\sin(\alpha_{FR})) + (\mu^{lat}_{FR}\cos(\alpha_{FR}) - \mu^{long}_{FR}\sin(\alpha_{FR}))\Bigg))\sin(\delta)\\
&+ \frac{b}{2}(Z^b_{FR}\Bigg(\frac{\partial\mu^{long}_{FR}}{\partial\delta}\cos(\alpha_{FR}) + \frac{\partial\mu^{lat}_{FR}}{\partial\delta}\sin(\alpha_{FR}) + (\mu^{lat}_{FR}\cos(\alpha_{FR}) - \mu^{long}_{FR}\sin(\alpha_{FR}))\Bigg)\\
&- Z^b_{FL}\Bigg(\frac{\partial\mu^{long}_{FL}}{\partial\delta}\cos(\alpha_{FL}) + \frac{\partial\mu^{lat}_{FL}}{\partial\delta}\sin(\alpha_{FL}) + (\mu^{lat}_{FL}\cos(\alpha_{FL}) - \mu^{long}_{FL}\sin(\alpha_{FL}))\Bigg))\cos(\delta)\\
&- \frac{b}{2}(Z^b_{FR}\Bigg(\frac{\partial\mu^{lat}_{FR}}{\partial\delta}\cos(\alpha_{FR}) - \frac{\partial\mu^{long}_{FR}}{\partial\delta}\sin(\alpha_{FR}) - (\mu^{long}_{FR}\cos(\alpha_{FR}) + \mu^{lat}_{FR}\sin(\alpha_{FR}))\Bigg)\\
&- Z^b_{FL}\Bigg(\frac{\partial\mu^{lat}_{FL}}{\partial\delta}\cos(\alpha_{FL}) - \frac{\partial\mu^{long}_{FL}}{\partial\delta}\sin(\alpha_{FL}) - (\mu^{long}_{FL}\cos(\alpha_{FL}) + \mu^{lat}_{FL}\sin(\alpha_{FL}))\Bigg))\sin(\delta)\\
&- l_r(Z^b_{RL}\Bigg(\frac{\partial\mu^{lat}_{RL}}{\partial\delta}\cos(\alpha_{RL}) - \frac{\partial\mu^{long}_{RL}}{\partial\delta}\sin(\alpha_{RL})\Bigg)\\
&- Z^b_{RR}\Bigg(\frac{\partial\mu^{lat}_{RR}}{\partial\delta}\cos(\alpha_{RR}) - \frac{\partial\mu^{long}_{RR}}{\partial\delta}\sin(\alpha_{RR})\Bigg))\Big\}
\end{aligned} \tag{6.47}$$

$$
\begin{aligned}
\frac{\partial \ddot{\psi}}{\partial X_R} = \frac{1}{I_{zz}} \Big\{ & l_f(Z_{FL}^b \left(\frac{\partial \mu_{FL}^{lat}}{\partial X_R} \cos(\alpha_{FL}) - \frac{\partial \mu_{FL}^{long}}{\partial X_R} \sin(\alpha_{FL}) \right) \\
& + Z_{FR}^b \left(\frac{\partial \mu_{FR}^{lat}}{\partial X_R} \cos(\alpha_{FR}) - \frac{\partial \mu_{FR}^{long}}{\partial X_R} \sin(\alpha_{FR}) \right)) \cos(\delta) \\
& + l_f(Z_{FL}^b \left(\frac{\partial \mu_{FL}^{long}}{\partial X_R} \cos(\alpha_{FL}) + \frac{\partial \mu_{FL}^{lat}}{\partial X_R} \sin(\alpha_{FL}) \right) \\
& + Z_{FR}^b \left(\frac{\partial \mu_{FR}^{long}}{\partial X_R} \cos(\alpha_{FR}) + \frac{\partial \mu_{FR}^{lat}}{\partial X_R} \sin(\alpha_{FR}) \right)) \sin(\delta) \\
& + \frac{b}{2}(Z_{FR}^b \left(\frac{\partial \mu_{FR}^{long}}{\partial X_R} \cos(\alpha_{FR}) + \frac{\partial \mu_{FR}^{lat}}{\partial X_R} \sin(\alpha_{FR}) \right) \\
& - Z_{FL}^b \left(\frac{\partial \mu_{FL}^{long}}{\partial X_R} \cos(\alpha_{FL}) + \frac{\partial \mu_{FL}^{lat}}{\partial X_R} \sin(\alpha_{FL}) \right)) \cos(\delta) \\
& - \frac{b}{2}(Z_{FR}^b \left(\frac{\partial \mu_{FR}^{lat}}{\partial X_R} \cos(\alpha_{FR}) - \frac{\partial \mu_{FR}^{long}}{\partial X_R} \sin(\alpha_{FR}) \right) \\
& - Z_{FL}^b \left(\frac{\partial \mu_{FL}^{lat}}{\partial X_R} \cos(\alpha_{FL}) - \frac{\partial \mu_{FL}^{long}}{\partial X_R} \sin(\alpha_{FL}) \right)) \sin(\delta) \\
& - l_r(Z_{RL}^b \left(\frac{\partial \mu_{RL}^{lat}}{\partial X_R} \cos(\alpha_{RL}) - \frac{\partial \mu_{RL}^{long}}{\partial X_R} \sin(\alpha_{RL}) \right) \\
& + Z_{RR}^b \left(\frac{\partial \mu_{RR}^{lat}}{\partial X_R} \cos(\alpha_{RR}) - \frac{\partial \mu_{RR}^{long}}{\partial X_R} \sin(\alpha_{RR}) \right))
\end{aligned}
\tag{6.48}
$$

The resulting linearised system is on the form

$$
\Delta \dot{\mathbf{x}} = \begin{bmatrix} \frac{\partial \dot{u}}{\partial u} & \frac{\partial \dot{u}}{\partial v} & \frac{\partial \dot{u}}{\partial \dot{\psi}} \\ \frac{\partial \dot{v}}{\partial u} & \frac{\partial \dot{v}}{\partial v} & \frac{\partial \dot{v}}{\partial \dot{\psi}} \\ \frac{\partial \ddot{\psi}}{\partial u} & \frac{\partial \ddot{\psi}}{\partial v} & \frac{\partial \ddot{\psi}}{\partial \dot{\psi}} \end{bmatrix} \Delta \mathbf{x} + \begin{bmatrix} \frac{\partial \dot{u}}{\partial \delta} & \frac{\partial \dot{u}}{\partial X_R} \\ \frac{\partial \dot{v}}{\partial \delta} & \frac{\partial \dot{v}}{\partial X_R} \\ \frac{\partial \ddot{\psi}}{\partial \delta} & \frac{\partial \ddot{\psi}}{\partial X_R} \end{bmatrix} \Delta \mathbf{u} \tag{6.49}
$$

where

$$
\Delta \mathbf{x} = \begin{bmatrix} \Delta u \\ \Delta v \\ \Delta \dot{\psi} \end{bmatrix} = \begin{bmatrix} u - u_0 \\ v - v_0 \\ \dot{\psi} - \dot{\psi}_0 \end{bmatrix} \tag{6.50}
$$

$$
\Delta \mathbf{u} = \begin{bmatrix} \Delta \delta \\ \Delta X_R \end{bmatrix} = \begin{bmatrix} \delta - \delta_0 \\ X_R - X_{R0} \end{bmatrix} \tag{6.51}
$$

where u_0, v_0 and $\dot{\psi}_0$ are state values and δ_0 and X_{R0} are input values at the linearisation point.

6.2 Linearisation Point

The simulator consist of a 6 DOF model that needs to be in a steady state to find the linearisation points. A steady state means that the states are constant, in other words, their derivatives are zero.

Gathering the differential equations for finding the linearisation point from equations (5.57), (5.58), (5.63) and (5.65).

$$\begin{aligned} L_a \frac{di_a}{dt} &= -R_a i_a - k_E \omega_m + u_a && (6.52)\\ I_m \dot{\omega}_m &= k_t i_a - T_L && (6.53)\\ I_w \dot{\omega}_{FL} &= -r_w X_{FL} && (6.54)\\ I_w \dot{\omega}_{FR} &= -r_w X_{FR} && (6.55)\\ \dot{\omega}_R &= \frac{1}{2I_w + I_m}\Big(T_{drive} - r_{wheel} X_R\Big) && (6.56) \end{aligned}$$

and the unknowns are

$$\delta_0,\ \dot{\psi}_0,\ V_{T0},\ \beta_0,\ \omega_{m0},\ \omega_{fl0},\ \omega_{fr0},\ T_{drive0},\ i_{a0},\ u_{a0} \tag{6.57}$$

It would be desirable to use the equations of motion to find the steady state of the system. However, this proved difficult due to the friction coefficient expression in equation (5.43), cannot be solved with respect to $s^{Res}_{(\cdot)}$.

Optimally the speed V_{T0} and sideslip angle β_0 could be chosen, and the other unknowns found through mathematical manipulation. However at first glance, by choosing two of the unknowns, there are still eight left, with only five equations. Thus three of the unknowns need to be found by searching. The search was performed on the equations of motion in equations (5.26) to (5.31), where the acceleration of the system is minimized.

Equation (6.56) was used to find the driving torque T_{drive0}

$$\begin{aligned} 0 &= T_{drive0} - r_w X_{R0}\\ T_{drive0} &= r_w X_{R0} && (6.58) \end{aligned}$$

Equation (6.52), (6.53) and (6.58) give an expression for the steady state armature current i_{a0} and armature voltage u_{a0}. Note that the load torque, T_{L0} is the driving torque T_{drive0}

$$\begin{aligned} 0 &= k_t i_{a0} - T_{drive0}\\ i_{a0} &= \frac{T_{drive0}}{k_t} = \frac{r_w X_{R0}}{k_t} && (6.59)\\ 0 &= -R_a i_{a0} - k_E \omega_{m0} + u_{a0}\\ u_{a0} &= k_E \omega_{m0} + R_a i_{a0} = k_E \omega_{m0} + \frac{r_w X_{R0} R_a}{k_t} && (6.60) \end{aligned}$$

If a swipe is done on ω_m to find the value ω_{m0} with the associated smallest acceleration value, u_{a0} can be found.

Equation (6.54) was used as a starting point for finding the steady state yaw rate $\dot{\psi}_0$. By substituting equation (5.32)

$$\begin{aligned}
X_{FL0} = 0 &= \mu_{FL0}^{long}\cos(\alpha_{FL0})Z_{FL0} + \mu_{FL0}^{lat}\sin(\alpha_{FL0})Z_{FL0} \\
\cos(\alpha_{FL0})\mu_{FL0}^{long} &= -\sin(\alpha_{FL0})\mu_{FL0}^{lat} \\
\cos(\alpha_{FL0})\mu_{FL0}\frac{s_{FL0}^{long}}{s_{FL0}^{Res}} &= -\sin(\alpha_{FL0})\mu_{FL0}\frac{s_{FL0}^{lat}}{s_{FL0}^{Res}} \\
s_{FL0}^{long}\cos(\alpha_{FL0}) &= -\sin(\alpha_{FL0})s_{FL0}^{lat}
\end{aligned} \tag{6.61}$$

where equation (5.41) has been used.

Inserting the expressions for the longitudinal and lateral slip from equations (5.44) and (5.45) gives

$$\begin{aligned}
\frac{V_{R,FL0}\cos(\alpha_{FL0}) - V_{W,FL0}}{V_{W,FL0}}\cos(\alpha_{FL0}) &= -\sin^2(\alpha_{FL0})\frac{V_{R,FL0}}{V_{W,FL0}} \\
V_{R,FL0} &= \cos(\alpha_{FL0})V_{W,FL0}
\end{aligned} \tag{6.62}$$

Now the wheel slip angle α_{FL0} and ground wheel contact point velocity $V_{W,FL0}$ from equations (5.33) and (5.49) respectively, are inserted

$$\begin{aligned}
V_{R,FL0} &= \cos(\delta_0 - \arctan\left(\frac{v_0 + \dot{\psi}_0 r_{FL}\cos(\vartheta_{FL})}{u_0 - \dot{\psi}_0 r_{FL}\sin(\vartheta_{FL})}\right)) \cdot \\
&\sqrt{u_0^2 + v_0^2 + 2\dot{\psi}_0 r_{FL}(v_0\cos(\vartheta_{FL}) - u_0\sin(\vartheta_{FL})) + \dot{\psi}_0^2 r_{FL}^2} \\
V_{R,FL0} &= (\cos(\delta_0)\cos\left(\arctan\left(\frac{v_0 + \dot{\psi}_0 r_{FL}\cos(\vartheta_{FL})}{u_0 - \dot{\psi}_0 r_{FL}\sin(\vartheta_{FL})}\right)\right) \\
&+ \sin(\delta_0)\sin\left(\arctan\left(\frac{v_0 + \dot{\psi}_0 r_{FL}\cos(\vartheta_{FL})}{u_0 - \dot{\psi}_0 r_{FL}\sin(\vartheta_{FL})}\right)\right)) \cdot \\
&\sqrt{u_0^2 + v_0^2 + 2\dot{\psi}_0 r_{FL}(v_0\cos(\vartheta_{FL}) - u_0\sin(\vartheta_{FL})) + \dot{\psi}_0^2 r_{FL}^2} \\
V_{R,FL0} &= (\cos(\delta_0)\frac{u_0 - \dot{\psi}_0 r_{FL}\sin(\vartheta_{FL})}{\sqrt{u_0^2 + v_0^2 + 2\dot{\psi}_0 r_{FL}(v_0\cos(\vartheta_{FL}) - u_0\sin(\vartheta_{FL})) + \dot{\psi}_0^2 r_{FL}^2}} \\
&+ \sin(\delta_0)\frac{v_0 + \dot{\psi}_0 r_{FL}\cos(\vartheta_{FL})}{\sqrt{u_0^2 + v_0^2 + 2\dot{\psi}_0 r_{FL}(v_0\cos(\vartheta_{FL}) - u_0\sin(\vartheta_{FL})) + \dot{\psi}_0^2 r_{FL}^2}}) \cdot \\
&\sqrt{u_0^2 + v_0^2 + 2\dot{\psi}_0 r_{FL}(v_0\cos(\vartheta_{FL}) - u_0\sin(\vartheta_{FL})) + \dot{\psi}_0^2 r_{FL}^2}
\end{aligned}$$

$$\begin{aligned}
V_{R,FL0} &= \cos(\delta_0)(u_0 - \dot{\psi}_0 r_{FL}\sin(\vartheta_{FL})) + \sin(\delta_0)(v_0 + \dot{\psi}_0 r_{FL}\cos(\vartheta_{FL})) \\
u_0\cos(\delta_0) + v_0\sin(\delta_0) - V_{R,FL0} &= \dot{\psi}_0 r_{FL}(\sin(\vartheta_{FL})\cos(\delta_0) - \cos(\vartheta_{FL})\sin(\delta_0)) \\
\dot{\psi}_0 &= \frac{u_0\cos(\delta_0) + v_0\sin(\delta_0) - V_{R,FL0}}{r_{FL}(\sin(\vartheta_{FL})\cos(\delta_0) - \cos(\vartheta_{FL})\sin(\delta_0))} \qquad (6.63)
\end{aligned}$$

where the trigonometric properties in equation (3.5), (3.7) and (3.8) were used. Finally the rotational equivalent velocity $V_{R,FL0}$is inserted from equation (5.48), which yields

$$\dot{\psi}_0 = \frac{u_0\cos(\delta_0) + v_0\sin(\delta_0) - r_w\omega_{FL0}}{r_{FL}(\sin(\vartheta_{FL})\cos(\delta_0) - \cos(\vartheta_{FL})\sin(\delta_0))} \qquad (6.64)$$

The steady state yaw rate $\dot{\psi}_0$ can be found from (6.64) with a swipe in ω_{FL} and δ to find the steady state values ω_{FL0} and δ_0.

A similar derivation can be done with equation (6.55) to find an expression for ω_{FR0}

$$\begin{aligned}
V_{R,FR0} &= \cos(\delta_0)(u_0 + \dot{\psi}_0 r_{FR}\cos(\vartheta_{FR})) + \sin(\delta_0)(v_0 + \dot{\psi}_0 r_{FR}\sin(\vartheta_{FR})) \\
\omega_{FR0} &= \frac{u_0\cos(\delta_0) + v_0\sin(\delta_0) + \dot{\psi}_0 r_{FR}(\cos(\vartheta_{FR})\cos(\delta_0) + \sin(\vartheta_{FR})\sin(\delta_0))}{r_w} \qquad (6.65)
\end{aligned}$$

In summary, by choosing V_{T0} and β_0, calculating T_{drive0}, i_{a0}, u_{a0}, $\dot{\psi}_0$ and ω_{FR0} by doing a swipe on ω_m, ω_{FL} and δ to find ω_{m0}, ω_{FL0} and δ_0, all the unknown steady state values are found.

7 Steady State Analysis

The vehicle has input saturations making some of the drifting equilibria unreachable. Thus an analysis of the steady state drifting equilibria is important, to find the envelope of feasible equilibria. When driving with large sideslip angles, the yaw rate changes according to the specific sideslip angle and speed. By looking at this relationship, the sideslip angle which corresponds to the largest yaw rate can be found for the speed range. Increase in yaw rate makes the turning radius smaller and increases manoeuvrability of the vehicle.

The linearised model developed in section 6.1 was implemented in Matlab. To find the steady state values for the nonlinear two-track model, the method described in section 6.2 was used. An analysis of the mappings between states and inputs, and between the states themselves can be found in section 7.1. In section 7.2 the pole movements of the linearised system is analysed. A discussion of the findings in sections 7.1 and 7.2 can be found in section 7.3.

7.1 Steady State Plots

In this section, drifting equilibria for a left handed turn will be investigated. Drifting in a left handed turn has positive yaw rate and negative sideslip angle. Due to vehicle symmetry, the steady state values for the right handed turn is a mirror image of the steady state values for the left handed turn.

Firstly the equilibrium values for the speed V_{T0} and the sideslip angle β_0, were chosen to be

$$V_{T0} = \{1, 2, 3, 4, 5, 6, 7, 8, 9, 10\} \text{ m/s} \tag{7.1}$$

$$\begin{aligned}\beta_0 = \{&-1^\circ, -2^\circ, -3^\circ, -4^\circ, -5^\circ, -6^\circ, -7^\circ, -8^\circ, -9^\circ, -10^\circ, -11^\circ, -12^\circ, -13^\circ, -14^\circ,\\ &-15^\circ, -16^\circ, -17^\circ, -18^\circ, -19^\circ, -20^\circ, -21^\circ, -22^\circ, -23^\circ, -24^\circ, -25^\circ, -26^\circ,\\ &-27^\circ, -28^\circ, -29^\circ, -30^\circ\}\end{aligned} \tag{7.2}$$

Then T_{drive0}, i_{a0}, u_{a0}, $\dot{\psi}_0$ and ω_{FR0} were found by equations (6.58) to (6.65), by means of a swipe in ω_m, ω_{FL} and δ. The smallest acceleration value from the equations of motion, in equations (5.26) to (5.31), were used as the steady state point.

In figure 7.1, the steady state values of the sideslip angle β_0 are shown as function of the steering angle δ_0. The plot has been made three-dimensional with colour coding of the points, with respect to the speed. Both the feasible and unreachable equilibriums have been included in the plot, where the stars, $*$, are the unreachable points and the circles, $\circ$, are the feasible ones. Input constraints are the reason some of the steady state points are unreachable. This graphing syntax will be used throughout this section.

In figure 7.2, the sideslip angle equilibriums are shown as function the thrust input X_{R0}. Figure 7.3 and 7.4 show the steady state yaw rate $\dot{\psi}_0$ as function of steering angle and thrust input respectively. To include the speed, these graphs have also been colour coded.

From figure 7.1 and 7.2, the steady state values seem to follow patterns, with some outlying exceptions. There is a cluster of feasible steady state values with small speed and sideslip angle, on the top left of figure 7.1 and 7.2. Those equilibrium points correspond to the points in the lower left corner of figure 7.3 and 7.4, with negative yaw rate. When driving without drifting, the sign of the sideslip angle and the yaw rate are equal, such that these equilibria are not drifting equilibria. According to [1], the sideslip angle is normally kept below 2°. However, the maximum sideslip angle for these equilibria is 6° which is three times higher than expected. Because steady state values for drifting are of interest, the equilibria with negative yaw rate will be discarded.

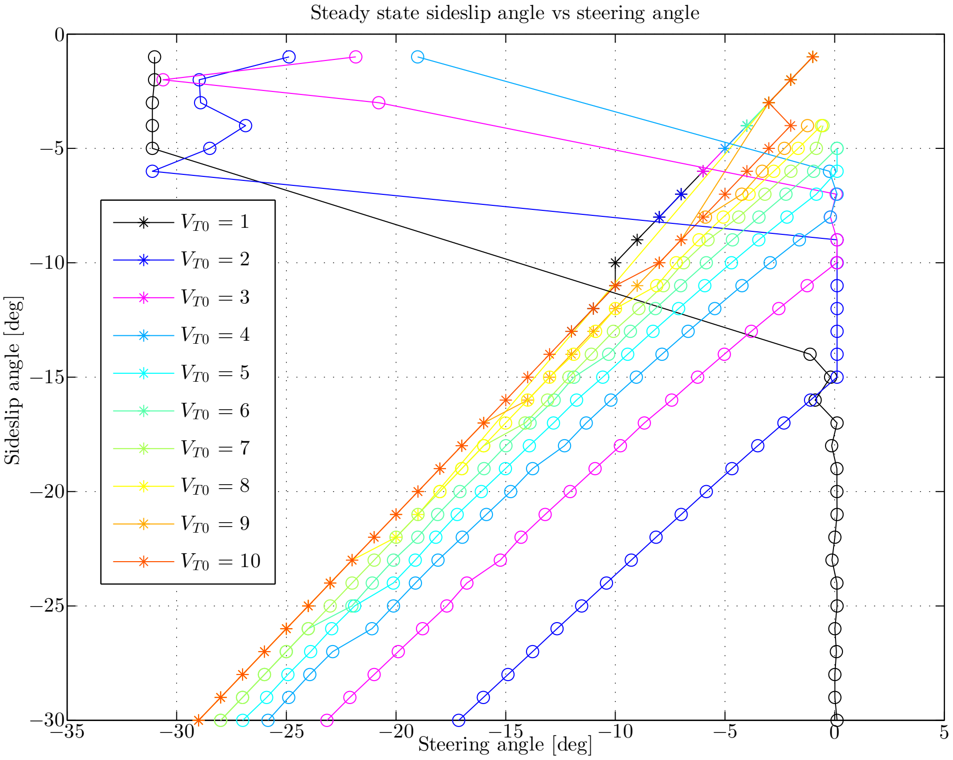

Figure 7.1: Steady state values for the sideslip angle versus steering angle, with colour coded speed.

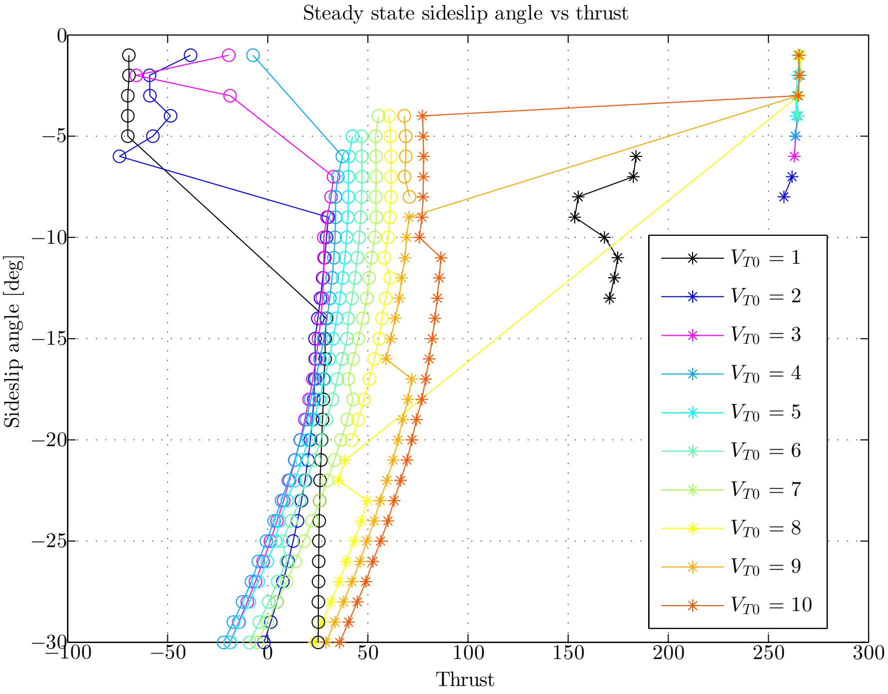

Figure 7.2: Steady state values for sideslip angle versus thrust input, with colour coded speed.

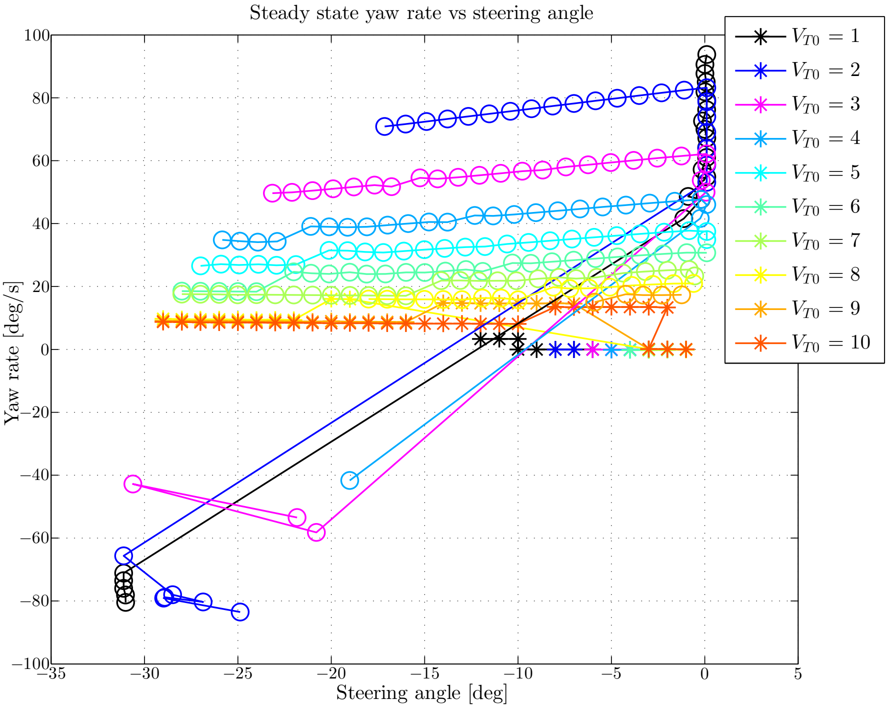

Figure 7.3: Steady state values for yaw rate versus steering angle, with colour coded speed.

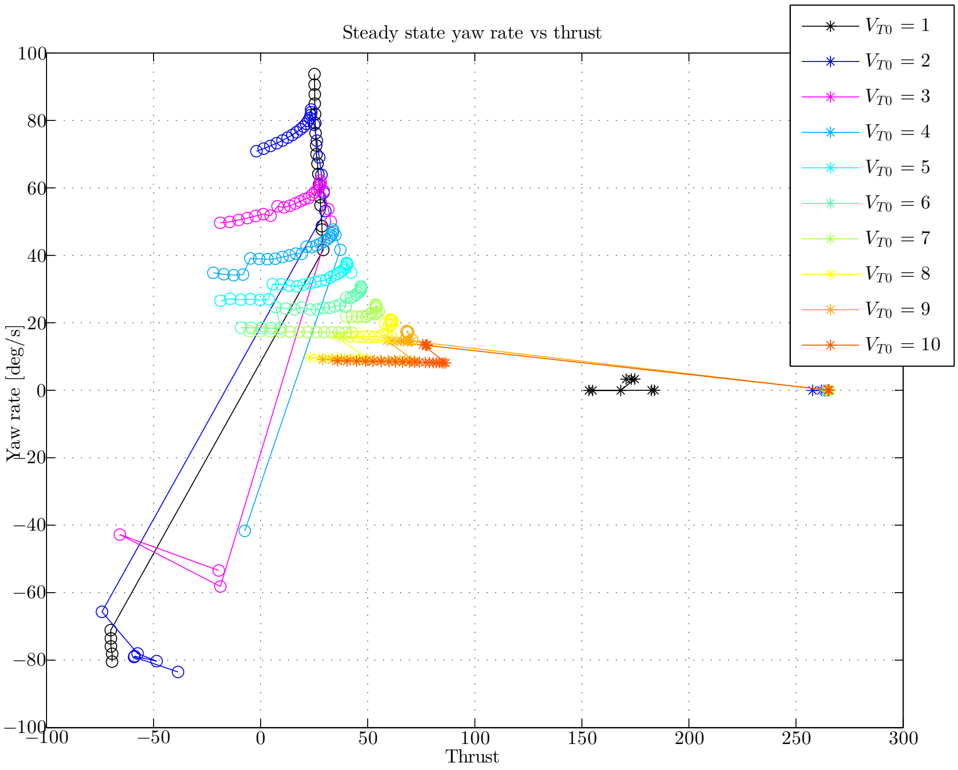

Figure 7.4: Steady state values for yaw rate versus thrust, with colour coded speed.

Now by discarding the infeasible equilibria and the cluster with negative yaw rate, the remaining points are all the feasible drifting equilibria for a left handed turn. And these points are shown in figure 7.5 to 7.8.

For a constant speed, there is an approximate linear mapping between the wheel turning angle and the sideslip angle, seen in figure 7.5. The steering angle starts close to zero for speeds of 4 to 9 m/s, and decrease linearly from this point. For speeds of 2-3 m/s, there are several points with steering angle close to zero before the linear relationship can be seen. Equilibria with speed of 1 m/s stand out here, with starting steering angle of -2° and ending up with close to zero steering angle.

The sideslip angle as function of the thrust input, for constant speed, could be approximated by a second order function, from figure 7.6. Equilibria with speed of 1 m/s, stand out here as well, with close to constant thrust for all sideslip angles.

In figure 7.7, the yaw rate as function of the wheel turning angle, for constant speed, could be linearly mapped for wheel turning angles less than zero degrees. Notice the equilibria with the largest yaw rate, have the smallest steering angle. In addition, an increase of speed causes the maximum yaw rate to decrease.

From figure 7.8, for constant speed, the yaw rate as function of thrust input could be mapped as an exponential function up to and including the equilibriums with the largest yaw rate. The equilibria corresponding to the largest yaw rate has a lower thrust, than the equilibria with the lowest sideslip angle for speeds of 1 to 5 m/s. These equilibria correspond to the ones with steering angle close to zero in figure 7.5 and 7.7. This behaviour shows that for small sideslip angles the thrust plays an important role for the drift. The steady state values for speed of 1 m/s, where the change in only changes about 1° and a thrust reduction of 4 N causes an increase in yaw rate of 52 deg/s.

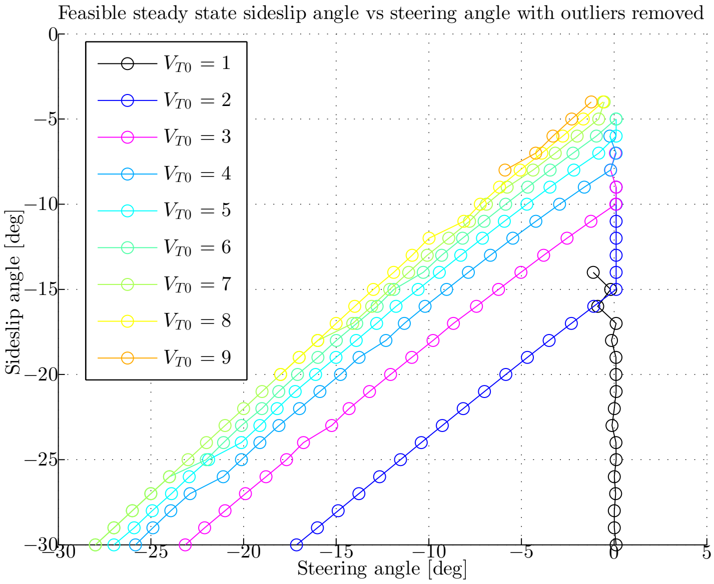

Figure 7.5: Only feasible steady state values for sideslip angle versus steering angle, with colour coded speed. Outliers with negative yaw rate have been removed.

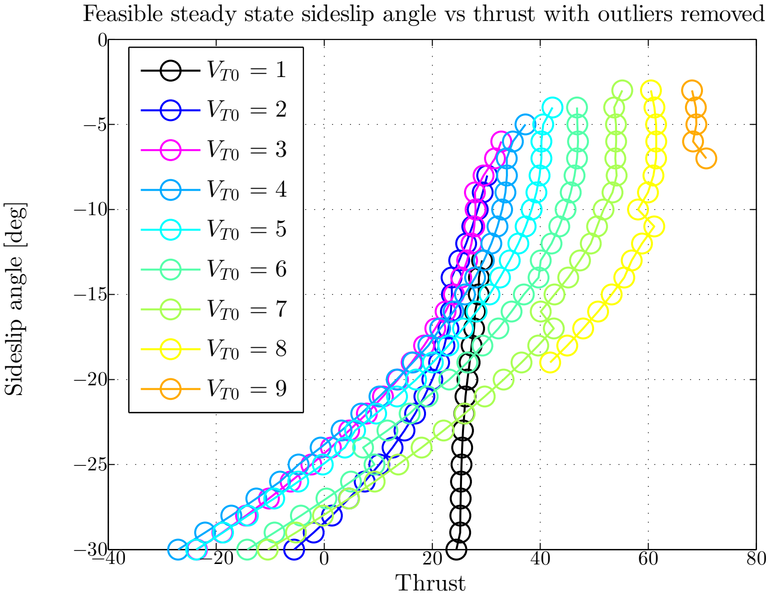

Figure 7.6: Only the feasible steady state values for sideslip angle versus thrust, with colour coded speed. Outliers with negative yaw rate have been removed.

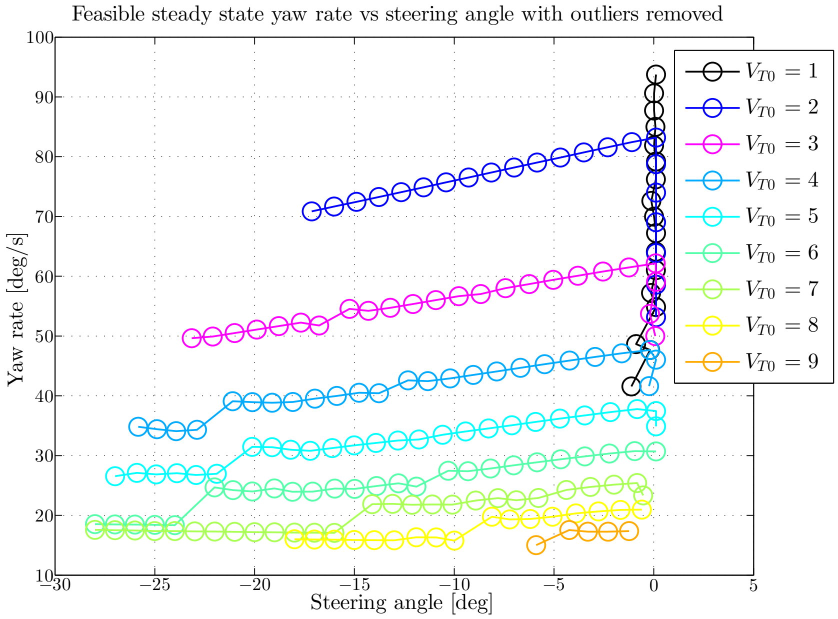

Figure 7.7: Only feasible steady state values for yaw rate versus steering angle, with colour coded speed. Outliers with negative yaw rate have been removed.

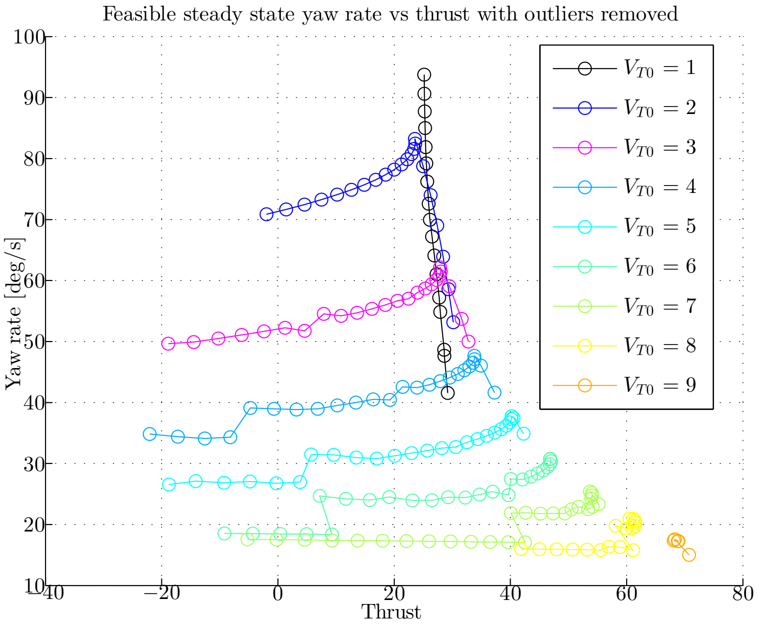

Figure 7.8: Only the feasible steady state values for yaw rate versus thrust, with colour coded speed. Outliers with negative yaw rate have been removed.

To manage a corner in the fastest way possible, the yaw rate should be maximised. The sideslip angles β with maximum yaw rate $\dot{\psi}$ for different speeds V_T are shown in table 7.1

Table 7.1: Notations for the DC motor model equation

Speed [m/s]	Max yaw rate [deg/s]	Sideslip angle [deg]
1	93.7470	30
2	83.2072	15
3	62.1542	10
4	47.6676	8
5	37.7680	7
6	30.7587	6
7	25.4051	5
8	20.9641	4
9	17.5521	7
10	0	0

Note that with a speed of 10 m/s there is no steady state drifting condition, which indicates that the drifting should be performed at lower speeds. As can be seen from table 7.1, the maximum yaw rate increases with decreasing speed.

7.2 Pole Movements

To be able to inspect the pole movements of the equilibria used in section 7.1, a linearisation was performed following the method described in section 6.1.

Figure 7.9 shows all the poles in the complex plane, with colours reflecting vehicle speed at linearisation point. Three different figures have been used to distinguish three poles, a star, $\star$, square, $\square$, and a cross, $\times$. As can be seen from figure 7.9, at speed of 1 m/s the poles are far into the right half plane. With increasing speed the poles move closer to the imaginary axis, however all the poles remain in the right half plane. All poles being in the right half plane correspond with the findings in [7] and [8]. From speeds of 2 m/s and up, two of the poles take imaginary values. The imaginary values increase with increased speeds, which can be seen from figure 7.11.

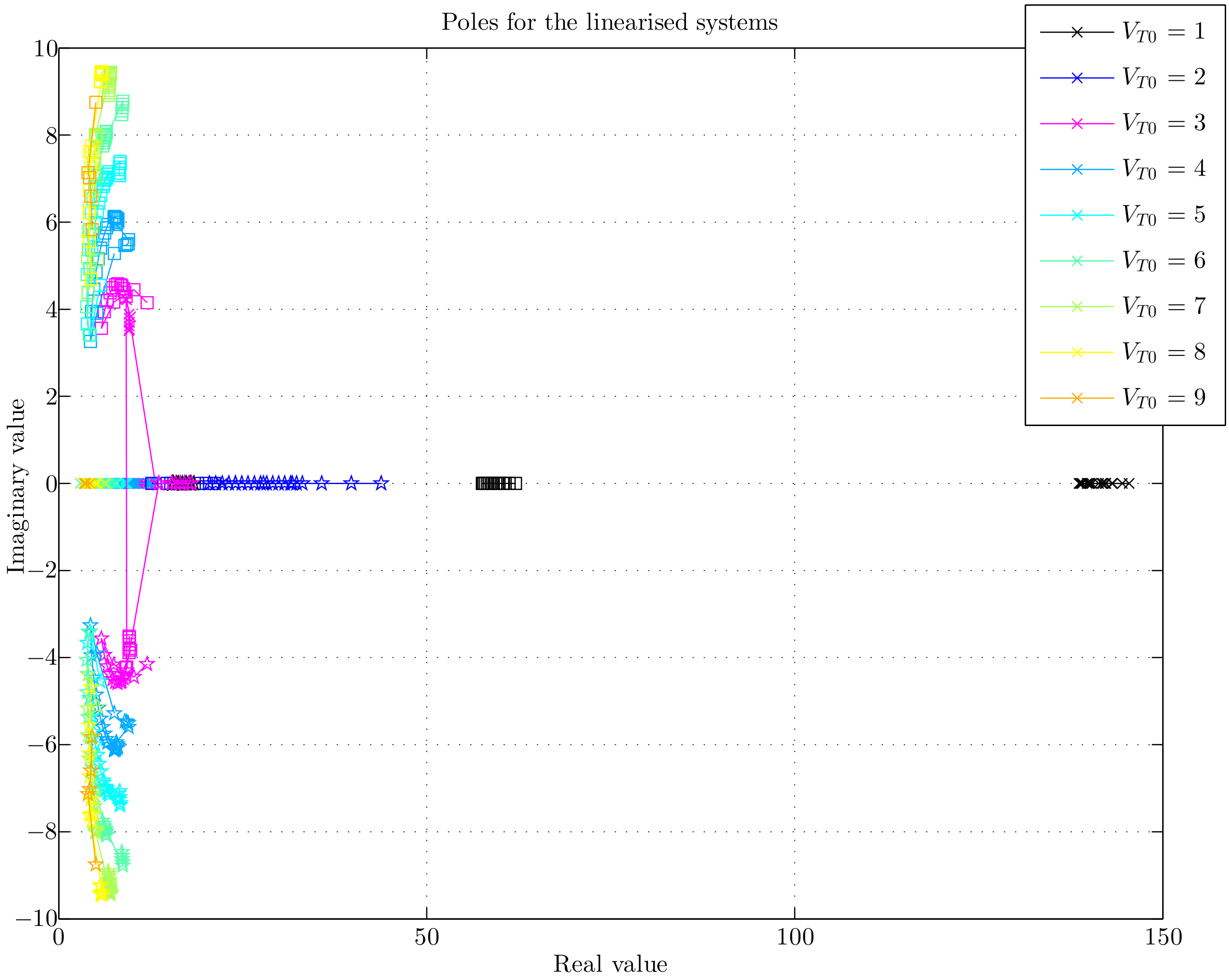

Figure 7.9: The poles of the system for different sideslip angles and speeds.

In figure 7.10 and 7.11 arrows have been added from the lowest to the largest sideslip angle, for each pole at constant speed. The arrows follow the same colour coding as the poles.

The poles seem to move closer to the imaginary axis for increased sideslip angle to a certain point and then move further into the right half plane. This suggests that for a given constant speed, there is one equilibrium that has slower dynamics than the others. And thus the linearised system in this equilibrium is easier to stabilize by means of a controller. The equilibria move closer to the imaginary axis with increased yaw rate and begin moving further into the right half plane after the peak in the yaw rate.

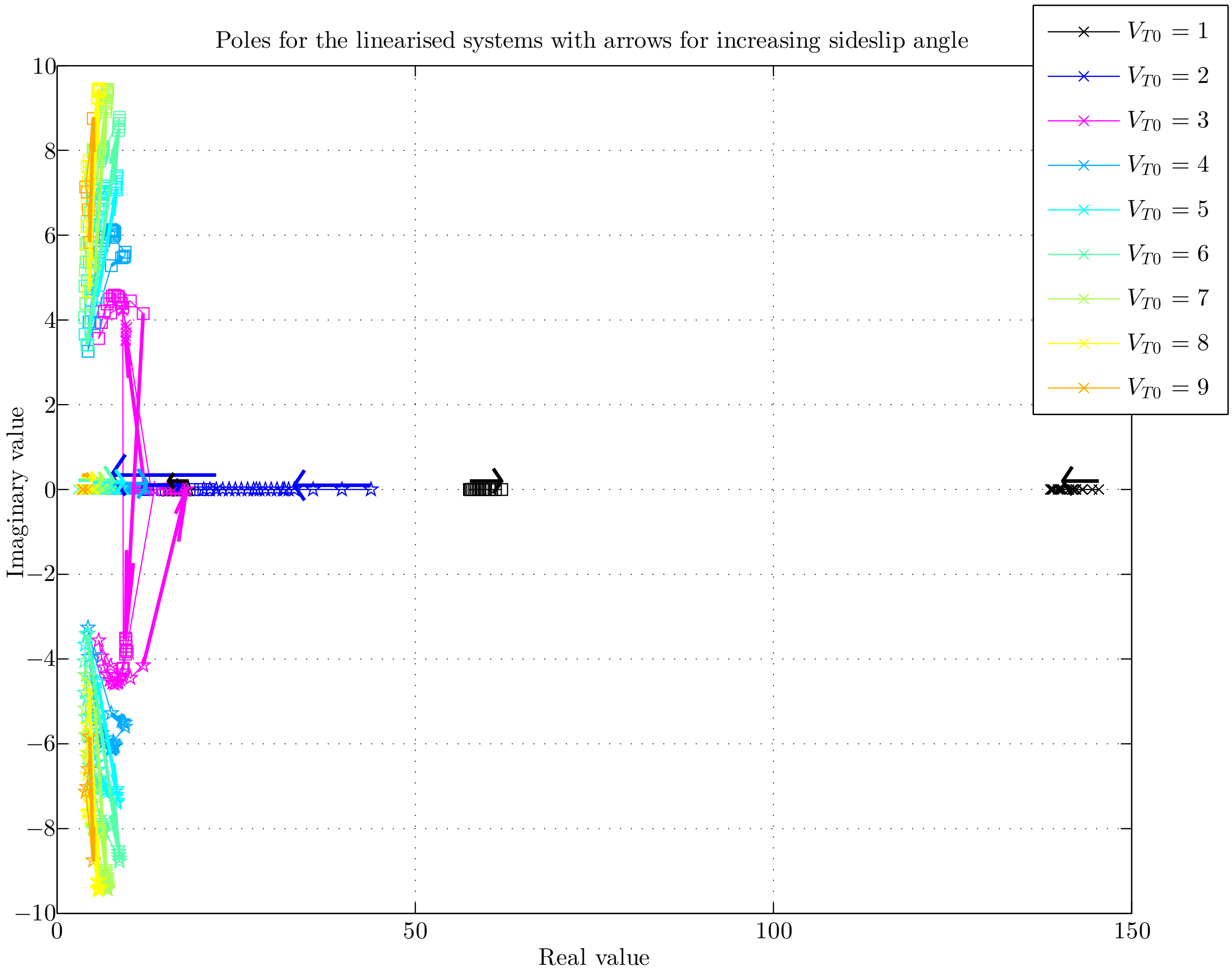

Figure 7.10: The poles of the system for different sideslip angles and speeds, with arrows from lowest to largest sideslip angle.

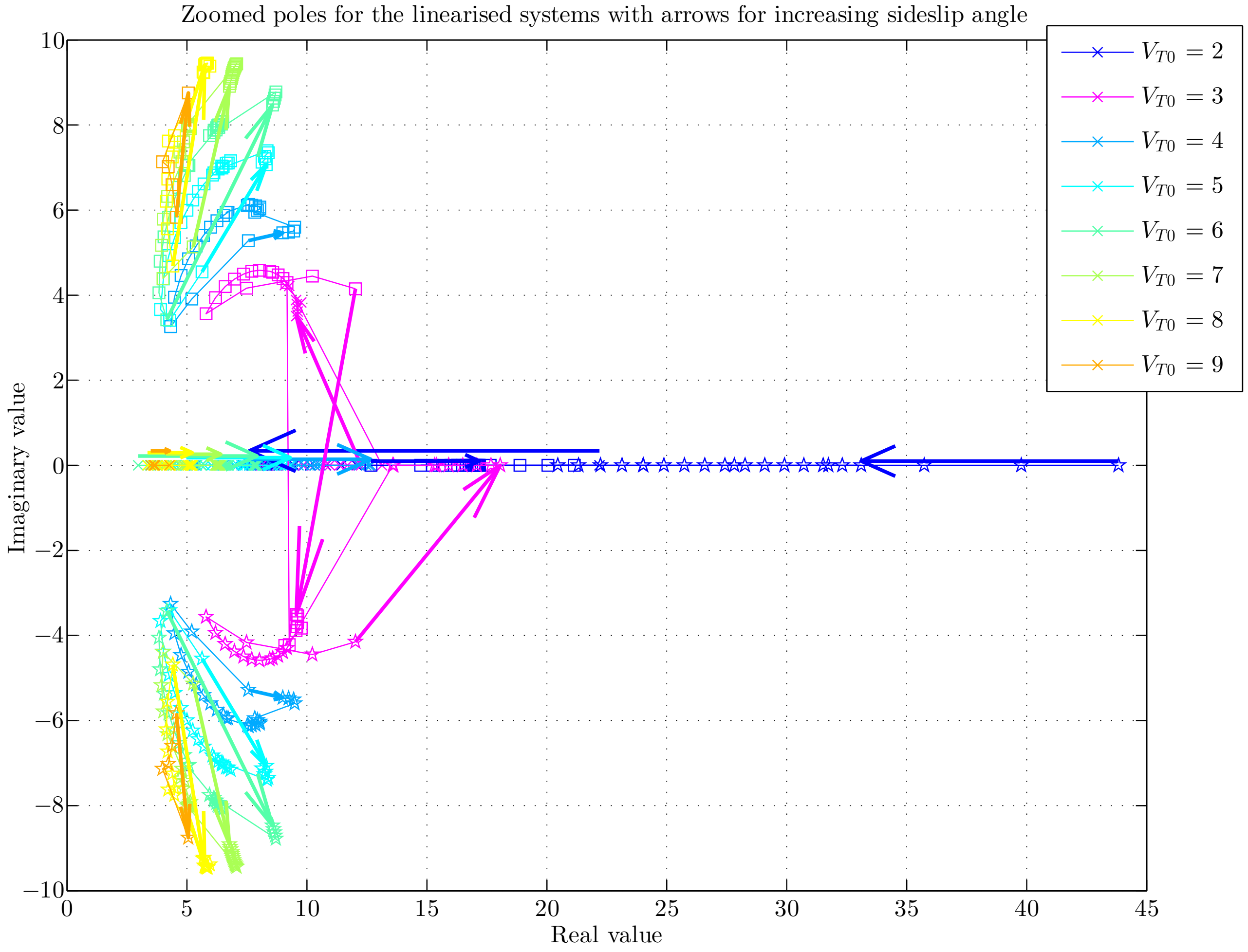

Figure 7.11: Zoomed poles of the system for different sideslip angles and speeds, with arrows from lowest to largest sideslip angle.

In the following chapters, the controllers will try to converge to equilibria at speeds of 3 m/s. This speed was chosen because the yaw rate for this speed is quite good and the mappings from input to state is smooth, shown in figure 7.5 to 7.8. A higher speed could be chosen for better mapping or a lower speed could have been chosen for a larger yaw rate, however 3 m/s gives an adequate combination of mapping and yaw rate. The mapping will be used for a lookup table in a feed forward described in section 8.5.

7.3 Discussion of Steady State Analysis

At constant speeds, simple mappings for the equilibrium values can be used to describe the relationship between the sideslip angle and the two inputs to the system, steering angle and thrust. The same can be said for the yaw rate. These mapping are valid for steering angles below -1°. At low speeds there are several steady state values with close to zero steering angle which move differently than the remaining equilibria.

It was found that the equilibrium points with the lowest steering angles corresponded to the equilibriums with the largest yaw rate. As well as an increase in speed caused the maximum yaw rate to decrease. Which is intuitively correct; trying to take a corner at higher speeds makes the turning radius larger.

All the poles for the drifting equilibriums are in the right half plane. However, the poles move closer to the imaginary axis for increased yaw rate. This means that even though all the equilibriums are unstable, some are easier to stabilize than others. A simple first test for a controller should be converging to a equilibrium with the largest yaw rate for a constant speed, which would be the easiest control objective.

8 Guidance and Control

Because the system has three states and the vehicle only has two control inputs, the system is underactuated. This problem is solved by cascade coupling of the controllers for sideslip angle β and the yaw rate $\dot{\psi}$. Thus the controller for sideslip gives a reference to the yaw rate controller.

A drifting technique is needed to be able to drift, and there are several to choose from; E-brake, Clutch Kick, Power Over and many more [19]. In this thesis the Power Over method was chosen, where the steering angle is aggressively increased at the same time as the thrust is increased to get the car to oversteer. When the car is oversteering, the controller needs to converge to a drifting equilibrium by countersteering. By using a steering controller for either the side force input Y_w or the yaw moment input N_w, the thrust can be dominated by the steering controller if equation (5.78) holds. Which means that the Power Over drifting can be achieved if the gains on the steering controller are large enough.

A sliding mode controller was developed and found wanting regarding convergence. The controller design can be found in appendix A, which also contains stability proofs for the controller.

A proportional controller for the sideslip angle is developed in section 8.1. The P controller needed integral action and this is provided by an adaptive backstepping controller which is developed in section 8.2. A PID controller for the speed and a baseline steering PID controller are described in section 8.3. Line of sight guidance used in this thesis is derived in section 8.4. Then the feed forward and state derivatives needed for implementation can be found in section 8.5. Lastly, the Simulink implementation is described in section 8.6.

8.1 Sideslip Proportional Controller

A radially unbounded Lyapunov function candidate(LFC) is used for deriving the controllers for sideslip and heading rate

$$V = \frac{1}{2}\tilde{\beta}^2 + \frac{1}{2}I_{zz}\dot{\tilde{\psi}}^2 \; > 0 \; \forall(\tilde{\beta}, \dot{\tilde{\psi}}) \neq (0,0) \tag{8.1}$$

where V is the Lyapunov function candidate, $\tilde{\beta}$ and $\tilde{\psi}$ are the deviation from the desired β and ψ respectively. That is

$$\tilde{\beta} = \beta - \beta_d \tag{8.2}$$

$$\dot{\tilde{\psi}} = \psi - \psi_d \tag{8.3}$$

Firstly the course angle χ and the derivative of the course angle $\dot{\chi}$ are defined as

$$\chi = \psi + \beta \tag{8.4}$$

$$\dot{\chi} = \dot{\psi} + \dot{\beta} \tag{8.5}$$

The derivative of the Lyapunov function along the trajectory of the system is

$$\begin{aligned} \dot{V} &= \tilde{\beta}\dot{\tilde{\beta}} + \dot{\tilde{\psi}} I_{zz} \ddot{\tilde{\psi}} \\ &= \tilde{\beta}(\dot{\beta} - \dot{\beta}_d) + \dot{\tilde{\psi}}(I_{zz}\ddot{\psi} - I_z\ddot{\psi}_d) \end{aligned} \tag{8.6}$$

By inserting $\dot{\beta}$ = $\dot{\chi}$ - $\dot{\psi}$ from equation (8.5) and $I_z\ddot{\psi}$ = N_w + (I_{xx} - I_{yy})pq from yaw acceleration equation in (4.18), $\dot{V}$ becomes

$$\dot{V} = \tilde{\beta}(\dot{\chi} - \dot{\psi} - \dot{\beta}_d) + \dot{\tilde{\psi}}(N_w + (I_{xx} - I_{yy})pq - I_{zz}\ddot{\psi}_d) \tag{8.7}$$

From equation (8.3), $\dot{\psi}$ = $\dot{\tilde{\psi}}$ + $\dot{\psi}_d$ is inserted into (8.7), which yields

$$\dot{V} = \tilde{\beta}(\dot{\chi} - \dot{\tilde{\psi}} - \dot{\psi}_d - \dot{\beta}_d) + \dot{\tilde{\psi}}(N_w + (I_{xx} - I_{yy})pq - I_{zz}\ddot{\psi}_d) \tag{8.8}$$

The yaw rate reference $\dot{\psi}_d$ and the yaw moment N_w are chosen as

$$\dot{\psi}_d = \dot{\chi}_d - \dot{\beta}_d + k_b\tilde{\beta} \tag{8.9}$$

$$N_w = I_{zz}\ddot{\psi}_d - k_r\dot{\tilde{\psi}} - (I_{xx} - I_{yy})pq \tag{8.10}$$

where k_b and k_r are positive gains. With equation (8.9) and (8.10), $\dot{V}$ becomes

$$\begin{aligned} \dot{V} &= \tilde{\beta}(\dot{\chi} - \dot{\tilde{\psi}} - \dot{\chi}_d + \dot{\beta}_d - k_b\tilde{\beta} - \dot{\beta}_d) + \dot{\tilde{\psi}}(I_{zz}\ddot{\psi}_d - k_r\dot{\tilde{\psi}} - I_{zz}\ddot{\psi}_d) \\ &= \tilde{\beta}(\dot{\chi} - \dot{\chi}_d - \dot{\tilde{\psi}} - k_b\tilde{\beta}) - k_r\dot{\tilde{\psi}}^2 \end{aligned} \tag{8.11}$$

By the assumption that $\dot{\chi}$ = $\dot{\chi}_d$

$$\dot{V} = -k_b\tilde{\beta}^2 - \tilde{\beta}\dot{\tilde{\psi}} - k_r\dot{\tilde{\psi}}^2 \tag{8.12}$$

$$= -\begin{bmatrix} \tilde{\beta} & \dot{\tilde{\psi}} \end{bmatrix} \begin{bmatrix} k_b & \frac{1}{2} \\ \frac{1}{2} & k_r \end{bmatrix} \begin{bmatrix} \tilde{\beta} \\ \dot{\tilde{\psi}} \end{bmatrix} = -\begin{bmatrix} \tilde{\beta} & \dot{\tilde{\psi}} \end{bmatrix} Q \begin{bmatrix} \tilde{\beta} \\ \dot{\tilde{\psi}} \end{bmatrix} \tag{8.13}$$

A positive definite Q is needed to make $\dot{V}$ strictly negative. Which means that the determinant of Q needs to be positive

$$\begin{aligned} k_b k_r - \frac{1}{4} &> 0 \\ k_r &> \frac{1}{4k_b} \end{aligned} \tag{8.14}$$

By choosing the gains according to the inequality in equation (8.14), $\dot{V}$ becomes strictly negative. With a strictly negative $\dot{V}$ and a strictly positive radially unbounded V, the system is globally asymptotically stable according to [20].

Stationary deviation in the sideslip angle was observed during simulation, indicating need of integral action. Integral action will be implemented by means of an adaptive backstepping controller derived in the next section.

8.2 Adaptive Backstepping Controller

An adaptive backstepping controller will be derived, for a system influenced by a constant disturbance. Integral action is needed to remove the disturbance and it will be achieved by parameter adaptation.

In [21], a system is defined on the form

$$\dot{x}_1 = h(x_1, t) + G(x, t)x_2 \tag{8.15}$$

$$\dot{x}_2 = -PG(x, t)^T \left(\frac{\partial W(x_1, t)}{\partial x_1} \right), \; P = P^T > 0 \tag{8.16}$$

where $x_1 \in \mathbb{R}^{n_1}$, $x_2 \in \mathbb{R}^{n_2}$ and W is a function with a continuous first order derivative, which maps $\mathbb{R}^{n_1} \times \mathbb{R}_{\geq 0} \to \mathbb{R}_{\geq 0}$. The function W also upholds assumption A2 stated below.

According to Theorem 1 in [21]: if the system stated in equations (8.15) to (8.16) upholds the assumptions A1 and A2 below, the system has uniform global asymptotic stability (UGAS). The assumptions are as follows

A1. Define $G_0(x_2, t) := G(x_2, t)|_{x_1 \equiv 0}$. Assume that there exist continuous nondecreasing functions ρ_j: $\mathbb{R}_{\geq 0} \to \mathbb{R}_{\geq 0}$, ($j$ = 1, 2, 3) such that, for all $t \geq 0$, $x \in \mathbb{R}^{n_1 + n_2}$

$$\max\left\{ \|h(x_1, t)\|, \left\| \frac{\partial W(x_1, t)}{\partial x_1} \right\| \right\} \leq \rho_1(\|x_1\|)\|x_1\| \tag{8.17}$$

$$\max\left\{ \|G(x, t)\|, \|G_0(x_2, t)\| \right\} \leq \rho_2(\|x\|) \tag{8.18}$$

$$\max\left\{ \left\| \frac{\partial G_0(x_2, t)}{\partial((x_2)_i)} \right\|, \left\| \frac{\partial G_0(x_2, t)}{\partial t} \right\| \right\} \leq \rho_3(\|x_2\|), \; i \in \{1, \; \dots \;, n_2\} \tag{8.19}$$

In addition, for each compact set $K \subset \mathbb{R}^{n_2}$ there exists $b_m > 0$ such that

$$G_0(x_2, t)^T G_0(x_2, t) \geq b_m I_{n_2 \times n_2} \tag{8.20}$$

for all $(x_2, t) \in K \times \mathbb{R}_{\geq 0}$.

A2. There exist class-$\mathscr{K}_\infty$ functions α_1 and α_2 and a strictly positive real number $c > 0$ such that

$$\alpha_1(\|x_1\|) \leq W(x_1, t) \leq \alpha_2(\|x_1\|) \tag{8.21}$$

$$\frac{\partial W(x_1, t)}{\partial t} + \frac{\partial W(x_1, t)}{\partial x_1} h(x_1, t) \leq -c\|x_1\|^2 \tag{8.22}$$

Also, if α_2(s) is proportional to s^2 for sufficiently small s then the origin has uniform local exponential stability (ULES).

A class $\mathscr{K}_\infty$ is defined as:
If a function α: [0,a) $\rightarrow$ [0,∞) is a class $\mathscr{K}_\infty$ function, then α is a strictly increasing continuous function with α(0) = 0 and if a = ∞ then α(r) $\rightarrow \infty$ as r $\rightarrow \infty$ [20].

The system being controlled can be found by inserting equations (5.1) and (5.3) into yaw acceleration equation in (4.18), which yields

$$\dot{y} = \dot{\beta} \tag{8.23}$$

$$I_{zz}\ddot{\psi} = N_w + (I_{xx} - I_{yy})pq + \phi^T\theta \tag{8.24}$$

$$\dot{\theta} = 0 \tag{8.25}$$

where the regressor ϕ = 1 is a measurement and θ is an unknown constant disturbance.

The error states can be expressed as

$$\dot{\tilde{y}} = \dot{\tilde{\beta}} = \dot{\beta} - \dot{\beta}_d \tag{8.26}$$

$$I_{zz}\ddot{\tilde{\psi}} = N_w + (I_{xx} - I_{yy})pq + \theta - I_{zz}\ddot{\psi}_d \tag{8.27}$$

$$\dot{\tilde{\theta}} = \dot{\hat{\theta}} - \dot{\theta} = \dot{\hat{\theta}} \tag{8.28}$$

where $\tilde{\theta}$ is the deviation between estimated disturbance $\hat{\theta}$ and actual disturbance θ. And $\dot{\beta}_d$ and $\ddot{\psi}_d$ are the desired sideslip angle rate and yaw angular acceleration respectively.

As can be seen from equations (8.27), the disturbance θ and the control input N_w appear in the same equation, which means that matching between N_w and θ can be done directly.

The backstepping is started by defining $z_1 = \tilde{\beta}$, and the calculation is as follows

$$\dot{z}_1 = \dot{\beta} - \dot{\beta}_d = \dot{\chi} - \dot{\tilde{\psi}} - \dot{\psi}_d - \dot{\beta}_d \tag{8.29}$$

where equations (8.5) and (8.3) have been solved for $\dot{\beta}$ and $\dot{\psi}$ respectively and inserted.

Now z_2 is chosen as

$$z_2 = \dot{\tilde{\psi}} - \alpha \tag{8.30}$$

Thus $\dot{z}_1$ becomes

$$\dot{z}_1 = \dot{\chi} - z_2 - \alpha - \dot{\psi}_d - \dot{\beta}_d \tag{8.31}$$

Choosing the stabilizing function α as

$$\alpha = \dot{\chi} - \dot{\psi}_d - \dot{\beta}_d + k_1 z_1 \tag{8.32}$$

yields

$$\dot{z}_1 = -k_1 z_1 - z_2 \tag{8.33}$$

The time derivative of z_2 is found by using equation (8.27)

$$\begin{aligned} \dot{z}_2 &= \ddot{\tilde{\psi}} - \dot{\alpha} \\ I_{zz}\dot{z}_2 &= N_w + (I_{xx} - I_{yy})pq + \theta - I_{zz}\ddot{\tilde{\psi}}_d - I_{zz}\dot{\alpha} \\ &= N_w + (I_{xx} - I_{yy})pq + (\hat{\theta} - \tilde{\theta}) - I_{zz}\ddot{\tilde{\psi}}_d - I_{zz}\dot{\alpha} \end{aligned} \tag{8.34}$$

Now a radially unbounded LFC $V_1 = 0.5z_1^2 + (1/2p)\tilde{\theta}^2$ will be used, where p > 0 and $\tilde{\theta}$ is the parameter estimation error. The time derivative of the LFC V_1 is

$$\begin{aligned} \dot{V}_1 &= z_1\dot{z}_1 + \frac{1}{p}\tilde{\theta}\dot{\hat{\theta}} \\ &= -k_1 z_1^2 - z_1 z_2 + \frac{1}{p}\tilde{\theta}\dot{\hat{\theta}} \end{aligned} \tag{8.35}$$

where (8.33) has been inserted.

The next step is to introduce the radially unbounded LFC $V_2 = V_1 + 0.5I_{zz}z^2$, with time derivative along the trajectories of the system, described in (8.33) and (8.34). This yields

$$\begin{aligned} \dot{V}_2 &= \dot{V}_1 + z_2 I_{zz}\dot{z}_2 \\ &= -k_1 z_1^2 - z_1 z_2 + \frac{1}{p}\tilde{\theta}\dot{\hat{\theta}} + z_2(N_w + (I_{xx} - I_{yy})pq + (\hat{\theta} - \tilde{\theta}) - I_{zz}\ddot{\tilde{\psi}}_d - I_{zz}\dot{\alpha}) \\ &= -k_1 z_1^2 - z_1 z_2 + \tilde{\theta}(\frac{1}{p}\dot{\hat{\theta}} - z_2) + z_2(N_w + (I_{xx} - I_{yy})pq + \hat{\theta} - I_{zz}\ddot{\tilde{\psi}}_d - I_{zz}\dot{\alpha}) \end{aligned} \tag{8.36}$$

Choosing the adaptation and control law as

$$\dot{\hat{\theta}} = pz_2 \tag{8.37}$$

$$N_w = z_1 - (I_{xx} - I_{yy})pq - \hat{\theta} + I_{zz}\ddot{\tilde{\psi}}_d + I_{zz}\dot{\alpha} - k_2 z_2 \tag{8.38}$$

the following is obtained

$$\dot{V}_2 = -k_1 z_1^2 - k_2 z_2^2 \leq 0 \tag{8.39}$$

The LFC V_2 is positive and has non-positive derivative, thus V_2 is a Lyapunov function for the error system in equations (8.26) to (8.28).

The system can now be expressed with variables z_1, z_2 and $\tilde{\theta}$ as

$$\begin{bmatrix} \dot{z}_1 \\ \dot{z}_2 \end{bmatrix} = \begin{bmatrix} -k_1 & -1 \\ \dfrac{1}{I_{zz}} & -\dfrac{k_2}{I_{zz}} \end{bmatrix} \begin{bmatrix} z_1 \\ z_2 \end{bmatrix} + \begin{bmatrix} 0 \\ -\dfrac{1}{I_{zz}} \end{bmatrix} \tilde{\theta} \tag{8.40}$$

$$\dot{\tilde{\theta}} = -p \begin{bmatrix} 0 & -\dfrac{1}{I_{zz}} \end{bmatrix} \begin{bmatrix} z_1 \\ I_{zz} z_2 \end{bmatrix} \tag{8.41}$$

Because V_2 has a non-increasing derivative, LaSalle's theorem can be invoked, see [20]. Since V_2 is radially unbounded, the set $\Omega_c = \{z \in \mathbb{R}^2, \theta \in \mathbb{R} \mid \dot{V}_2 \leq 0\}$ is a compact positively invariant set. The set $E = \{z \in \Omega_c, \theta \in \Omega_c \mid z_1 = z_2 = 0\}$, where every point on the line $z_1 = z_2 = 0$ is an invariant set.

To test the set E, the values for the invariant set E are inserted into equations (8.40) and (8.41), which leads to

$$\dot{z}_1 = 0 \tag{8.42}$$

$$\dot{z}_2 = 0 = -\frac{1}{I_{zz}} \tilde{\theta} \tag{8.43}$$

$$\dot{\tilde{\theta}} = 0 \tag{8.44}$$

where it can be concluded that every trajectory starting in Ω_c approaches E as time goes to infinity. Because V_2 is radially unbounded, the system has UGAS. However, theorem 1 stated above can prove ULES for the system.

The assumption A1 and A2 need to be fulfilled for theorem 1 to hold. While comparing the system in equations (8.40)-(8.41) to the systems in equations (8.15)-(8.16), the following variables can be renamed as

$$x_1 = [z_1,\ z_2]^T \tag{8.45}$$
$$x_2 = \tilde{\theta} \tag{8.46}$$
$$P = p \tag{8.47}$$
$$G(x,t) = \left[0,\ -\frac{1}{I_{zz}}\right]^T \tag{8.48}$$
$$h(x_1,t) = \begin{bmatrix} -k_1 & -1 \\ \frac{1}{I_{zz}} & -\frac{k_2}{I_{zz}} \end{bmatrix} \tag{8.49}$$
$$W(x_1) = \frac{1}{2}(z_1^2 + I_{zz}z_2^2) \tag{8.50}$$

The system has already been proven to be UGAS, such that only $\alpha_2(\|x_1\|)$ in equation (8.21) needs to be found. By studying $W(x_1)$ in equation (8.50), both $\alpha_1(\|x_1\|)$ and $\alpha_2(\|x_1\|)$ can be chosen as

$$\alpha_1(\|x_1\|) = \alpha_2(\|x_1\|) = 2W(x_1) = \|x_1\|^2 \tag{8.51}$$

Because $\alpha_2(\|x_1\|)$ is proportional to $\|x_1\|^2$, the error dynamics in equations (8.40) and (8.41) are ULES.

The controller has integral action in the inner loop. However, if the yaw rate for the equilibrium that corresponds to current desired sideslip angle β_d and desired speed $V_{T,d}$ is known and fed to the controller, the result would be that the equilibrium will be reached which means that the sideslip angle converges. This will be done by means of a feed forward term $\dot{\psi}_{d,ff}$, which is included in the injection term α. This leads to

$$\alpha = \dot{\chi} - \dot{\psi}_d - \dot{\beta}_d + k_1 z_1 + \dot{\psi}_{d,ff} \tag{8.52}$$

See section 8.5 for more information on $\dot{\psi}_{d,ff}$.

8.3 Speed Controller and Baseline Steering Controller

The speed controller was chosen as a PID controller. Integral action was used to remove stationary deviations. It is on the form

$$X_w = -k_p\tilde{V}_T - k_i\int_0^t \tilde{V}_T(\tau)d\tau \tag{8.53}$$

where k_p and k_i are positive gains, and

$$\tilde{V}_T = V_T - V_{T,d} \tag{8.54}$$

is the speed deviation from desired speed.

A baseline PID controller for steering was developed based on pole placement for the linearised systems from section 7.2. This controller will be compared with the adaptive backstepping controller by means of simulation, in section 9.4.

By using equation (6.51), and inserting $\Delta\mathbf{u}$ = -KΔx, the system on pole placement form is gotten

$$\Delta\dot{\mathbf{x}} = \mathbf{A}\Delta\mathbf{x} - \mathbf{B}\mathbf{K}\Delta\mathbf{x} = (\mathbf{A} - \mathbf{B}\mathbf{K})\Delta\mathbf{x} \tag{8.55}$$

where $\mathbf{K}$ is a chosen gain matrix to move the poles of $(\mathbf{A} - \mathbf{B}\mathbf{K})$ to the desired location.

First the 3 DOF linearised system needs to be transformed to include the total speed V_T and sideslip angle β instead of longitudinal velocity u and lateral velocity v. From the relationship in equation (2.1)

$$V_T = \frac{u}{\cos(\beta)} \tag{8.56}$$

$$\beta = \arcsin\left(\frac{v}{V_T}\right) \tag{8.57}$$

Thus the first row of A and B are divided by $\cos(\beta)$ and $\arcsin\left(\frac{derivative}{V_T}\right)$ was performed on the second row, which transforms the state vector $\mathbf{x}$ from $[u, v, \dot{\psi}]^T$ to $[\ V_T, \beta, \dot{\psi}]^T$.

For speed V_T = 3 m/s, the poles for $(\mathbf{A} - \mathbf{B}\mathbf{K})$ are placed at (-2, -5, -5), and the resulting gain matrix is

$$\mathbf{K} = \begin{bmatrix} -0.0319 & -0.1370 & -0.0999 \\ 84.8937 & -27.5471 & -37.6267 \end{bmatrix} \tag{8.58}$$

Tests were performed to place the poles further into the left half plane for faster convergence, however this only caused oscillations during simulation. The chosen poles were the furthest into the left half plane without these oscillations.

8.4 Line Of Sight Guidance

The controller needs references to follow, and these are created by the guidance system. Straight line following using Line of sight (LOS) will be described in this section.

The course angle is given in equations (8.4) and is repeated here for convenience

$$\chi = \psi + \beta \tag{8.59}$$

Following the derivations in [14], a desired course angle can be split into two parts

$$\chi_d(\mathrm{e}) = \chi_p + \chi_r(\mathrm{e}) \tag{8.60}$$

where

$$\chi_p = \alpha_k \tag{8.61}$$

is the path-tangential angle shown in figure 8.1, and

$$\chi_r(\mathrm{e}) = \arctan\left(\frac{-\mathrm{e}}{\Delta}\right) \tag{8.62}$$

is the velocity-path relative angle, the variable e is the cross-track error and Δ is the lookahead distance. The cross-track error and lookahead distance are shown in figure 8.1. This kind of guidance system, where the velocity is directed at a point on a path, is called lookahead-based steering.

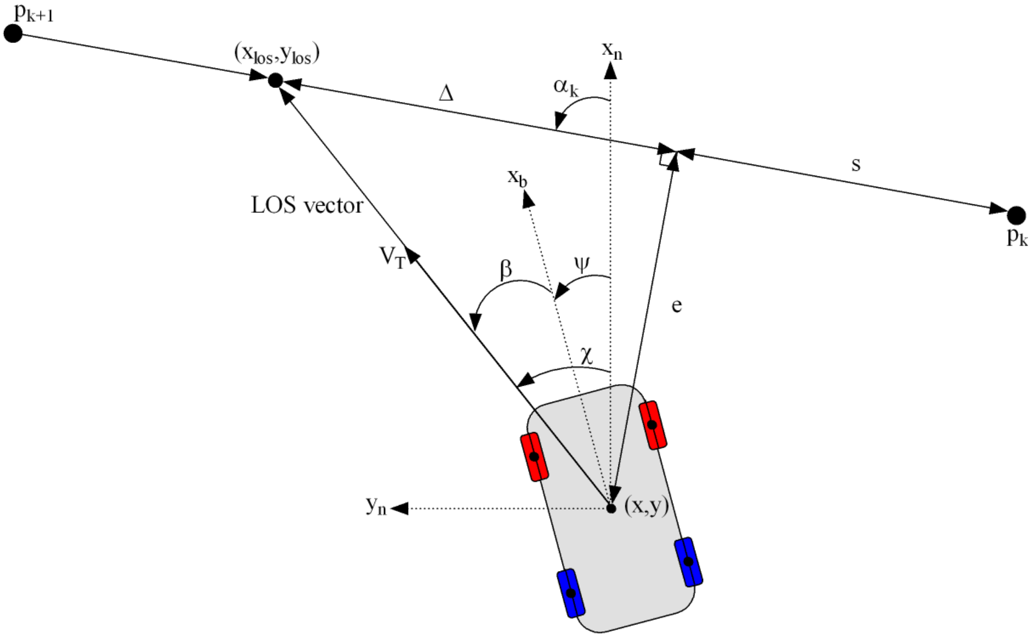

Figure 8.1: LOS guidance where the velocity is pointing towards the LOS intersection point.

Path following is accomplished by velocity-path relative angle χ_r that ensures the velocity is directed toward a point on the path placed a lookahead distance $\Delta > 0$ ahead of the direct projection of the vehicle position on to the path. This behaviour is shown in figure 8.1.

The velocity-path relative angle can also be seen as a saturated proportional controller

$$\chi_r(\mathrm{e}) = \arctan\left(-K_p \mathrm{e}\right) \tag{8.63}$$

where $K_p = 1/\Delta$.

Convergence of the heading χ to the desired heading χ_d is done by treating the heading angle ψ as a disturbance. And transforming the desired course angle χ_d to a desired sideslip angle β_d by using (8.59). Which yields

$$\beta_d = \chi_d - \psi \tag{8.64}$$

A block diagram of the adaptive backstepping controller from sections 8.2 and the speed controller in section 8.3 together with the LOS guidance are shown in figure 8.2. Note that the feed forward calculation of $\dot{\psi}_{d,ff}$ and the variables $\dot{\chi}$, $\dot{\beta}_d$ and $\ddot{\psi}_d$ have been omitted. However, these variables will be described in section 8.5.

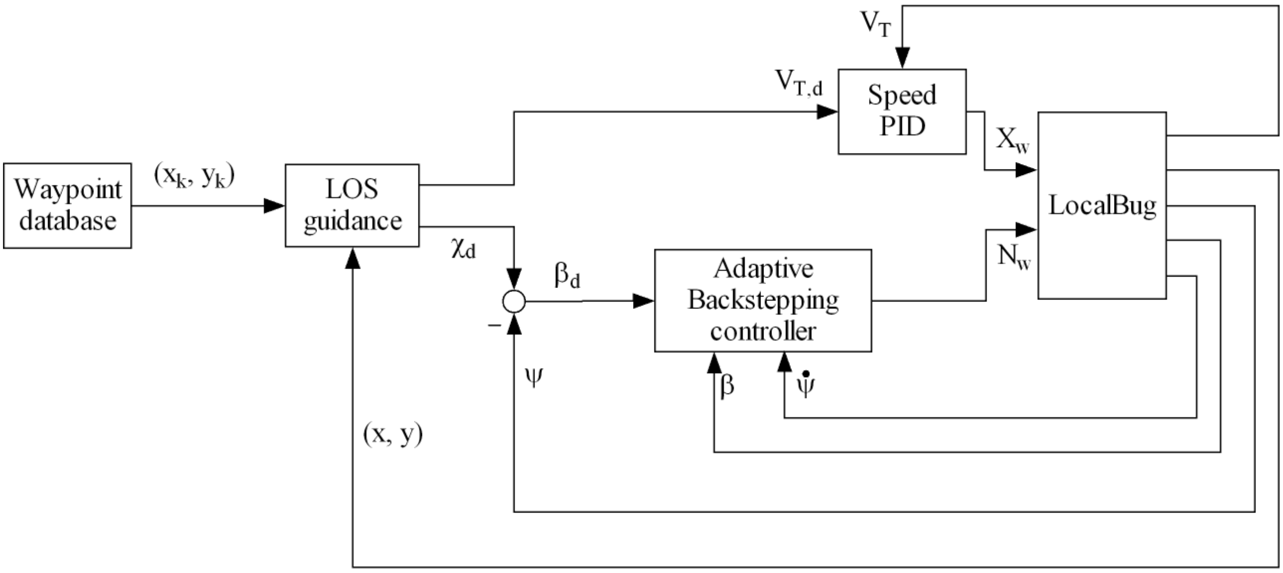

Figure 8.2: LOS guidance and controllers block diagram without feed forward.

If a turn is to be done as fast as possible, it is important to have the largest yaw rate. Therefore a saturation for the desired sideslip angle has been added in the implementation of the LOS guidance. The saturation ensures that the desired sideslip angle does not exceed the steady state drifting condition with the largest yaw rate. See table 7.1 for the largest yaw rates sorted by speed, with corresponding sideslip angles.

8.5 Feed Forward and State Derivatives

The adaptive backstepping controller derived in section 8.2, includes a feed forward term $\dot{\psi}_{d,ff}$. The feed forward term can be found from a lookup table of the steady state yaw rate values $\dot{\psi}_0$, found in section 7.1. Desired sideslip angle β_d and desired speed $V_{T,d}$ should be used as inputs to the lookup table.

Because the lookup table will be used between the steady state values found, an interpolation or mathematical approximation should be done to get the entire range of steady state yaw rates for sideslip angles $-30° \leq \beta \leq 30°$.

The variables $\dot{\chi}$, $\dot{\beta}_d$ and $\ddot{\psi}$ are derivatives needed for the adaptive backstepping controller in section 8.2. The derivative of the course $\dot{\chi}$ can be found by equation (8.5). However, this requires knowledge of the sideslip angle rate $\dot{\beta}$, which are not available. A derivative approximation could be found by backward Euler [23], which yields

$$\dot{a}(t) \approx \frac{a(t) - a(t-T)}{T} \tag{8.65}$$

where a can be any variable, t is the simulation time and T is the step time.

The derivatives for heading rate $\dot{\chi}$ and desired sideslip angle $\dot{\beta}_d$ will be found by using equation (8.65). This approximation should be sent through a reference model to avoid peaks in the derivatives. A second order transfer function will be used in this thesis, which is on the form

$$H(s) = \frac{\omega^2}{s^2 + 2\zeta\omega s + \omega^2} \tag{8.66}$$

where ω is the natural frequency and ζ is the relative damping ratio.

The desired yaw angular acceleration $\ddot{\psi}_d$ could be found from equation (5.31). However, all the wheel forces and inputs are required for this calculation. For simplicity, the yaw angular acceleration will be calculated using equation (8.65).

8.6 Simulink Implementation

The controllers and guidance system described this chapter were implemented in Simulink. They were used to control the simulator described in chapter 5.1, which was implemented in [5]. See figure 8.3 and 8.4 for Simulink screenshots of the controller and guidance respectively.

In figure 8.3 the saturation of the steering angle δ and the throttle input u_a in blocks labelled $max\ 30deg$ and $max\ 25v$ respectively. Where the steering angle is forced to be between ±30 deg and the throttle input between 0 and 25 V.

During implementation, the desired sideslip angle β_d was saturated with an upper limit associated to the equilibrium point with the largest yaw rate. An overview of the maximum

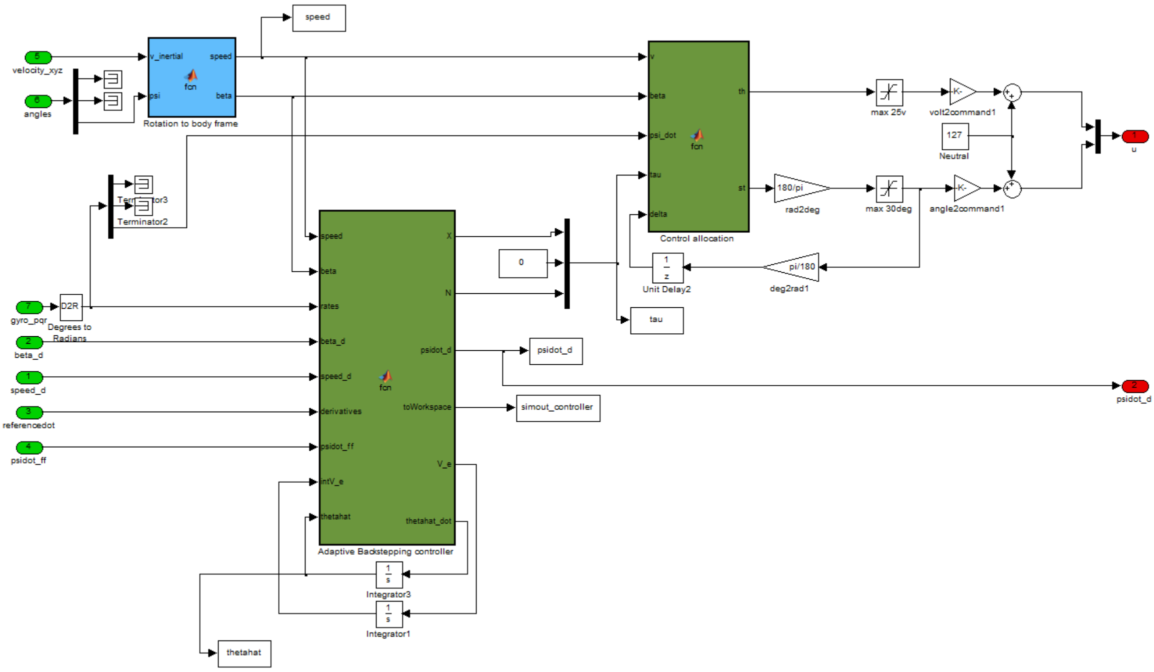

Figure 8.3: Screenshot of Simulink controller block.

yaw rates with related sideslip angles, for different speeds are shown in table 7.1.

In figure 8.4, the derivative approximations are calculated and filtered to avoid peaks. The filter in equation (8.66) was used for filtering the derivatives of the desired sideslip angle $\dot{\beta}_d$, course angle $\dot{\chi}$ and desired course angle $\dot{\chi}_d$. The filter parameters were chosen as

$$\omega = 10 \text{ rad/s} \tag{8.67}$$

$$\zeta = 1 \tag{8.68}$$

This gives a critically damped second order filter with natural frequency of 10 rad/s. However, for the derivative of the desired yaw rate $\ddot{\psi}_d$ a moving average was chosen because the filter caused the controller to oscillate severely. This is due to the phase lag of 180 deg introduced by the filter, making the controller unstable.

The moving average works as follows

$$\hat{b}(t) = \frac{b(t) + b(t-1) + \cdots + b(t-n)}{n+1} \tag{8.69}$$

where b can be any variable, the output $\hat{b}(t)$ is the current value, the time is the variable t and n is the number of samples before the current sample used in the average. In the implementation, n = 3 giving

$$\hat{\ddot{\psi}}_d(t) = \frac{\ddot{\psi}_d(t) + \ddot{\psi}_d(t-1) + \ddot{\psi}_d(t-2) + \ddot{\psi}_d(t-3)}{4} \tag{8.70}$$

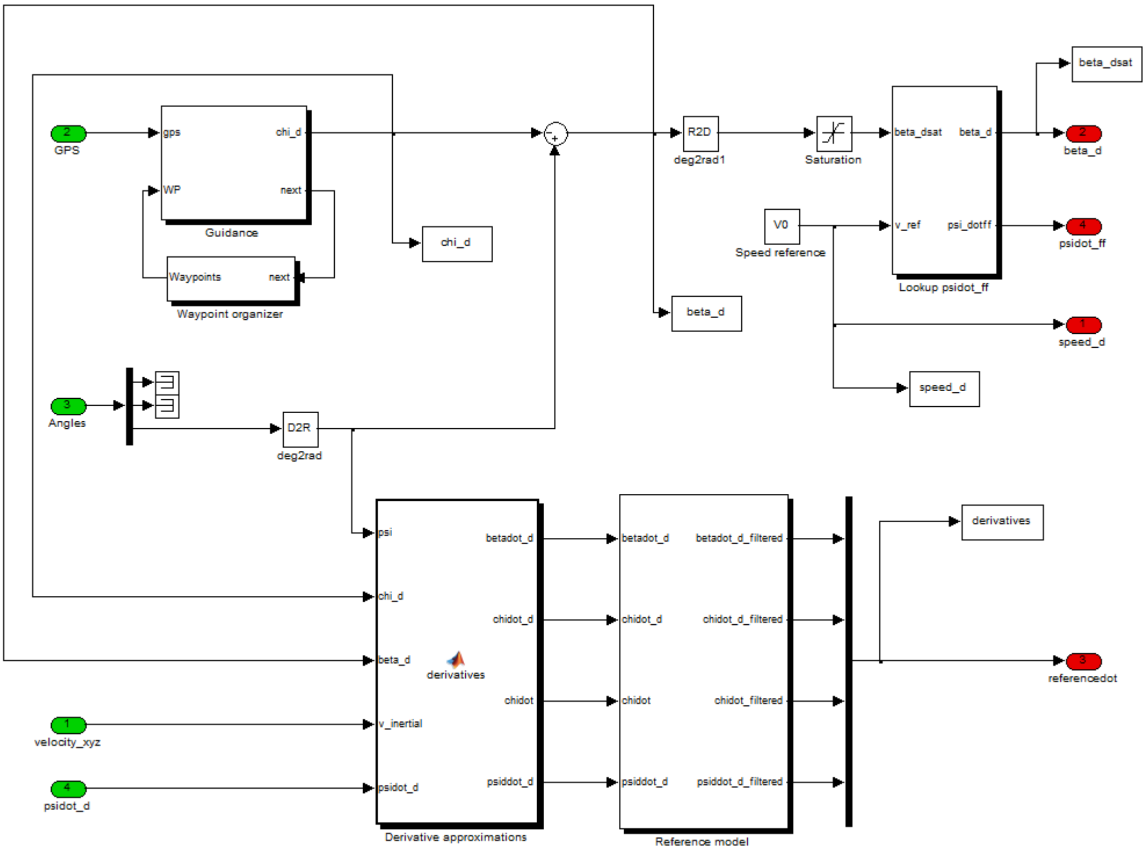

Figure 8.4: Screenshot of Simulink guidance block.

A moving average has a shorter phase lag than a second order filter and therefore does not cause oscillations in the controller.

9 Simulation Results

Four test cases have been used to check how well the controller achieves the desired yaw rate ψ_d and sideslip angle β_d. All the cases will be performed with friction corresponding to that of wet cobblestones, and they are as follows

Case 1: Controller response to a steps in desired sideslip angle, at the same desired speed.

Case 2: Tracking of a sinus reference in desired sideslip angle, with amplitude of 30 deg.

Case 3: Inspecting how model parameter uncertainty affects the controller.

Case 4: Comparison between a baseline PID controller and the adaptive backstepping controller.

The controller gains used for the simulation were for the adaptive backstepping controller

$$k_1 = 7 \tag{9.1}$$

$$k_2 = 300 \tag{9.2}$$

$$p = 41 \tag{9.3}$$

and the speed controller

$$k_p = 100 \tag{9.4}$$

$$k_i = 100 \tag{9.5}$$

Notice the adaptive backstepping controller has a larger gain k_2 compared to the speed controller. This is done to satisfy equation (5.78), which means that the yaw moment N_w from the controller will dominate the thrust X_w to achieve Power Over drifting.

9.1 Case 1: Step Responses

Step responses in desired sideslip angle were preformed to three equilibrium points at the same desired speed $V_{T,d}$ = 3 m/s. These three step responses were simulated with steps in desired sideslip angle β_d of 10 deg, 20 deg and 30 deg. The steps were initiated at time t = 5 seconds.

Figure 9.1 shows a comparison of the different paths taken during drifting. It also shows that the drifting condition with the largest yaw rate is at sideslip angle β of 10 deg. This is supported by the vehicle states shown in figure 9.2. With the convergence to the desired sideslip angle β_d and the desired yaw rate $\dot{\psi}_d$, the first two error states in figure 9.3 converge to zero and the disturbance estimate $\hat{\theta}$ converges to a constant value. When the sideslip angle converges, the behaviour is underdamped with the normalized overshoot with respect to desired sideslip angle increasing with decreasing desired sideslip angle. The lowest step in the test was to desired sideslip angle equal to 10 deg, and here the overshoot was 28% of the desired sideslip angle, which is a significant overshoot. This overshoot can be attributed to the aggressive adaptive backstepping controller.

From figure 9.2, it is shown that when the drift is initiated the vehicle speed increases. This affect is due to the drifting controller giving a large yaw moment that effectively dominates the speed controller when drift is being initialised, see figure 9.4. According to [19], a drifting technique called Power Over Drift uses throttle to get the rear tires to slip, just as the backstepping controller does in this thesis. The oscillations caused by this behaviour only has an amplitude of about 5% of the desired speed. An initial reduction in speed is due to motor current $i_a = 0$ at start of simulation.

For desired sideslip angle equal to 10 deg, the steering angle δ in figure 9.4, only hits the lower saturation. However, for other two cases the steering angle is saturated both at the upper and the lower limit with increasing oscillations with increase desired sideslip angle. The constant steering angle after drifting is achieved is about zero for desired sideslip angle of 10 deg, 12 deg with desired sideslip angle of 20 deg and 23 deg steering angle for desired sideslip angle of 30 deg.

To see that the controller actually converges to the desired sideslip angle, a longer time series with step in desired sideslip angle to 10 deg, shown in figure 9.5. The integral action from the parameter adaptation causes convergence to the desired sideslip angle, albeit slowly.

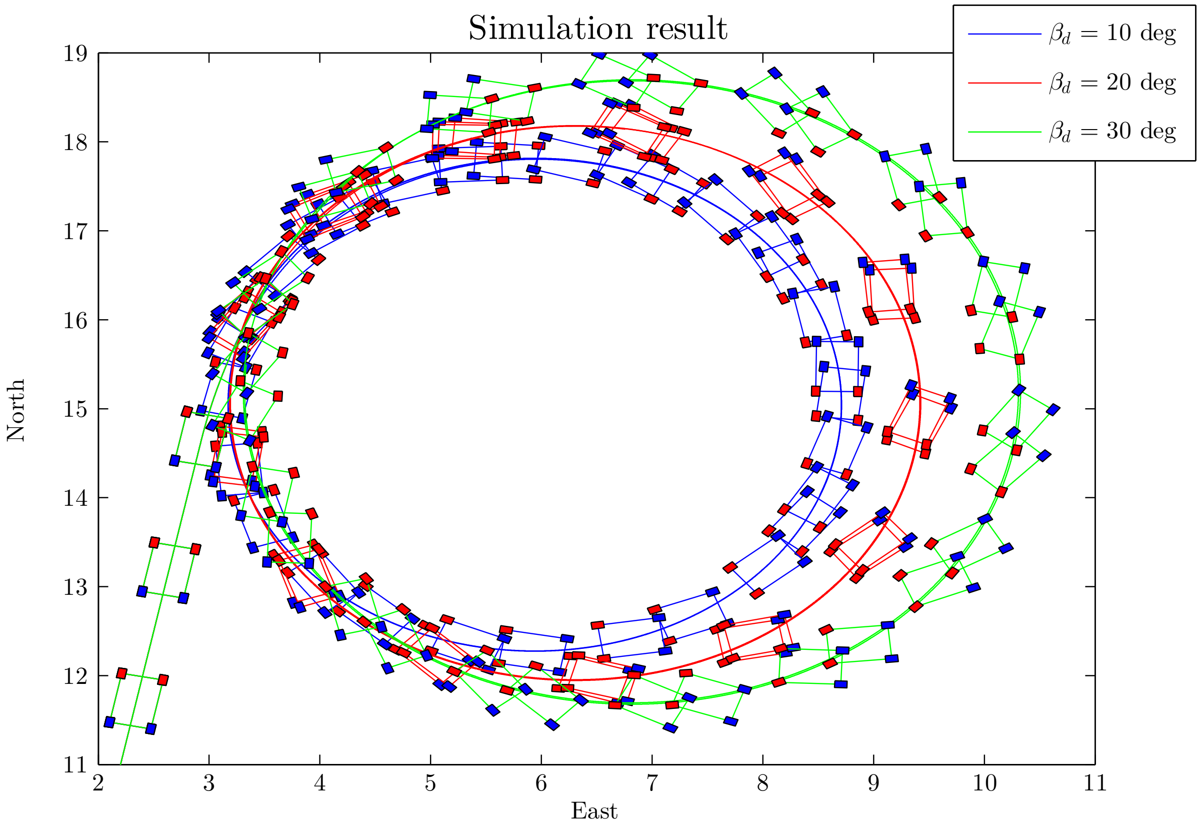

Figure 9.1: Simulation results for steps in desired sideslip angle of 10 deg, 20 deg and 30 deg. The front wheels are red.

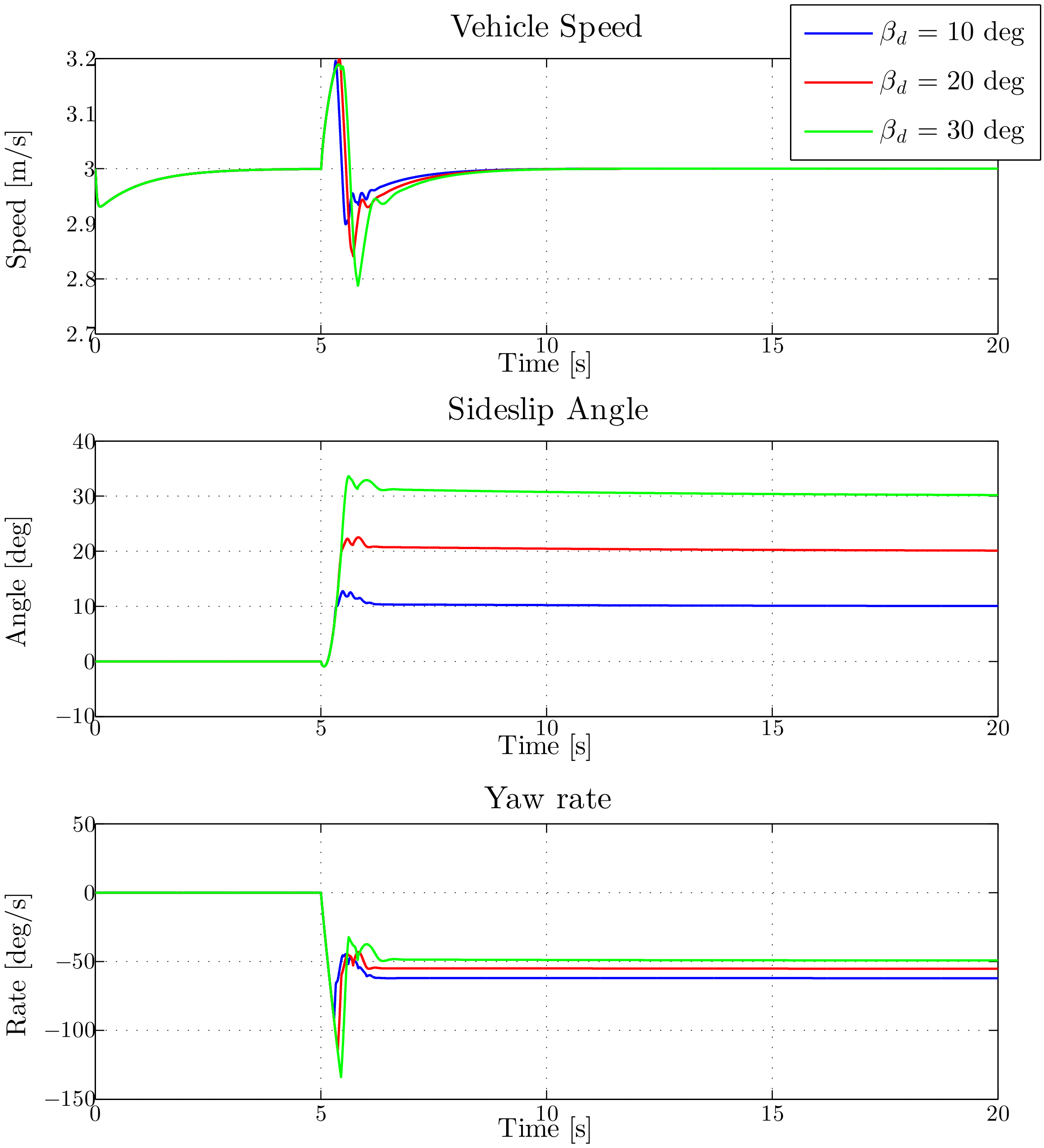

Figure 9.2: Vehicle states during for steps in desired sideslip angle. The desired sideslip angle is achieved for all three steps.

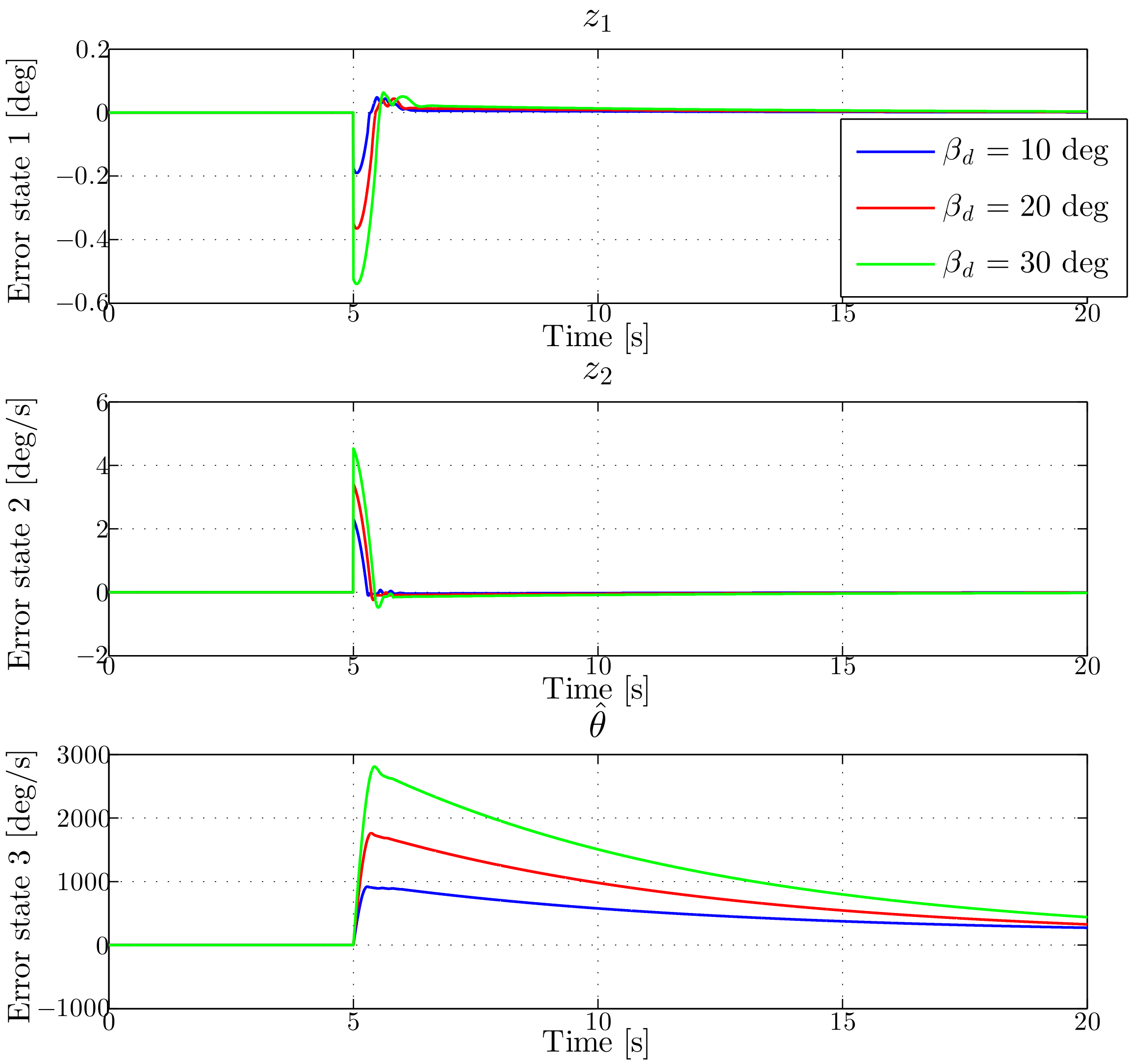

Figure 9.3: Error states in the adaptive backstepping controller. The first two error states go to zero, and the third converges to a constant value.

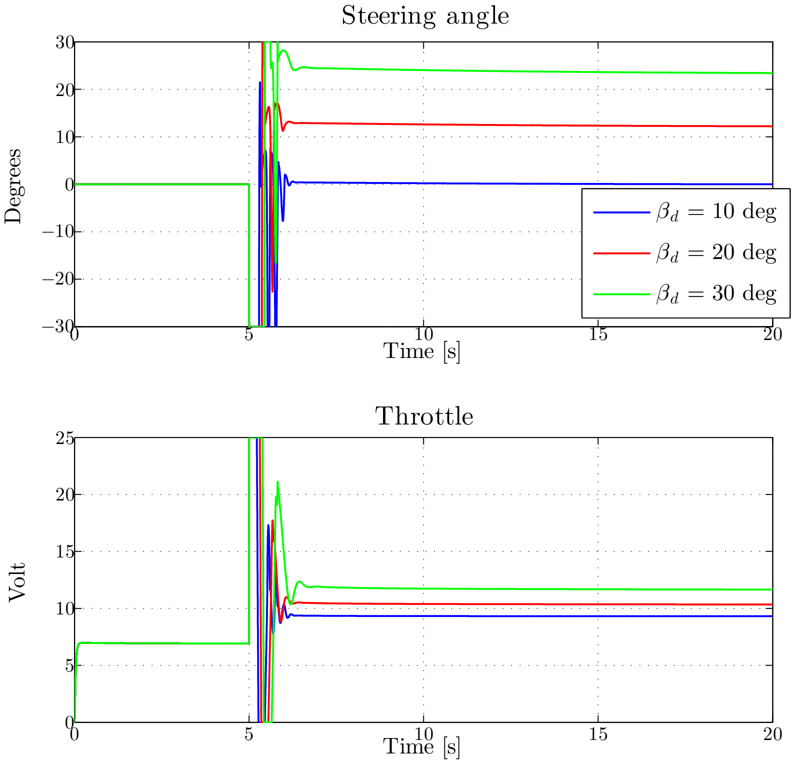

Figure 9.4: Plot of control inputs during steps in the desired sideslip angle.

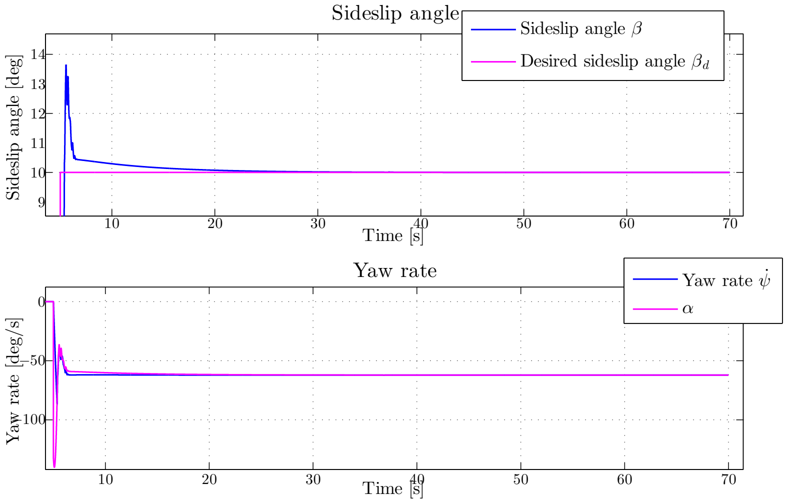

Figure 9.5: Convergence to the desired sideslip angle and yaw rate it shown. The integral action works slowly, however convergence is achieved.

9.2 Case 2: Following a Sinusoidal Reference

A sinusoidal signal is used for the desired sideslip angle β_d, with an amplitude of 30 deg and a frequency of 0.5 rad/s. The desired speed $V_{T,d}$ = 3 m/s during the simulation.

The yaw rate $\dot{\psi}$ is the only state that converges to the desired value during simulation, from figure 9.6. And oscillations in the speed with an amplitude of 5% of the desired speed can also be seen in this figure. When the desired sideslip angle increases, the sideslip angle β does not converge until the desired sideslip angle peaks at 30 deg. And the same behaviour can be seen for decreasing desired sideslip angle, where convergence is achieved at desired sideslip angle of -30 deg. All the states oscillate when the sideslip angle changes polarity, when drifting in the opposite direction needs to be established.

The error states z_1 and z_2 in figure 9.7 reflect the behaviour described in the previous paragraph. Where z_1 does not converge to zero, but z_2 is zero most of the time. When the desired slideslip angle crosses zero, oscillations appear in all the error states. These oscillations happen because the vehicle need to transition between a right handed turn and a left handed turn and vice versa. This transition can clearly be seen in the control inputs in figure 9.8, where drifting initialisation and countersteering to compensate need to be done for every zero crossing of the desired sideslip angle. Both control inputs oscillate and hit their upper and lower constraint.

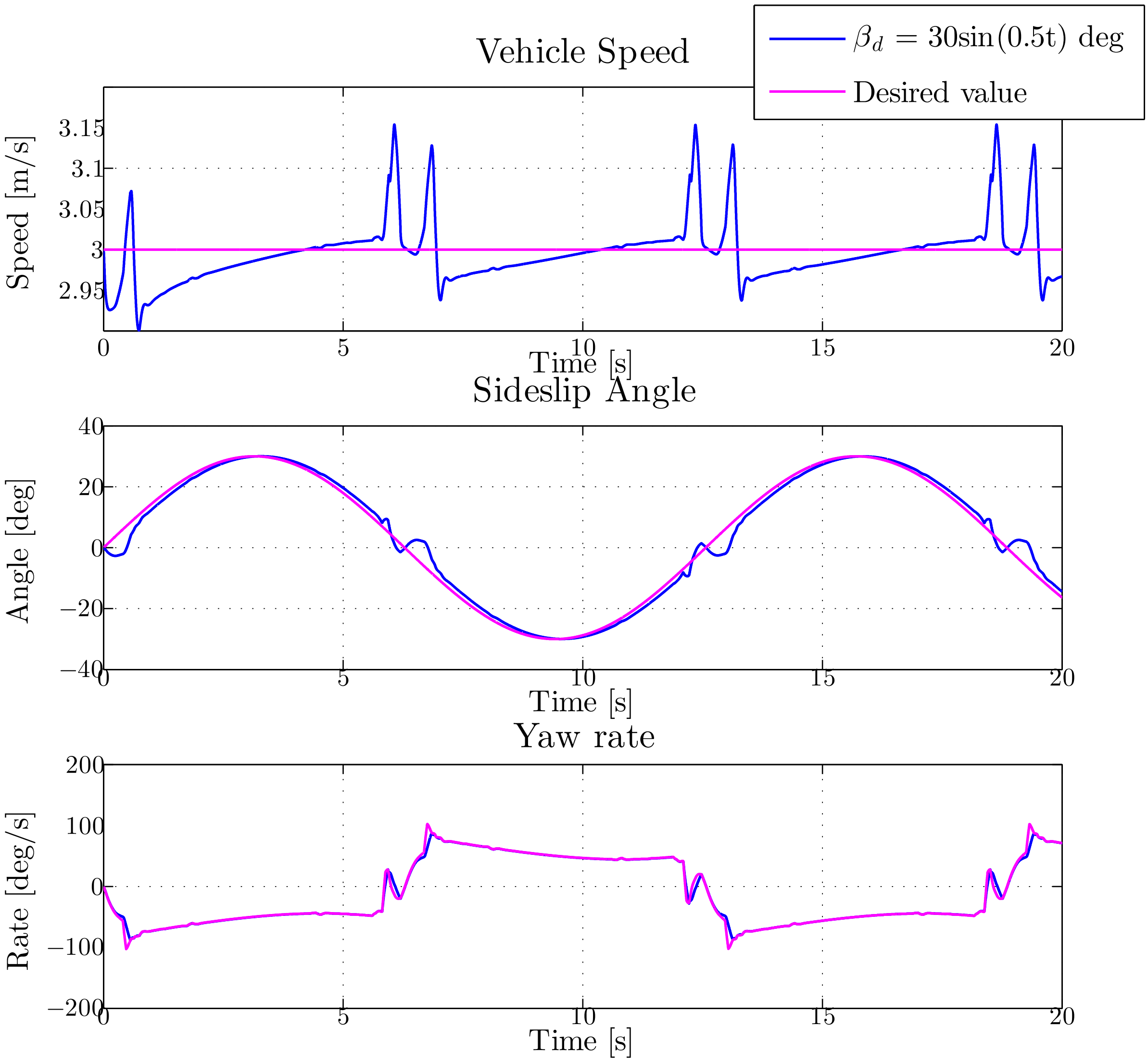

Figure 9.6: Vehicle states with sinusoidal sideslip angle reference. The sideslip angle follows the reference with some lag.

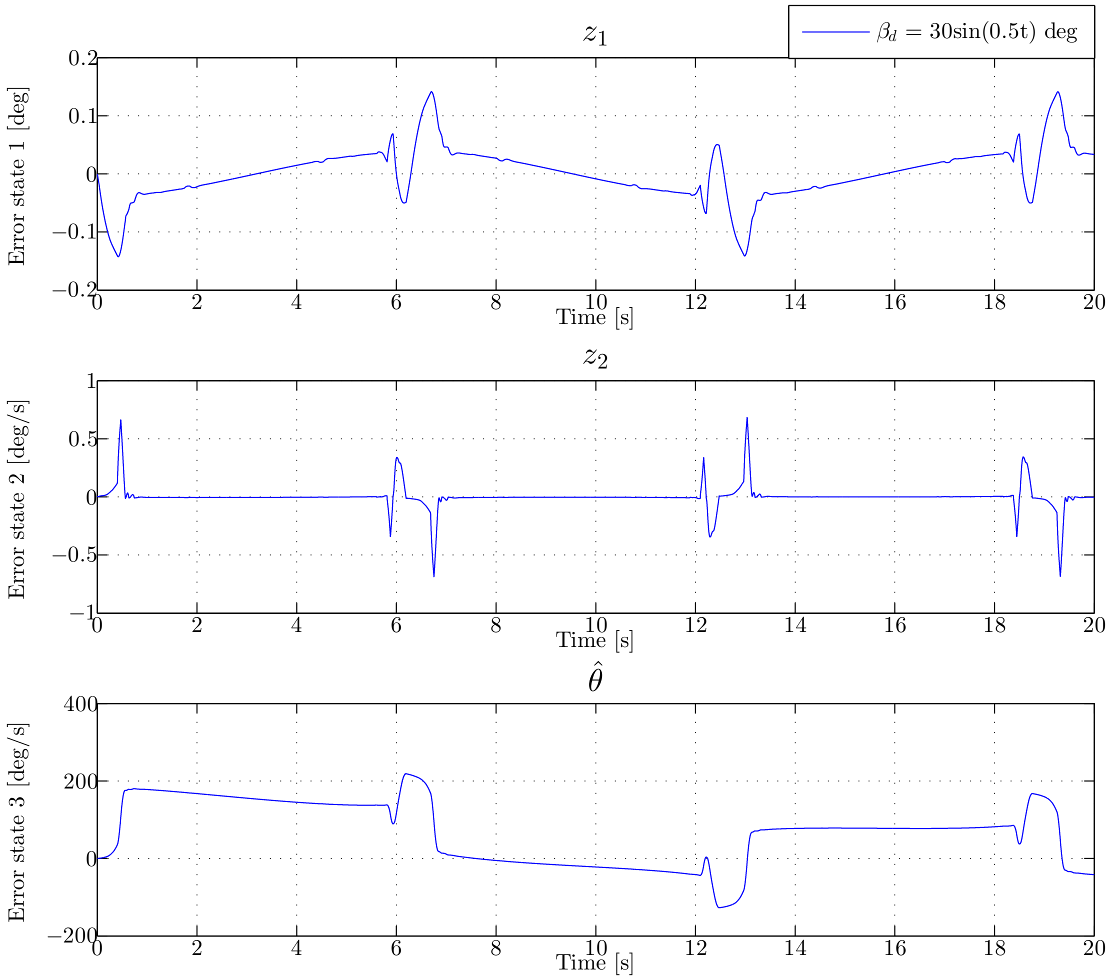

Figure 9.7: Error states with sinusoidal sideslip angle reference. The second error state z_2 converges to zero. However, z_1 does not converge fast enough and fails to reach zero. The third state nears constant values on two occasions.

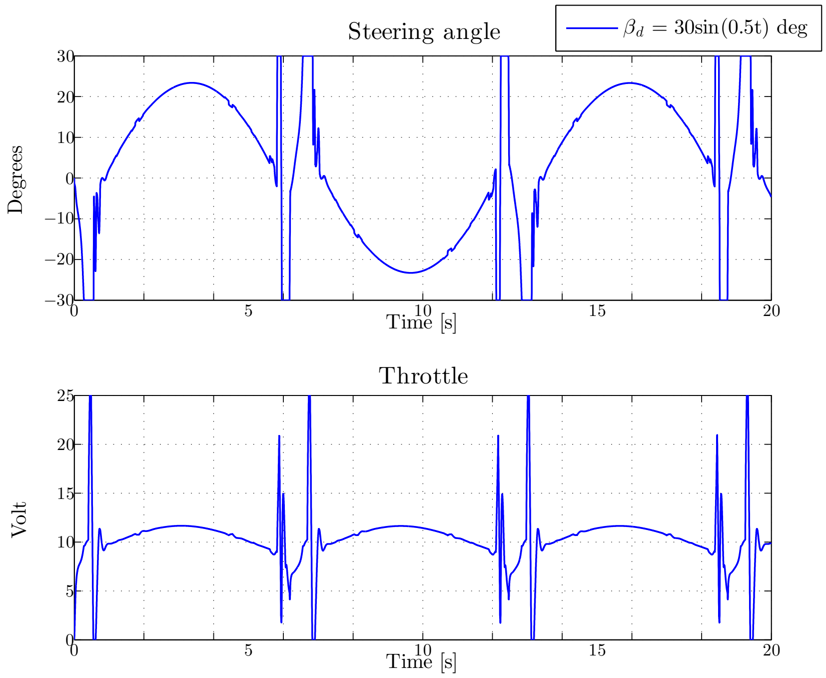

Figure 9.8: Inputs to the system for sinusoidal sideslip angle reference. Note that both inputs oscillate with given intervals during polarity change of the sideslip angle.

9.3 Case 3: Parameter Uncertainty

To inspect the robustness of the controller, the mass was changed by ±30% and compared to a simulation with the mass unchanged. A step in desired sideslip angle β_d of 10 deg at time $t = 5$ seconds, with desired speed $V_{T,d} = 3$ m/s was used for this case.

In figure 9.9 the path taken during the three simulations can be seen. The three tests converge to the same size drifting circle, however the controller converges faster with increased mass. This convergence speed change causes the paths to be moved along the line of entry to the drifting circle. The increase in mass causes the speed control to have reduced effect on the system, and thus the speed oscillations are reduced, see figure 9.10. When the speed oscillations are reduced, the turn becomes less aggressive resulting in reduced strain on the steering angle controller, shown in figure 9.12. All vehicle states converge to the same values, even though they take different routes.

The error states z_1 and z_2 converge faster with increased mass, from figure 9.11. Therefore it is to be expected that the disturbance estimate $\hat{\theta}$ peak decreases with increased mass, because $\hat{\theta}$ is the integral of z_2 times a constant.

In figure 9.13 the path taken with variations of ±30% of inertia is shown. And the vehicle states, error states and control inputs for this case are shown in figure 9.14, 9.15 and 9.16 respectively. Not surprisingly, the drifting is established faster with decreasing inertia. While comparing the change in mass and inertia, it is evident that the controllers are less sensitive to an increase of 30% of the inertia than an increase of 30% in mass. This means that if the vehicle is loaded with more equipment and the inertia and mass are both increase 30%, the vehicle will converge faster.

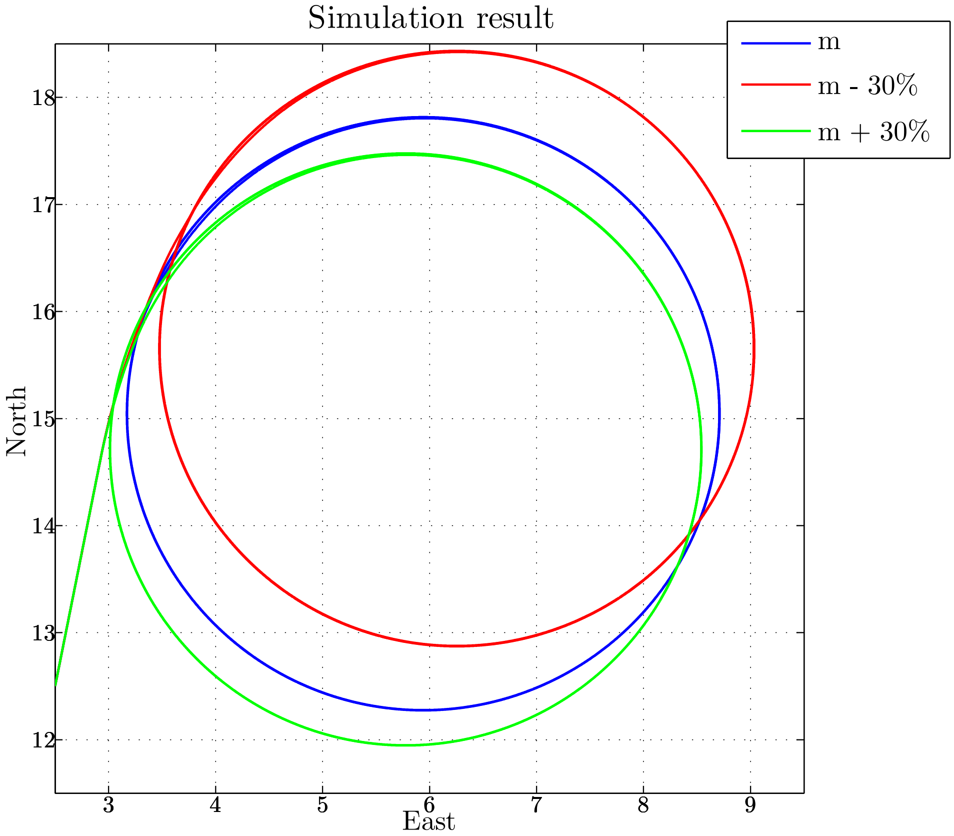

Figure 9.9: Simulation results for backstepping controller with errors in the vehicle mass. Reduced mass makes the convergence slower and the opposite effect is observed for increased mass. To reduce cluttering in this plot, the vehicle outline has been removed.

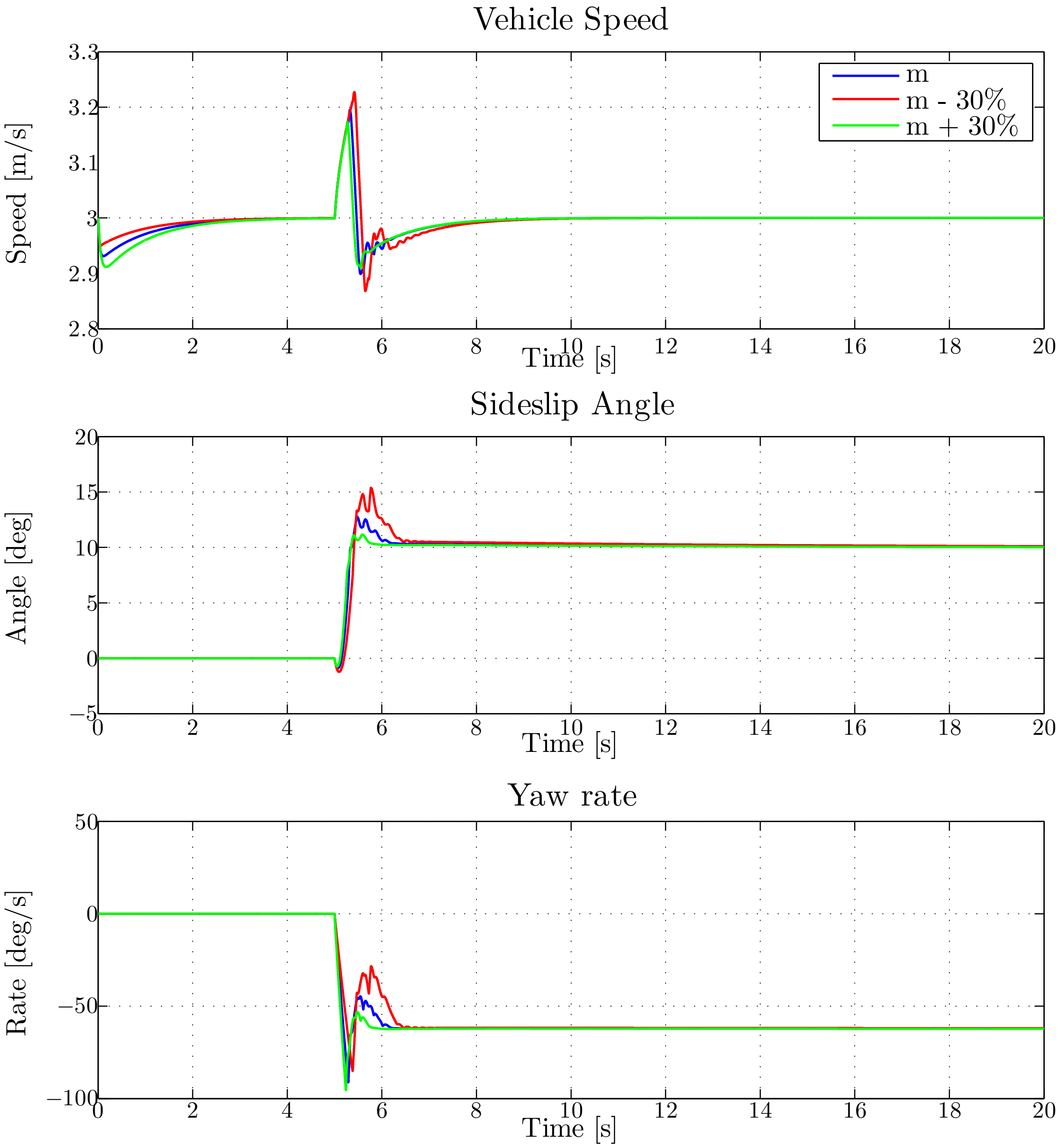

Figure 9.10: Vehicle states for errors in the vehicle mass. Notice the increased convergence speed with increased mass.

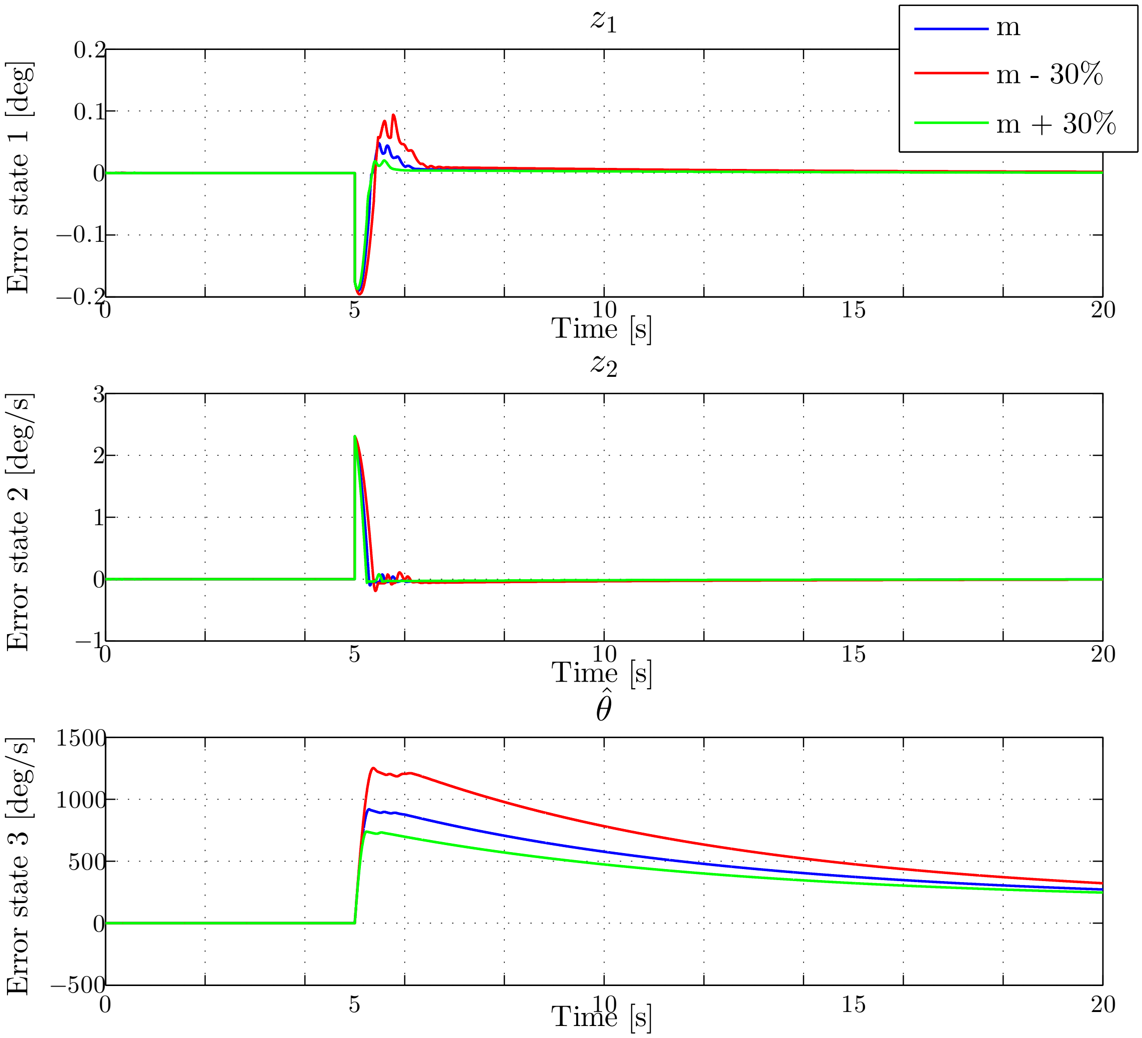

Figure 9.11: Error states for vehicle mass variations. The convergence is increased with increased mass.

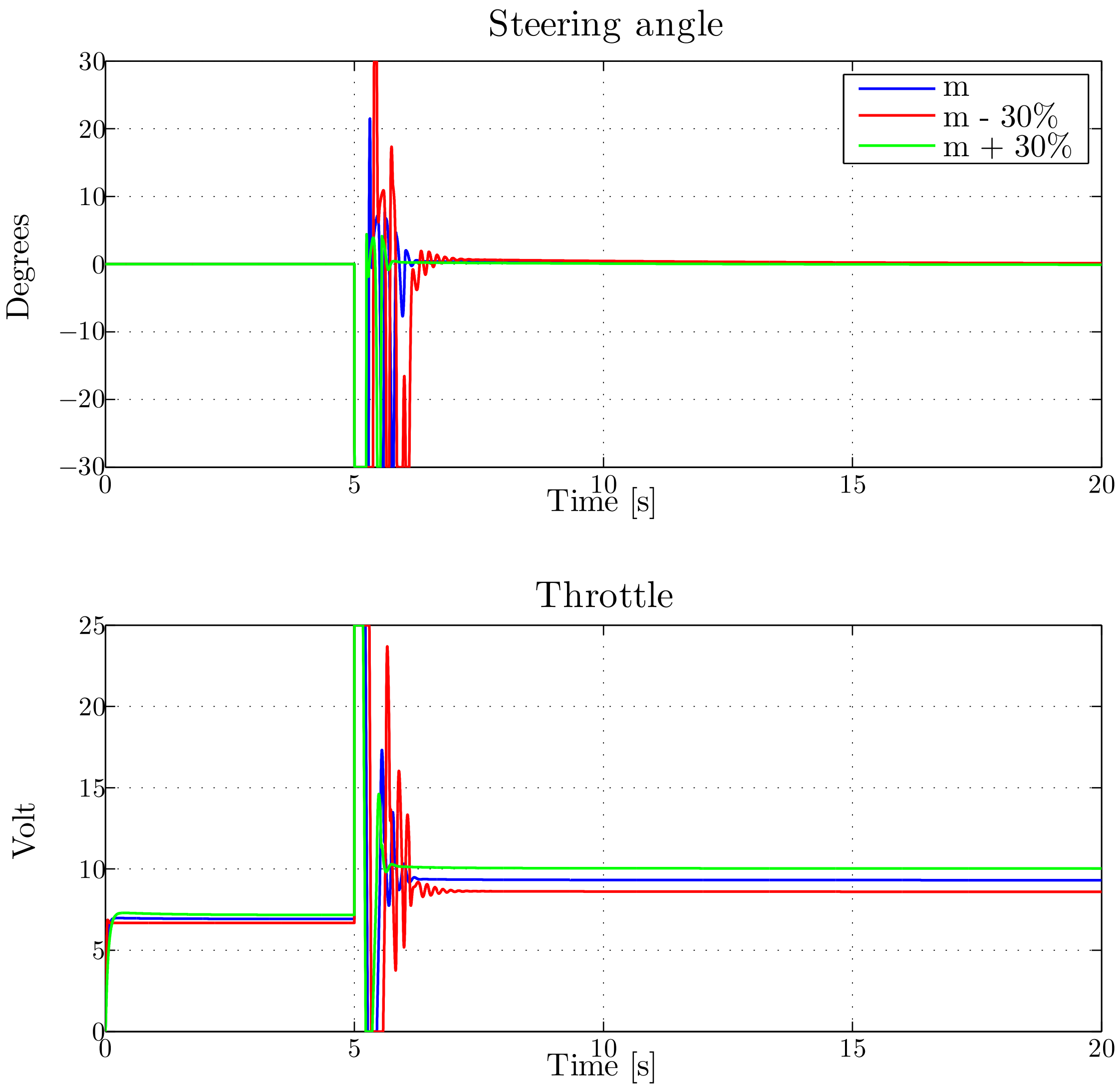

Figure 9.12: Vehicle inputs with errors in the vehicle mass. The strain on the steering and speed controllers are reduction and increased respectively, with increased mass.

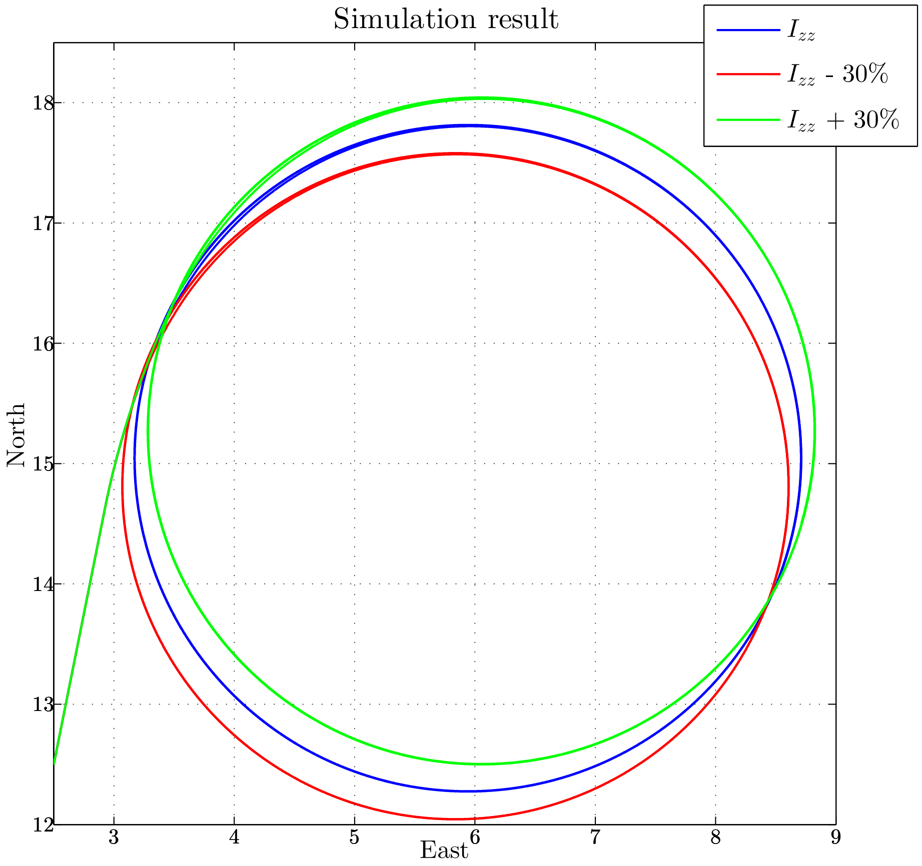

Figure 9.13: Simulation results for backstepping controller with errors in the vehicle inertia. Reduced inertia makes the convergence faster and the opposite effect is observed for increased inertia. To reduce cluttering in this plot, the vehicle outline has been removed.

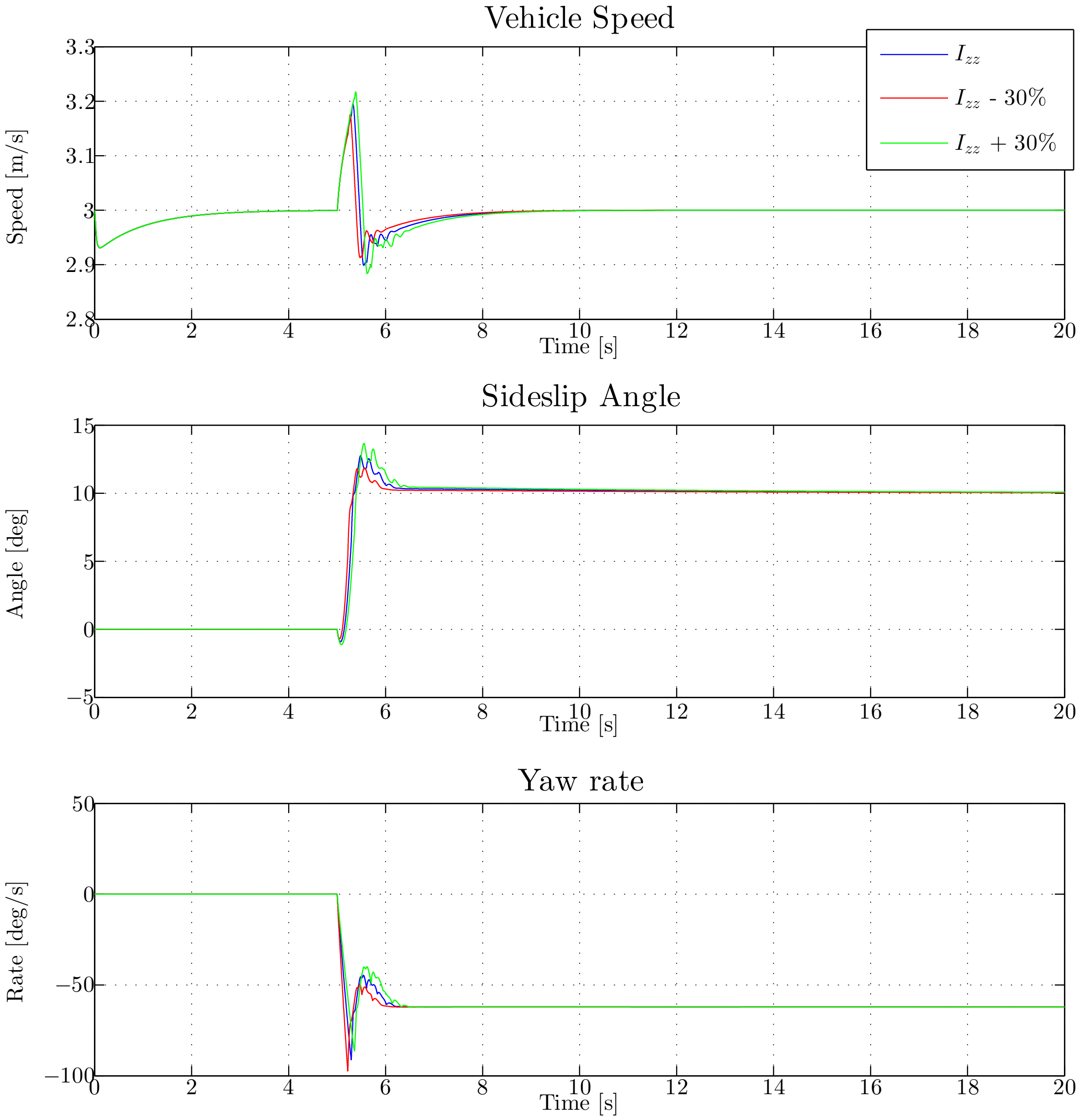

Figure 9.14: Vehicle states for errors in the vehicle inertia. Notice the increased convergence speed with decreased inertia.

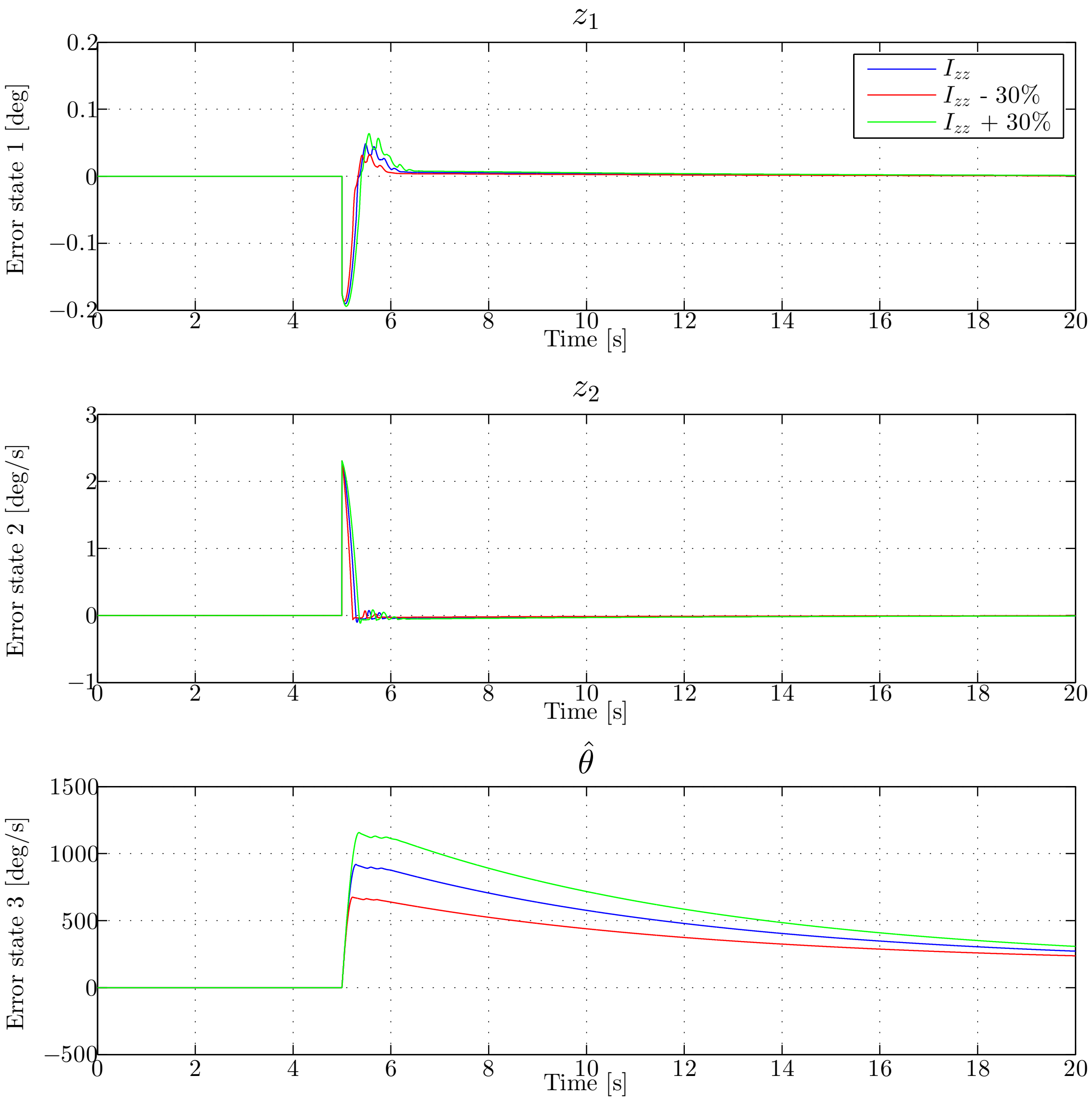

Figure 9.15: Error states for vehicle inertia variations. The convergence speed is increased with decreased inertia.

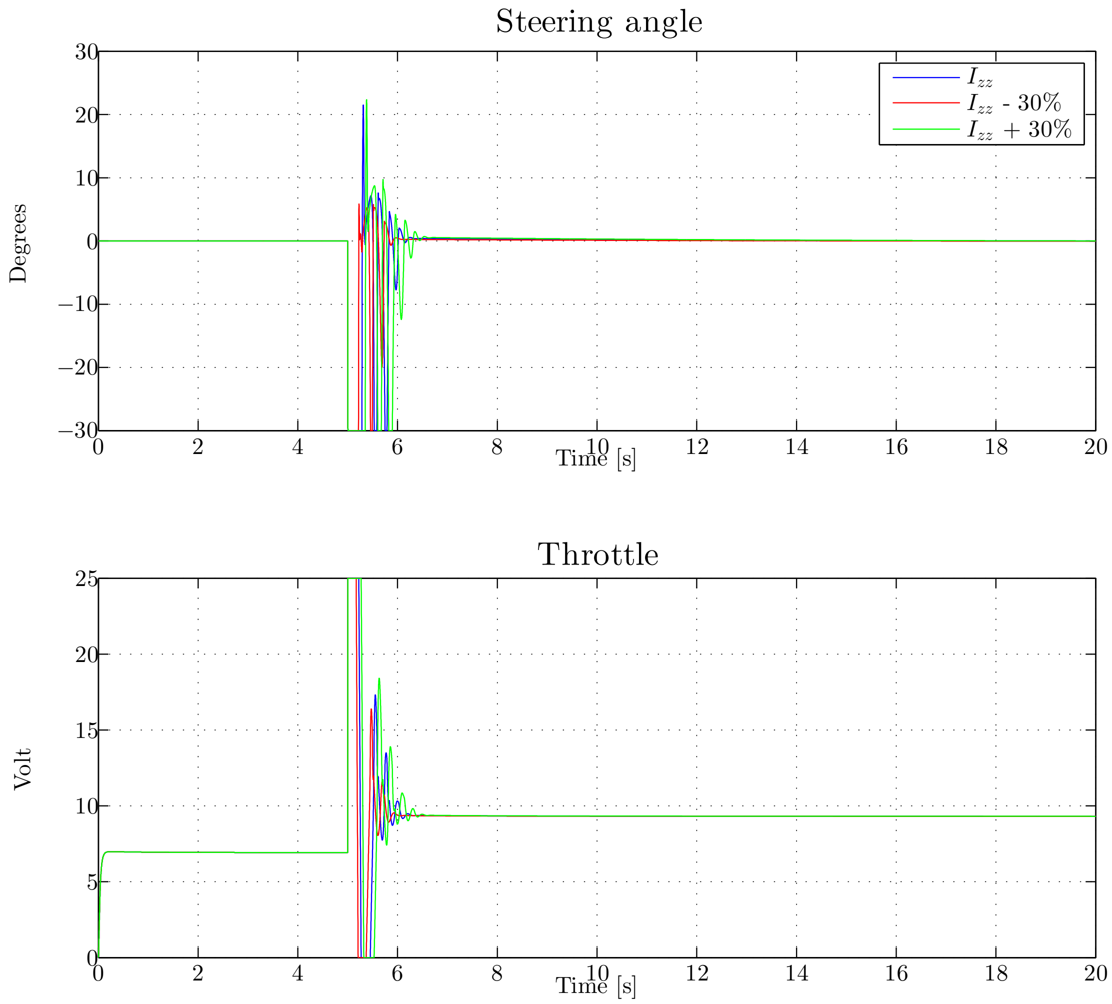

Figure 9.16: Vehicle inputs with errors in the vehicle inertia. The strain on the steering and speed controllers are reduction and increased respectively, with decreased inertia.

9.4 Case 4: Comparison with PID Controller

A baseline PID controller described in section 8.3 will be used for comparison for this final test. This test is done to highlight the strong points of the adaptive backstepping controller compared to conventional cornering. The desired sideslip angle β_d is supplied from a LOS guidance system described in section 8.4, while the desired speed $V_{T,d}$ = 3 m/s during the test. A figure eight is the chosen path, with two hairpin turns of 203 deg connected with two 30 meter straight sections.

The adaptive backstepping controller clearly completes the figure eight faster than the PID controller, see figure 9.17. Half way through the lap, the backstepping controller has a lead of five car lengths. It is evident that the backstepping controller makes a much tighter corner compared to the PID controller, which can be seen from figure 9.17, and more clearly from 9.18. Also notice that with conventional steering with the PID controller, a much larger turning circle is performed, which makes the vehicle run off the road.

The speed of the drifting controller oscillates seven times higher than with the PID, from figure 9.19. Which is due to the more aggressive yaw moment that dominate the speed controller while the drift is initialized, see figure 9.21. During the hairpin turn, drifting is achieved with the backstepping controller with a maximum sideslip angle β of -12.5 deg. While the PID controller converges to a sideslip angle of 2 deg, which corresponds to conventional cornering, where the yaw rate $\dot{\psi}$ and sideslip angle β have the same sign. The yaw rate is larger for the backstepping controller, with a peak of 90 deg/s, and convergence to 62 deg/s. When the cornering is performed with the PID, it only achieves 43 deg/s, and therefore more time is used to complete the turn.

Error states for the backstepping controller are shown in figure 9.20. Fast convergence in error states z_1 and z_2, when they are far from zero. However, convergence slows down closer to zero due to slow integral action. Because z_2 converges fast when far from zero, $\hat{\theta}$ converges slowly.

Both the throttle and the steering angle are much more aggressively controlled by the backstepping controller, shown in figure 9.21. The PID controller increases the steering angle to saturation and there it stays until the corner is completed, which corresponds to normal vehicle driving behaviour. Yaw moment applied from the PID controller is much smaller than the drifting controller, such that the throttle will be less affected. Peaks in the throttle setting for the PID can be seen when the turn is started, while they are dwarfed by the oscillations in the throttle setting for the drifting controller.

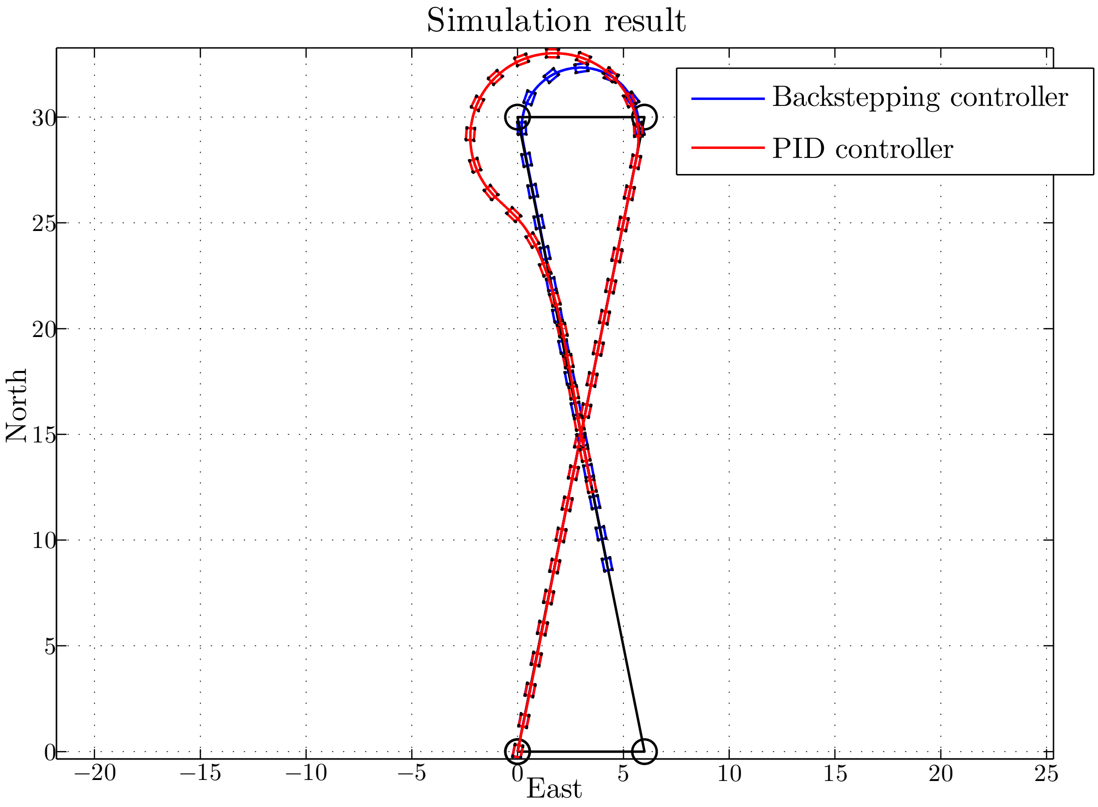

Figure 9.17: Simulation results for backstepping controller and PID controller with LOS guidance. The backstepping controller completes the lap faster than the PID.

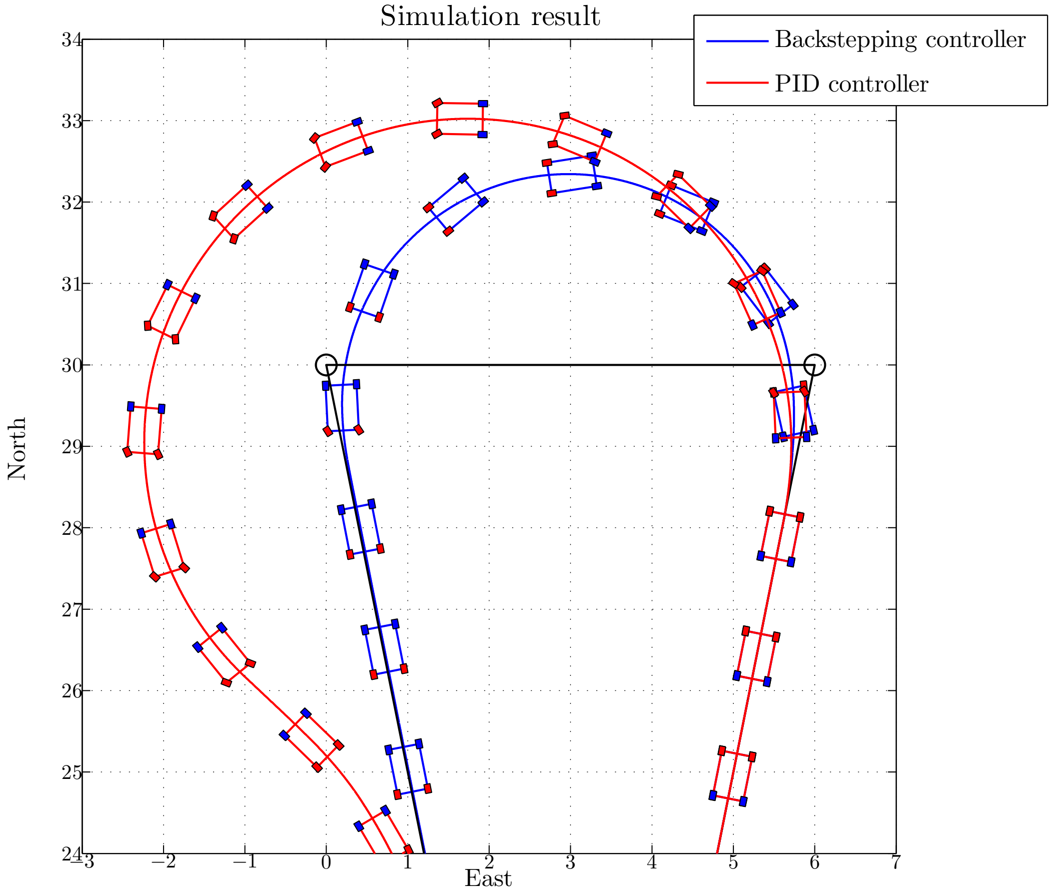

Figure 9.18: Zoomed figure of the cornering comparison between backstepping controller and PID controller. Notice that the backstepping controller makes a much tighter corner compared to the PID. The front wheels are red.

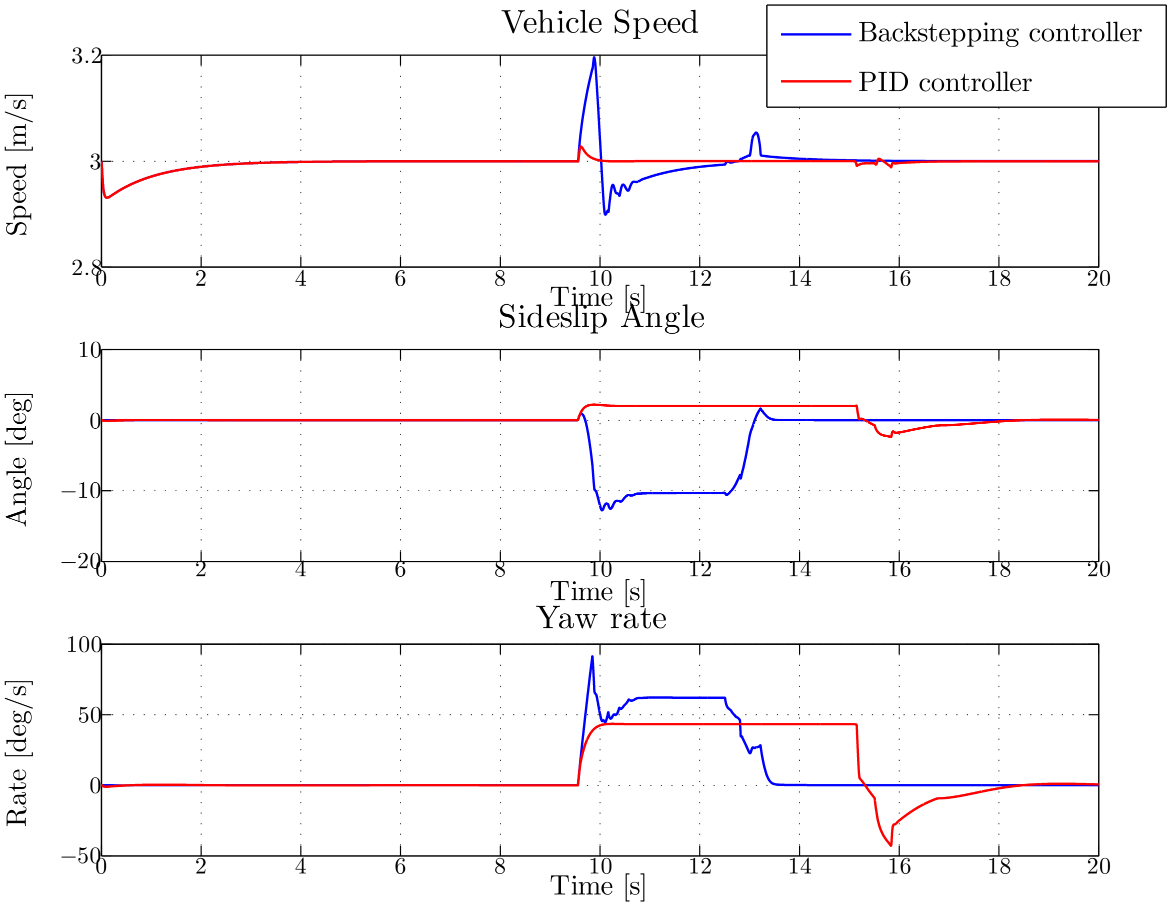

Figure 9.19: Comparison between the vehicle states with drifting and conventional cornering. The behaviour of the drifting controller is more aggressive.

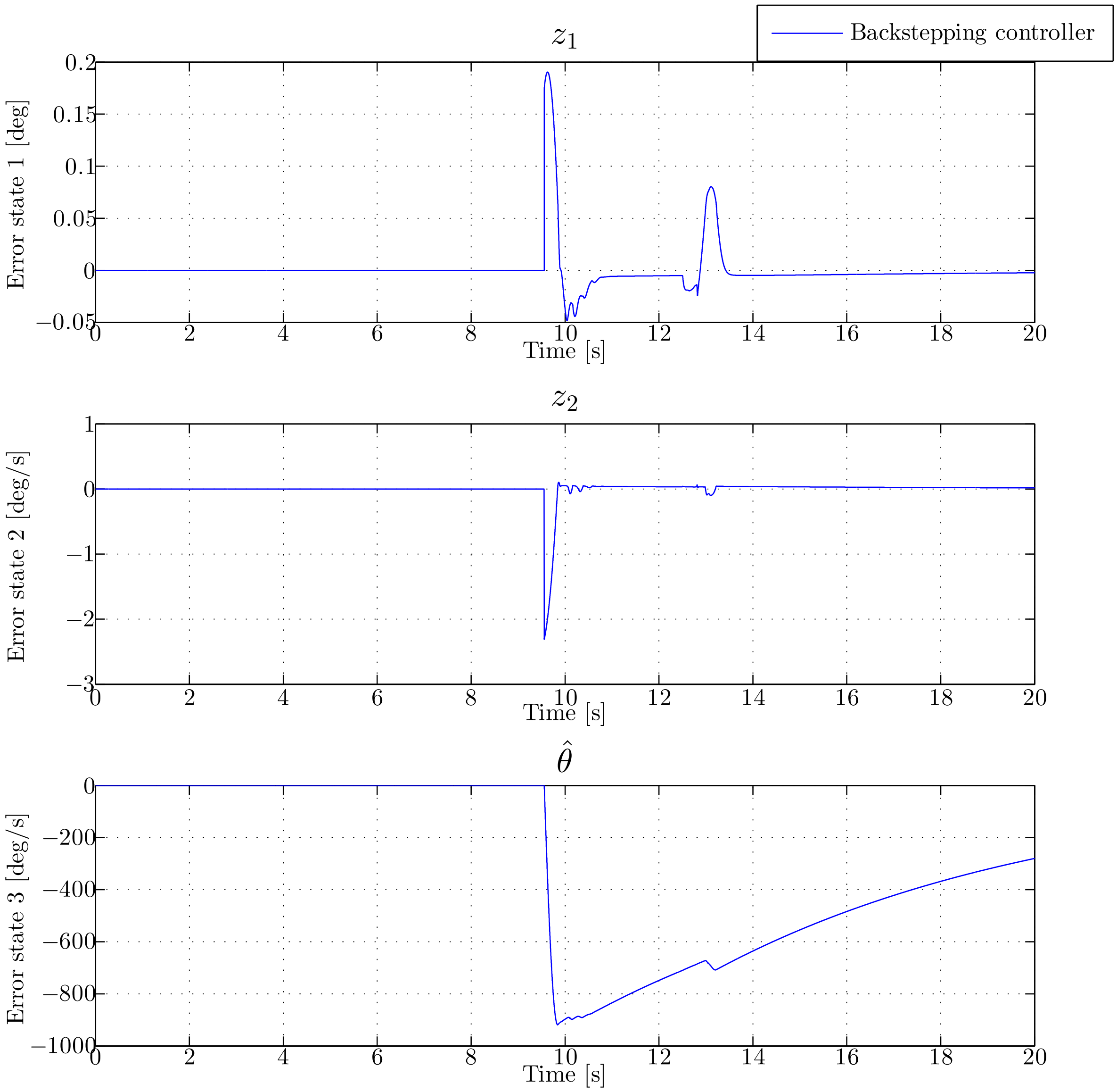

Figure 9.20: Error states for the backstepping controller. Fast convergence in z_2 causes slow convergence in the error estimate $\hat{\theta}$.

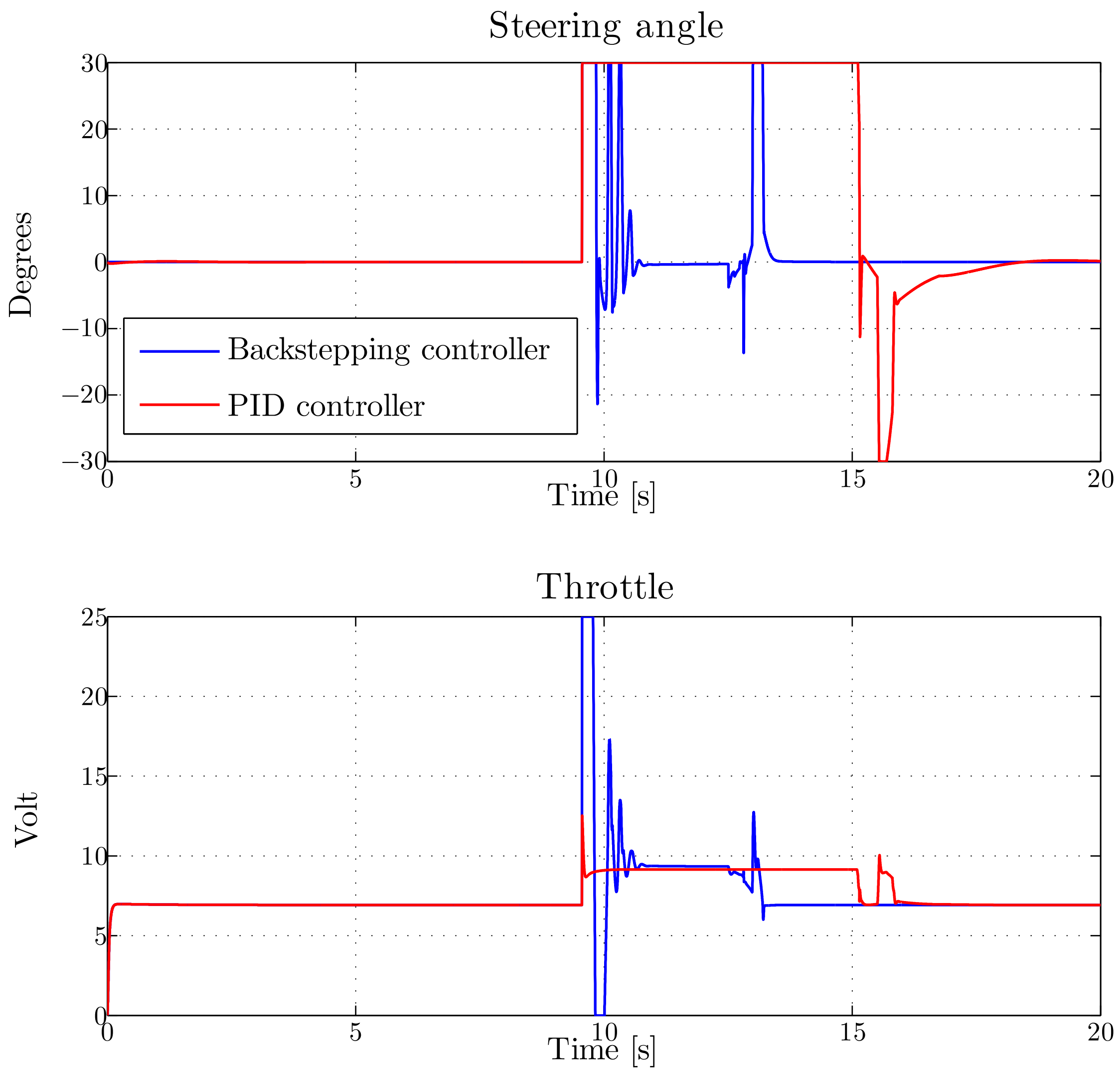

Figure 9.21: Control inputs for the backstepping controller and the PID controller. Notice that the backstepping controller is much more aggressive.

10 Discussion

The controller can converge to and maintain a desired sideslip angle β_d within the range -30 deg to 30 deg, which can be seen from the simulation results. Drifting is achieved by the adaptive backstepping controller dominating the speed controller and applying max motor throttle when the drift is being initiated, which corresponds to a drifting technique called Power Over.

Steps in the desired sideslip angle causes an underdamped response in sideslip angle, with decreasing overshoot with increased desired sideslip angle. The integral action provided by the disturbance estimate in the adaptive backstepping controller makes the controller converge to the desired sideslip angle, albeit slowly. Slow convergence when close to the desired state is acceptable, because the initialisation of the drift is the crucial part. Here the convergence is much faster and sideslip angle crosses the desired sideslip angle for the first time within 0.6 seconds of the step.

In the second test case, the vehicle tracks the sinusoidal reference during the entire range of sideslip angles between -30 deg and 30 deg. The slow convergence of the sideslip angle makes it lag behind the reference. However, the yaw rate error is close to zero whenever drifting is not being initiated. Sign change of desired sideslip angle causes severe oscillations in the control inputs and could cause wear and tear of actuators if tested in practice.

Because the speed controller is being dominated when drifting is being initiated, the speed oscillates and only maintains constant desired speed whenever the adaptive backstepping controller has reached its control objective. This is desirable because the vehicle drifting is the main purpose of this thesis, and the speed oscillations are only below 6% of the desired speed.

With errors in the mass parameter in third test case, the vehicle still converges to the same drifting equilibrium. The only change seen from this test was that the convergence speed to the desired sideslip angle increased with increased mass. Because the techniques used to drift in this thesis is the Power Over which uses power to get the rear tires to slip, this is a desirable behaviour. Less oscillations in the speed makes for a less dynamic transition to the drifting equilibrium. An increase of inertia reduces the convergence speed of the drifting controller. This behaviour is to be expected, because the yaw moment created by the adaptive backstepping controller will create a smaller acceleration with increased inertia. Increased mass cannot be done without changing the inertia, however the controller is less sensitive to inertia variations than mass changes. Such that if the percentage inertia increase is kept less than equal to the mass increase, the controller will converge faster. By placing new equipment and sensors close to the vehicle center of gravity, this can be achieved.

The adaptive backstepping controller used for drifting in this assignment has proven to be effective at increasing vehicle manoeuvrability and this is shown in the last test case. When the adaptive backstepping controller is compared to a PID controller while following a figure eight path, drifting makes the vehicle stay on the road while the PID controller does not. This increase in manoeuvrability decreases lap times through the figure eight, because the path taken is shorter.

There is always room for improvement, even though the adaptive backstepping controller completes the turn in the final test case, a skilled driver could position the vehicle optimally before entering the turn and establishing the sideslip angle at the optimal position. A technique such as open loop commands in [24], could be used to mimic these manoeuvres, which are not taken into account in this thesis.

11 Conclusion

An adaptive backstepping controller has been designed which causes the LocalBug to stabilize at a drifting equilibrium with a desired sideslip angle in the range of -30 to 30 deg. The convergence from straight line to drifting is a nonlinear transition with changes in the dynamic response of the steering angle and the throttle actuators. For large sideslip angles the ground-tire contact forces are very nonlinear.

The adaptive backstepping controller has been proven capable of mimicking the behaviour of a recognized drifting technique called Power Over. Where the throttle is set to the maximum value to make the rear wheels slip and the steering increases the sideslip angle. This technique causes the speed to oscillate with a small amplitude about the desired value during drift initialization.

Adaptive backstepping has been shown to be robust against variation in vehicle mass and inertia, which is useful in further research using the LocalBug, because sensor arrays could be added or removed without needing to reconfigure the controller.

The LOS guidance system used in this thesis worked well together with the adaptive backstepping controller, providing sideslip angle references during path following. And during testing with the guidance system, the backstepping controller outperformed a PID controller both in cornering and lap time during a figure eight course.

Because the controller made in this thesis has a very aggressive behaviour, caution must be used to ensure unnecessary wear and tear on actuators does not occur.

11.1 Further Work

The controller derived in section 8.2 and 8.3 should be implemented and tested on the LocalBug. However, because control is performed on the sideslip angle, the controller should be tested with velocity errors and measurement noise before testing on the LocalBug. The system has been proven robust to mass and inertia errors, however the velocity errors may cause problems.

Wheel speed encoders should be considered for the LocalBug to enable wheel slip calculations, which can be used to find wheel forces and estimating road friction. This would enable the use of hybrid control based on friction estimates.

L1 adaptive control should be considered as an alternative controller to the adaptive backstepping. This is due to L1 having robustness to modelling errors, which makes it viable for drifting on surfaces with changing friction.

To improve controller performance, methods such as open loop commands to take advantage of techniques used by skilled drivers should be considered.

Bibliography

[1] H. F. Grip, L. Imsland, T. A. Johansen, J. C. Kalkkuhl, and A. Suissa, "Vehicle sideslip estimation - design, implementation and experimental validation," *IEEE control systems magazine*, vol. 29, no. 5, p. 36–52, 2009.

[2] E. Velenis, P. Tsiotras, and J. Lu, "Modeling aggressive maneuvers on loose surfaces: The cases of trail-braking and pendulum-turn," in *Proceedings of the 2007 European Control Conference, Kos, Greece*, July 2007.

[3] E. Velenis, E. Frazzoli, and P. Tsiotras, "Steady-state cornering equilibria and stabilization for a vehicle during extreme operating conditions," *International Journal of Vehicle Autonomous Systems*, vol. 8, no. 2/3, pp. 217–241, 2010.

[4] R. Y. Hindiyeh and J. C. Gerdes, "Design of a dynamic surface controller for vehicle sideslip angle during autonomous drifting," in *6th IFAC Symposium Advances in Automotive Control*, Munich, Germany, July 2010, pp. 560–565.

[5] J. L. Jakobsen, "Autonomous drifting of a 1:5 scale model car," Master's thesis, Norwegian University of Science and Technology, 2011.

[6] E. Velenis, "Fwd vehicle drifting control: The handbrake-cornering technique," in *2011 50th IEEE Conference on Decision and Control and European Control Conference (CDC-ECC)*, 2011.

[7] R. Y. Hindiyeh and J. C. Gerdes, "Equilibrium analysis of drifting vehicles for control design," in *Proceedings of the ASME 2009 Dynamic Systems and Control Conference*, 2009.

[8] J. Edelmann and M. Plöchl, "Handling characteristics and stability of the steady-state powerslide motion of an automobile," *Regular and Chaotic Dynamics*, vol. 14, no. 6, pp. 682–692, 2009.

[9] E. Velenis, E. Frazzoli, and P. Tsiotras, "On steady-state cornering equilibria for wheeled vehicles with drift," in *Decision and Control, 2009 held jointly with the 2009 28th Chinese Control Conference. CDC/CCC 2009*, December 2009.

[10] E. Velenis, D. Katzourakis, E. Frazzoli, P. Tsiotras, and R. Happee, "Stabilization of steady-state drifting for a rwd vehicle," in *10th International Symposium on Advanced Vehicle Control, Loughborough, UK*, August 2010.

[11] C. Voser, R. Y. Hindiyeh, and J. C. Gerdes, “Analysis and control of high sideslip manoeuvres,” *Vehicle System Dynamics: International Journal of Vehicle Mechanics and Mobility*, vol. 48, pp. 317–336, 2010.

[12] E. Velenis and P. Tsiotras, “Minimum time vs maximum exit velocity path optimization during cornering,” in *IEEE International Symposium on Industrial Electronics, Dubrovnic, Croatia*, June 2005, pp. 355–360.

[13] E. Velenis, P. Tsiotras, and J. Lu, “Optimality properties and driver input parameterization for trail-braking cornering,” *European Journal of Control*, vol. 14, no. 4, pp. 308–320, 2008.

[14] T. I. Fossen, *Handbook of Marine Craft Hydrodynamics and Motion Control*, 1st ed. John Wiley & Sons, 2011.

[15] K. Rottmann, *Matematiske Formelsamling*. Spektrum forlag, 2006.

[16] T. D. Gillespie, *Fundamental of Vehicle Dynamics*. Society of Automotive Engineers, Inc., 1992.

[17] U. Kiencke and L. Nielsen, *Automotive Control Systems for Engine, Driveline and Vehicle*, 1st ed. Springer-Verlag Berlin Heidelberg, 2000.

[18] O. Egeland and J. T. Gravdahl, *Modeling and Simulation for Automatic Control*. Marine Cybernetics, 2002.

[19] P. Mortion, *How to Drift: The Art of Oversteer*, 1st ed. Brookland Books, September 2006.

[20] H. K. Khalil, *Nonlinear Systems*, 3rd ed. Prentice Hall, 2002.

[21] T. I. Fossen, A. Loría, and A. Teel, “A theorem for ugas and ules of (passive) nonautonomous systems: robust control of mechanical systems and ships,” *International Journal of Robust and Nonlinear control*, vol. 11, no. 2, January 2001.

[22] P. A. Ioannou and J. Sun, *Robust Adaptive Control*, 1st ed. Prentice Hall, 1995.

[23] A. J. Sørensen, *Marine Control Systems: Propulsion and Motion Control of Ships and Ocean Structures*. a, a.

[24] S. Henry and A. Perrault, “Autonomous rc car drifting,” Cornell University, Tech. Rep., 2010.

A Discarded Sliding Mode controller

This controller was derived with cascade coupling of the sideslip angle β and the yaw rate $\dot{\psi}$ to make a steering angle controller.

A radially unbounded LFC, V, is used for deriving the controllers for sideslip and heading rate

$$V = \frac{1}{2}s^2 + \frac{1}{2}I_{zz}\dot{\tilde{\psi}}^2 \ > 0 \ \forall(s, \dot{\tilde{\psi}}) \neq (0, 0) \tag{A.1}$$

where $\dot{\tilde{\psi}}$ is the deviation from the desired yaw rate, s is a sliding surface for the sideslip angle. They can be written as

$$\begin{aligned} s &= \tilde{\beta} + k_\beta \int_0^t \tilde{\beta}(\tau)d\tau && \text{(A.2)} \\ \tilde{\beta} &= \beta - \beta_d && \text{(A.3)} \\ \dot{\tilde{\psi}} &= \dot{\psi} - \dot{\psi}_d && \text{(A.4)} \end{aligned}$$

where k_β is a positive gain.

By taking the time derivative of the LFC along the trajectory of the system, the controllers can be designed. The derivative yields

$$\begin{aligned} \dot{V} &= s\dot{s} + \dot{\tilde{\psi}}I_{zz}\ddot{\tilde{\psi}} \\ &= s(\dot{\beta} - \dot{\beta}_d + k_\beta\tilde{\beta}) + \dot{\tilde{\psi}}(I_{zz}\ddot{\psi} - I_{zz}\ddot{\psi}_d) \end{aligned}$$

By inserting $\dot{\beta}$ = $\dot{\chi}$ - $\dot{\psi}$ from equation (8.5) and $I_{zz}\ddot{\psi}$ = $N_w + (I_{xx} - I_{yy})pq$ from equation (4.18), such that

$$\dot{V} = s(\dot{\chi} - \dot{\psi} - \dot{\beta}_d + k_\beta\tilde{\beta}) + \dot{\tilde{\psi}}(N_w + (I_{xx} - I_{yy})pq - I_{zz}\ddot{\psi}_d) \tag{A.5}$$

Substitution of $\dot{\psi}$ = $\dot{\tilde{\psi}}$ + $\dot{\psi}_d$ from equation (A.4), yields

$$\dot{V} = \tilde{\beta}(\dot{\chi} - \dot{\tilde{\psi}} - \dot{\psi}_d - \dot{\beta}_d + k_\beta\tilde{\beta}) + \dot{\tilde{\psi}}(N_w + (I_{xx} - I_{yy})pq - I_{zz}\ddot{\psi}_d) \tag{A.6}$$

The yaw rate reference, $\dot{\psi}_d$, and the yaw moment, N_w, are chosen as

$$\dot{\psi}_d = \dot{\chi}_d - \dot{\beta}_d + k_\beta \tilde{\beta} + k_s \text{sgn}(s) + k_d s + \dot{\psi}_{d,ff} \tag{A.7}$$

$$N_w = I_{zz}\ddot{\psi}_d - k_r \dot{\tilde{\psi}} - (I_{xx} - I_{yy})pq \tag{A.8}$$

where k_s, k_d and k_r are positive gains, and $\dot{\psi}_{d,ff}$ is a desired yaw rate feed forward term, which is extracted from the equilibrium points found in section 6.2.

With equation (A.7) and (A.8), $\dot{V}$ becomes

$$\begin{aligned}
\dot{V} &= s(\dot{\chi} - \dot{\tilde{\psi}} - \dot{\chi}_d + \dot{\beta}_d - k_\beta \tilde{\beta} - k_s \text{sgn}(s) - k_d s - \dot{\psi}_{d,ff} - \dot{\beta}_d + k_\beta \tilde{\beta}) \\
&\quad + \dot{\tilde{\psi}}(I_{zz}\ddot{\psi}_d - k_r \dot{\tilde{\psi}} - I_{zz}\ddot{\psi}_d) \\
&= s(\dot{\chi} - \dot{\tilde{\psi}} - \dot{\chi}_d - k_s \text{sgn}(s) - k_d s - \dot{\psi}_{d,ff}) - k_r \dot{\tilde{\psi}}^2 \\
&= s(\dot{\chi} - \dot{\chi}_d - \dot{\psi}_{d,ff}) - k_s|s| - k_d s^2 - s\dot{\tilde{\psi}} - k_r \dot{\tilde{\psi}}^2 \\
&= s(\dot{\chi} - \dot{\chi}_d - \dot{\psi}_{d,ff}) - k_s|s| - \begin{bmatrix} s & \dot{\tilde{\psi}} \end{bmatrix} \begin{bmatrix} k_d & \frac{1}{2} \\ \frac{1}{2} & k_r \end{bmatrix} \begin{bmatrix} s \\ \dot{\tilde{\psi}} \end{bmatrix} \\
&= s(\dot{\chi} - \dot{\chi}_d - \dot{\psi}_{d,ff}) - k_s|s| - \begin{bmatrix} s & \dot{\tilde{\psi}} \end{bmatrix} Q \begin{bmatrix} s \\ \dot{\tilde{\psi}} \end{bmatrix}
\end{aligned} \tag{A.9}$$

The matrix Q needs to be positive definite to achieve a strictly negative derivative of the LFC, V. The determinant of the matrix Q must be positive if the matrix is positive definite, that is

$$\begin{aligned}
k_d k_r - \frac{1}{4} &> 0 \\
k_r &> \frac{1}{4k_d}
\end{aligned} \tag{A.10}$$

Assuming the gains follow the inequality in equation (A.10), the upper limit for the LFC is

$$\begin{aligned}
\dot{V} &\leq |s||\dot{\chi} - \dot{\chi}_d - \dot{\psi}_{d,ff}| - k_s|s| - \begin{bmatrix} s & \dot{\tilde{\psi}} \end{bmatrix} Q \begin{bmatrix} s \\ \dot{\tilde{\psi}} \end{bmatrix} \\
&\leq |s||\dot{\chi} - \dot{\chi}_d - \dot{\psi}_{d,ff}|_{max} - k_s|s| - \begin{bmatrix} s & \dot{\tilde{\psi}} \end{bmatrix} Q \begin{bmatrix} s \\ \dot{\tilde{\psi}} \end{bmatrix}
\end{aligned} \tag{A.11}$$

where the subscript max means the maximum of the absolute value. Now the sliding mode gain k_s is needed to dominate the unwanted terms. Consequently,

$$k_s \geq |\dot{\chi} - \dot{\chi}_d - \dot{\psi}_{d,ff}|_{max} \tag{A.12}$$

With k_s upholding the inequality in equation (A.12), such that

$$\dot{V} \leq -\begin{bmatrix} s & \dot{\tilde{\psi}} \end{bmatrix} Q \begin{bmatrix} s \\ \dot{\tilde{\psi}} \end{bmatrix} < 0 \tag{A.13}$$

By choosing the gains according to the inequality in equations (A.10) and (A.12), $\dot{V}$ becomes strictly negative. With a strictly negative $\dot{V}$ and a strictly positive radially unbounded V, the system is globally asymptotically stable, according to [20].

Even though this controller made the sideslip angle error $\tilde{\beta}$ converge to zero, it did not do it according to theory. The sliding surface s never approached zero, such that the controller did not achieve the control objective stated above. If the controller had behaved correctly, the sliding surface would approach zero and then the sideslip angle error would converge to zero. Because this controller did not work as intended, it was discarded and an adaptive backstepping controller was used instead.

B Contents of Attached ZIP-file

PDF File

- *Master's thesis*: Digital copy of master's thesis.

Matlab and Simulink files

- *carsim.mdl*: The guidance, controller and simulator model.
- *plot_figures.m*: Plots figures after simulation is done.
- *init_and_run.m*: Initialises variables for simulation and runs *carsim.mdl* and *plot_figures.m*.
- *show_movie*: Shows a movie of the simulation.
- *run_steadystate*: Finds equilibriums for sideslip angles of -30 deg to 30 with speeds of 1 m/s to 10. This script takes up to several days to find good values for the equilibriums.
- *run_linearisation*: Performs a linearisation of the equilibria.
- *plot_steady_state*: Plots maps between inputs and states. In addition, the pole placements for the linearised systems are plotted.